Design and Optimization of Novel Single-Ion Conducting Polymer Electrolytes for Sodium-Metal Batteries

Zur Erlangung des akademischen Grades eines

Doktors der Naturwissenschaften

(Dr. rer. nat.)

von der KIT-Fakultät für Chemie und Biowissenschaften des

Karlsruher Instituts für Technologie (KIT)

genehmigte

Dissertation

von

Clemens Wunder

1. Referent: Prof. Dr. Stefano Passerini

2. Referent: Prof. Dr. Patrick Theato

Tag der mündlichen Prüfung: Mai 2025

Abstract

Batteries are a cornerstone of our modern society, since they act as the energy source that powers various modern-day technologies such as mobile phones, laptops, and electric vehicles. The energy that sustains such devices is primarily derived from fossil fuels. However, growing concerns over the environmental damage caused as a result of procuring these fuels have intensified the search for greener and more sustainable alternatives. Renewable energy sources, such as wind and solar power, have advanced significantly in recent years. Nevertheless, their fluctuating nature necessitates the development of efficient methods to store the energy they generate on a large scale, ensuring their availability when demand exceeds production. Large-scale energy storage solutions pose a challenge for the currently dominant lithium-ion battery technology, due to the limited availability of lithium and related materials such as cobalt and nickel. Consequently, alternative and complementary technologies must be developed to overcome these limitations.

Sodium batteries present a promising alternative to lithium-ion batteries, because sodium is both abundantly available and inexpensive. This makes sodium batteries suitable for mass production using environmentally friendly and readily available materials, which enhances their sustainability and cost-effectiveness. However, sodium batteries, like lithium batteries, when intended for large-scale grid applications, must meet stringent safety standards to prevent potential hazards. The greatest risk associated with such batteries originates from their liquid electrolyte, which can leak, ignite, or cause thermal runaways. This peril of liquid electrolytes can be circumvented by utilizing dry, solid-state electrolytes instead. Solid-state electrolytes offer high thermal and mechanical stability, while remaining electrochemically stable even when coupled with metallic sodium, thereby improving the possible energy density of the battery.

In the class of solid-state electrolytes, polymer electrolytes are especially attractive for such applications due to their high design flexibility. They can be tailored to meet various requirements, such as specific operating temperatures, potential windows, and mechanical characteristics. Furthermore, the risk of charge gradient buildup and dendrite growth during cycling can be reduced by developing polymer electrolytes with single-ion conducting properties. In these electrolytes, the counter anion is tightly bound to the polymer backbone, which enhances efficient cationic transport within the battery.

In this thesis, new single-ion polymer electrolytes for sodium-metal batteries have been developed, characterized, and optimized, focusing on the component-driven influences on electrochemical performance. First, the composition of the polymer backbone was optimized, resulting in increased homogeneity and integrity of the single-ion polymer electrolyte. Subsequently, the supporting polymer and ionic conductor concentrations were investigated to boost ionic conductivity and cycling performance. The effect of the ionic group on ionic movement was assessed, leading to the identification of a high-performance anionic group that promotes fast cationic movement and stable interface formation. The spacer arm connecting the anionic group to the polymer backbone was then adjusted, further enhancing ion transport by increasing anionic mobility. This work was concluded by investigating the influence of the polymer backbone on the chemical and mechanical properties. The findings confirmed that structures with larger pores facilitate improved ionic movement but reduce mechanical stability, thus confirming the modularity of the polymer electrolyte. The influences of various components on the polymer electrolyte were successfully evaluated, and an optimized electrolyte with high ionic conductivity, wide electrochemical and thermal stability window, promising cyclability, and high capacity retention in Na||Prussian White cells was demonstrated.

These findings highlight the remarkable design flexibility of single-ion polymer electrolytes and their potential use in sodium-metal batteries. The studies revealed the impact of the composition, anionic center, spacer arm, and backbone morphology on the single-ion polymer electrolyte. Thus, these results serve as a valuable foundation for further optimization, showcasing the potential of single-ion polymer electrolyte-based sodium-metal cells as next-generation energy storage devices.

Kurzfassung

Batterien sind eine Schlüsseltechnologie in unserer modernen Gesellschaft, da sie eine Vielzahl von Alltagsgegenständen wie Smartphones, Laptops und Elektrofahrzeuge antreiben. Der Strom, mit dem diese Geräte betrieben werden, stammt jedoch hauptsächlich aus fossilen Brennstoffen. Angesichts der wachsenden Besorgnis über die Umweltschäden, die durch das Fördern und die Verbrennung fossiler Brennstoffe verursacht werden, hat die Suche nach umweltfreundlicheren und nachhaltigeren Alternativen an Bedeutung gewonnen. Die Technologien erneuerbarer Energiequellen wie Wind- und Sonnenenergie wurden in den letzten Jahren erheblich verbessert. Allerdings erfordert ihre unbeständige Natur zwingend die Entwicklung von großen Speichersystemen, damit die gewonnene Energie auch genutzt werden kann, wenn die Nachfrage die Produktion übersteigt. Energiespeicher in solch großen Maßstäben stellen jedoch eine immense Herausforderung für die derzeit dominierende Lithium-Ionen Batterietechnologie dar, da Lithium und die damit verbundenen Batteriekomponenten, wie Kobalt, Nickel oder Mangan, teuer und nur begrenzt verfügbar sind. Es ist daher zwingend notwendig, alternative und massenproduzierbare Technologien zu entwickeln, welche die fluktuierende Produktion von erneuerbaren Energien ausgleichen und somit dauerhaft verfügbar machen können.

Natrium-Ionen Batterien gelten als vielversprechende Alternative zu Lithium-Ionen Batterien. Sowohl Natrium als auch die Komponenten von Natrium-Ionen-Batterien bestehen aus weit verbreiteten, umweltfreundlichen und kostengünstigen Materialien, was eine kosteneffiziente Massenproduktion ermöglicht. Allerdings müssen Natrium-Ionen Batterien, ebenso wie Lithium-Ionen Batterien, welche speziell für den Einsatz in Netzspeichern vorgesehen sind, ein sehr hohes Sicherheitsniveau gewährleisten, um potenzielle, weitreichende Risiken zu vermeiden. Die größte Gefahr bei solchen Batterien geht von ihrem flüssigen Elektrolyten aus, der auslaufen, brennen oder thermische Durchgänge verursachen kann. Trockene Festkörperelektrolyte umgehen dieses Risiko, bieten eine erhöhte thermische und mechanische Stabilität und ermöglichen die Verwendung von metallischem Natrium, was die Energiedichte der Batterie weiter verbessern kann.

Unter den Festkörperelektrolyten sind Polymerelektrolyte für diese Anwendungen besonders attraktiv, da sie sehr vielseitig gestaltet werden können. Sie können gezielt modifiziert werden, um verschiedensten Anforderungen gerecht zu werden, wie etwa einer spezifischen Betriebstemperatur, einem erweiterten Potenzialfenster oder einer erhöhten mechanischen Stabilität. Zusätzlich kann das Risiko von Ladungsungleichgewichten und Dendritenwachstum während des Betriebs durch Polymerelektrolyte mit ionenselektiver Leitfähigkeit (Single-Ion) verringert werden. In solchen Single-Ion Polymerelektrolyten ist das Anion an ein Polymer-Rückgrat gebunden, was den effizienten Kationentransport innerhalb der Batterie verbessert.

In dieser Arbeit wurde ein neuer Single-Ion Polymer-Elektrolyt für Natrium-Metall Batterien entwickelt, analysiert und der Einfluss verschiedener Komponenten auf die thermischen und elektrochemischen Eigenschaften untersucht. Zunächst wurde die Struktur des Polymergerüsts untersucht und optimiert, indem das Verhältnis der gerüstbildenden Komponenten variiert wurde. Daraufhin erfolgte eine detaillierte Analyse des Hilfspolymers und der anionischen Gruppen, um die Leitfähigkeit weiter zu verbessern, wodurch eine geeignete anionische Gruppe identifiziert werden konnte, die eine schnelle kationische Leitfähigkeit sowie eine stabile Grenzflächenbildung ermöglicht. Anschließend wurde der Effekt des „Verbindungs-Arms“, der die anionische Gruppe mit dem Polymer-Rückgrat verbindet, untersucht. Es wurde festgestellt, dass der Kationentransport durch eine erhöhte Mobilität des Anions verbessert wird. Abschließend wurde die Struktur des Polymergerüsts selbst weiter untersucht, wobei bestätigt wurde, dass weniger Verzweigungen größere Poren erzeugen, welche die Leitfähigkeit positiv beeinflussen. Jedoch führt dies zu einem Kompromiss, da die mechanische Stabilität dadurch verringert wird. Auf Basis dieser Ergebnisse wurde ein optimierter Elektrolyt entwickelt, der eine hohe ionische Leitfähigkeit, eine gute Stabilität in einem weiten Spannungsbereich, eine gute thermische Stabilität, exzellente Zyklisierbarkeit und eine hohe Kapazitätserhaltung in einer Natrium-Metall||Prussian White Zelle aufweist.

Die Möglichkeit, Natrium-Metall Batterien mithilfe von Single-Ion Polymer-Elektrolyten zu realisieren, wurde in dieser Arbeit eingehend untersucht, da sie ein großes Potenzial für zukünftige mobile und stationäre Energiespeichersysteme bietet. Es konnte gezeigt werden, dass Polymerelektrolyte eine außergewöhnliche Vielseitigkeit im Design aufweisen, was sie zu einer vielversprechenden Grundlage für Natrium-Metall Batterien macht. Die verschiedenen Analysen haben erfolgreich aufgezeigt, wie die prozentuale Polymerzusammensetzung, das anionische Zentrum, der Verbindungs-Arm sowie die Morphologie des Gerüstpolymers die Eigenschaften von Single-Ion Polymer-Elektrolyten beeinflussen. Diese Erkenntnisse liefern detaillierte Einblicke in die Funktionsweise von Single-Ion Polymer-Elektrolyten und bieten eine wertvolle Grundlage für zukünftige Forschungsansätze sowie für die Kommerzialisierung von Natrium-Metall Batterien.

Table of Contents

Abstract I

Kurzfassung III

Table of Contents VI

List of Abbreviations X

1 Preface 1

2 Introduction 3

2.1 Battery Technologies 3

2.1.1 Common Battery Terms 5

2.2 Lithium-Ion Batteries 6

2.2.1 Lithium-Metal Batteries 9

2.3 Sodium-Ion Batteries 11

2.3.1 Negative and Positive Materials for SIBs 12

2.3.2 Sodium-Metal Batteries 14

2.4 Solid-State Electrolytes 16

2.4.1 Solid-State Polymer Electrolytes 17

2.4.2 Quasi-Solid-State Polymer Electrolytes 18

2.5 Single-Ion Polymer Electrolytes 20

2.5.1 Influence of the Anionic Center 22

2.5.2 Influence of the Spacer Arm 23

2.5.3 Influence of the Backbone 23

2.5.4 Sodium-based SIPEs 24

3 Motivation and Aim 26

4 Materials and Techniques 28

4.1 Materials 28

4.1.1 Materials for Synthesis 28

4.1.2 NMR Solvents and Plasticizers 28
4.1.3 Purifications 29
4.2 Synthesis of the Sodium Salt Monomers 29
4.2.1 Synthesis of the NaSTFSI monomer 29
4.2.2 Synthesis of the NaSDCM monomer 32
4.2.3 Synthesis of the NaFTFSI monomer 34
4.2.4 Synthesis of the NaMDCM monomer 35
4.3 Membrane Fabrication 37
4.3.1 NaSTFSI-SIPEs 37
4.3.2 Membrane Fabrication using Alternative Components 38
4.3.3 Membrane List 38
4.4 Characterization Techniques 41
4.4.1 Nuclear Magnetic Resonance Spectroscopy 41
4.4.2 Fourier-Transform Infrared Spectroscopy 44
4.4.3 Thermogravimetric Analysis 45
4.4.4 Differential Scanning Calorimetry 46
4.4.5 Chronopotentiometry 47
4.4.6 Linear Sweep Voltammetry 48
4.4.7 Galvanostatic Cycling 49
4.4.8 Mechanical Properties 50
4.4.9 Electrochemical Impedance Spectroscopy 50
4.4.10 X-Ray Photoelectron Spectroscopy 51
4.4.11 Small- and Wide-Angle X-ray Scattering 53
4.5 Instrumental Procedures 54
4.5.1 Nuclear Magnetic Resonance Spectroscopy 54
4.5.2 Fourier-Transform Infrared Spectroscopy 55
4.5.3 Thermogravimetric Analysis 55
4.5.4 Differential Scanning Calorimetry 55
4.5.5 Chronopotentiometry 55
4.5.6 Linear Sweep Voltammetry 56
4.5.7 Galvanostatic Cycling 56
4.5.8 Mechanical Properties 56

4.5.9 Electrochemical Impedance Spectroscopy 56
4.5.10 X-Ray Photoelectron Spectroscopy 57
4.5.11 Small- and Wide-Angle X-ray Scattering 57

5 Results and Discussion 59

5.1 NaSTFSI-SIPE Development 60
5.1.1 NaSTFSI SSM and NaSTFSI-SIPE Characterization 60
5.1.2 Thermal Properties of NaSTFSI-SIPE 63
5.1.3 Electrochemical Characterization of the NaSTFSI-SIPE 64
5.1.4 Study of the Solid Electrolyte Interphase 67
5.1.5 Electrochemical Performance of NaSTFSI-SIPE SMBs 70
5.1.6 Conclusion on the Performance of NaSTFSI-SIPE 72
5.2 Component-Driven Influence in NaSTFSI-SIPEs 73
5.2.1 Optimizing the Ratio of the Backbone Monomers 74
5.2.2 Optimizing the PVDF-HFP Content 75
5.2.3 Optimizing the Sodium Salt Monomer Content 80
5.2.4 Conclusion on the Component-Driven Influence 85
5.3 SSM Design with Varying Anionic Centers 87
5.3.1 Structures of SSMs with Varying Anionic Centers 87
5.3.2 Ionic Conductivity Dependence on Anionic Center 89
5.3.3 Cycling Performance in Symmetric Sodium-Metal Cells 91
5.3.4 Study of the Solid Electrolyte Interphase 91
5.3.5 Galvanostatic Cycling Performance 93
5.3.6 Conclusion on the Influence of the Anionic Center 94
5.4 Spacer Arm Variation in TFSI-based SIPEs 95
5.4.1 Chemical Structures of SSMs with Varying Spacer Arms 95
5.4.2 Thermal and Electrochemical Properties 96
5.4.3 Spacer Arm Dependent Cycling Performance 101
5.4.4 Conclusion on the Spacer Arm Investigation 103
5.5 Investigation of Different Backbones with NaMTFSI as SSM 104
5.5.1 Chemical Structures of Different Polymer Backbone Monomers 104
5.5.2 Mechanical Properties of SIPEs with Different Backbone Monomers . . . 105
5.5.3 Thermal Stability of SIPEs with Different Backbones 107

5.5.4 Small and Wide Angle X-ray Scattering 107
5.5.5 Conductivity and Electrochemical Stability Window 111
5.5.6 Cycling Performance of the SIPEs with different Backbones 112
5.5.7 Conclusion on the use of different Backbones 114
5.6 Combing the Best Performing Anionic Center, Spacer Arm and Backbone Monomers 115
5.6.1 Overview of the Obtained Advantages 115
5.6.2 Thermal and Electrochemical Characterization of the NaMDCM-SIPE . 116
5.6.3 Cycling Performance of NaMDCM-Based SIPEs 118
5.6.4 Conclusion on the Optimized NaMDCM-SIPE 118

6 Conclusion and Outlook 119
6.1 Conclusion 119
6.2 Outlook 121

7 References 123

8 Appendix 134

List of Figures 136

List of Tables 143

9 Acknowledgements 144

10 Academic Contributions 146
10.1 Scientific Meetings and Conferences 146
10.2 Publications 147

List of Abbreviations

CPMAS-NMR	Cross-polarization magic angle spinning nuclear magnetic resonance
DEC	Diethylene carbonate
DCM	Dichloromethane
DMC	Dimethyl carbonate
DMSO	Dimethyl sulfoxide
DSC	Differential scanning calorimetry
EC	Ethylene carbonate
EIS	Electrochemical impedance spectroscopy
EOL	End of life
ESV	Electrochemical stability window
EU	European Union
EVs	Electric vehicles
FEC	Fluoroethylene carbonate
FT-IR	Fourier transformed infrared spectroscopy
HC	Hard carbon
LIB	Lithium-ion battery
LiFSI	Lithium bis(fluorosulfonyl)imide
LiTFSI	Lithium bis(trifluoromethanesulfonyl)imide
LMB	Lithium-metal battery
MS	Mass spectrometry
NaCMC	Sodium carboxymethyl cellulose
NaFTFSI	Sodium (((1,1,2,2-tetrafluoro-2-(1,1,2,2-tetrafluoro-2-iodo-ethoxy)ethyl) sulfonyl)-((trifluoro-methyl)sulfonyl)amide
NaMTFSI	Sodium ((3-acetoxypropyl)sulfonyl)-((trifluoromethyl) sulfonyl)amide
NASICON	Sodium superionic conductor
NaSTFSI	Sodium 4-styrenesulfonyl(trifluoromethylsulfonyl) imide

NMR	Nuclear magnetic resonance
PAN	Poly (acrylonitrile)
PC	Propylene carbonate
PEO	Poly (ethylene oxide)
PET4A	Pentaerythritol tetraacrylate
PETMP	Pentaerythritol tetrakis(3-mercaptopropionate)
PVA	Poly(vinyl alcohol)
PVC	Poly(vinyl chloride)
PVDF	Poly(vinylidene-fluoride)
PVDF-HFP	Poly(vinylidene-fluoride-hexafluoropropylene)
PVP	Poly(vinyl pyrrolidone)
PW	Prussian White
QSSPE	Quasi-solid-state polymer electrolyte
QSS-SIPE	Quasi-solid-state single-ion polymer electrolyte
QSSSMB	Quasi-solid-state sodium-metal battery
RT	Room temperature (20 °C)
SEI	Solid-electrolyte interphase
SIB	Sodium-ion battery
SIPE	Single-ion polymer electrolyte
SMB	Sodium-metal battery
SSB	Solid-state battery
SSE	Solid-state electrolyte
SSM	Sodium salt monomer
SSPE	Solid-state polymer electrolyte
SWAXS	Small- and wide-angle X-ray scattering
TEA	Triethyl amine
TGA	Thermo gravimetric analysis
TGA-MS	Thermogravimetric analysis coupled with mass spectroscopy
VTF	Vogel-Tamman-Fulcher
XPS	X-ray photoelectron spectroscopy

Preface

Humanity is evolving at a tremendous pace, with most of our major technologies having been discovered only in the past few decades. The boom of technological research began with the industrial revolution at the end of the 18th century, which marked the turning point for countless innovations following in rapid succession. Notable milestones include the first generator in 1831, followed by the invention of the light bulb in 1835, the telephone in 1861, the automobile in 1885, the first computer in 1941, and the introduction of the internet in 1991, among others.[1–3] Most of the technologies shaping our modern lives today share one common factor: they require energy, more specifically, electricity, to function. Electricity can be produced through various methods, such as burning coal or oil, to power a generator. However, fossil fuels are increasingly controversial due to their environmental impact, including both the mining process and the emissions released during burning.[4–6]

Alternative power sources, such as wind, water, and solar energy, have been researched extensively and are now widely available, enabling us to harness these renewable energy sources for our own use. However, a major challenge remains for the transition from fossil fuels to renewable energy: the intermittent nature of its production. Solar energy, for instance, is dependent on daylight, while wind and water energy fluctuate based on weather conditions. Solar panels reliably generate green energy to power various devices during the day. Nevertheless, they cannot generate energy at night, yet society continuously requires electricity. This inconsistency poses a significant challenge to their reliability, which must be addressed to pave the way for a carbon-neutral future.[7–9] These natural fluctuations could be overcome by storing excess energy generated in periods of high production for later use. Batteries are an ideal candidate for this strategy, since they can efficiently store and release energy in a reversible manner.

However, the growing demand of energy storage cannot be achieved using the currently predominant lithium-ion batteries (LIBs) alone, as lithium and key battery components such as cobalt and nickel are critical raw materials that are both expensive and limited in supply. Therefore, alternative energy storage technologies that provide a safe, sustainable, mass-producible and affordable method for energy storage must be researched to overcome these constraints.[10]

Sodium-based batteries present attractive candidates for sustainable energy storage due to their affordable and environmentally friendly design. While their lower specific energy density is often considered a disadvantage, does it not pose a significant obstacle for stationary applications where space constraints are less critical. Batteries, especially for large-scale energy storage, must be designed with safety as a top priority to prevent any potential harm to both their users and the environment. Typically, the greatest safety risk arises from the use of flammable, volatile, and/or toxic liquid electrolytes. Replacing the liquid electrolyte with a solid or quasi-solid-state electrolyte can mitigate these risks, which in turn, reduces the danger of leaking solvents. Additionally, the substitution could enable a higher energy density by utilizing sodium-metal as the negative electrode instead of an insertion electrode.

Among various solid-state electrolytes, polymer electrolytes stand out as the most promising candidates, since they offer high thermal stability, wide electrochemical stability window, versatility and modifiability. Polymer electrolytes can be specifically tailored to meet desired properties, such as designing single-ion polymer electrolytes (SIPEs), where the anion is chemically bonded to the polymer backbone. This restriction of the movement of the anion not only prevents the build-up of concentration gradients, but also suppresses dendrite growth, all while maintaining the key advantages of a solid polymer electrolyte.

The next key step towards a sustainable lifestyle is the transition from fossil fuels to renewable energy sources, which requires cost-effective, environmentally friendly, and mass-produced batteries. Among these, sodium-based batteries stand out as the most promising candidates, as they use abundant raw materials, which can be combined with a solid-state SIPE to leverage the potential of sodium-metal as the anode material. Research on single-ion solid-state polymer electrolytes for sodium-metal batteries (SMBs) significantly improves batteries safety. However, they represent a completely new field that is in active development. This work aims to provide a deeper understanding of SIPEs and their use in SMBs, which will aid in realizing safe, sustainable, and mass-producible batteries that are essential for fully enabling renewable energy sources. Such advancements represent a crucial step toward a truly sustainable future.

Introduction

Chapter 2.1
Battery Technologies

Batteries fulfill an essential role in our modern society, powering a wide range of devices and systems we rely on every day. The key components of a battery are the negative electrode (anode), the positive electrode (cathode) and the electrolyte, which allows the ions to move between the electrodes (Figure 2.1). Upon connecting both electrodes, a steady flow of electrical energy occurs, which can be used to fuel various electronic devices such as remote controls, mobile phones, laptops, electric vehicles (EVs) and so forth. Batteries that can only be discharged once are called primary (non-rechargeable) batteries. Nowadays, they are predominantly used in devices with low power consumption, like remote controllers or calculators. At the same time, batteries that can be charged and discharged continuously for hundreds or thousands of cycles are labeled as secondary (rechargeable) batteries and find their use in various modern applications.[11]

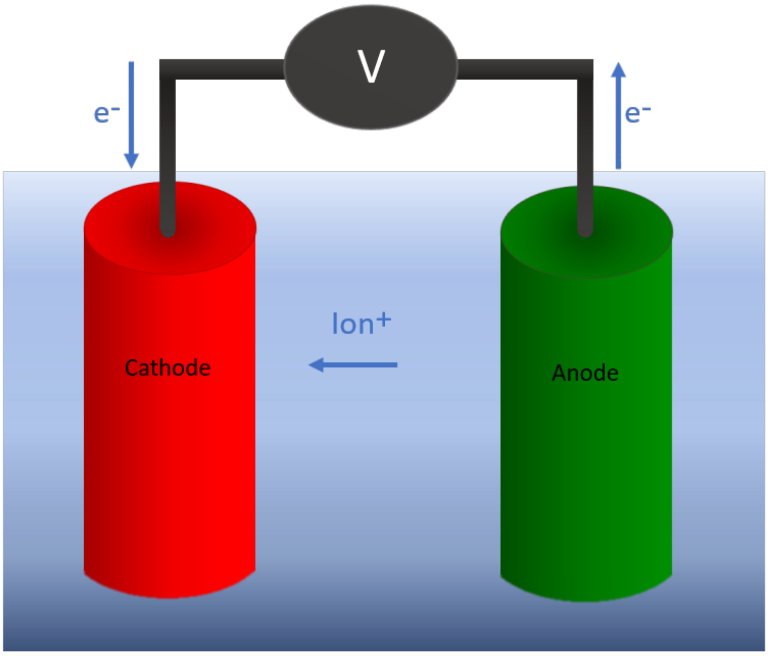

Figure 2.1: Scheme of a rechargeable battery. During discharge, the electrons travel from the negative electrode (anode, green) to the positive electrode (cathode, red), where the cations travel through the single ion-conducting electrolyte (blue), reducing the positive electrode and oxidizing the negative one.

The first battery was invented by Alessandro Volta in Italy in the 18th century, following the discovery of electricity by Luigi Galvani. He witnessed that a frog's leg would move when touched by a series of two different metals and concluded that electric energy flows between the used zinc and silver disks, which they had connected with a piece of cloth soaked in sodium chloride.[12] The critical role of the electrolyte that allows ion transport but hinders the electronic conductivity was already discovered in those days, as Volta wrote that "the electric current is hindered for this experiment due to the interposed wet layers which are not good conductors".[13] After their first development, batteries were further investigated by Lechlanché, Junger and Planté and many other researchers using, e.g., silver and zinc, lead-acid, and nickel-cadmium or nickel metal hydride battery systems.[14] However, the energy density of these batteries was still rather low, leading to heavy and big batteries which were not practical for most desired applications.[15]

2.1.1 Common Battery Terms

In order to discuss the numerous properties a battery possesses, the most essential terms in battery research that are needed for battery performance will be defined. First, cells are noted as anode||cathode or as anode||electrolyte||cathode. The amount of energy that can be stored inside the cell will be referred to as the capacity (mAh), while specific capacity (mAh g^{-1}) expresses the capacity per mass of the active material in the cell. The third capacity term is the theoretical capacity and theoretical specific capacity, respectively, which represent the capacity in an ideal setup. The theoretical capacity (Q) can be calculated using the formula $Q = zF/M$, wherein z is the number of transferred electrons, F is the Faraday constant, and M is the molecular mass of the electroactive material. The theoretic capacity can further be multiplied with the theoretical voltage to obtain the theoretical specific gravimetric (Wh kg^{-1}) or volumetric (Wh L^{-1}) energy density. Considering the ideal case, the obtained capacity would still be far lower than the theoretical capacity due to the inefficiency of the charge and discharge processes. In reality, the practical capacity might be even lower because of various factors, such as the operation temperature, the degree of wear and tear of the cell, and the charge and discharge current. The current in relation to the capacity is referred to as "C-rate" (Charge/discharge rate), whereof a C-rate of 1 (labeled 1C) is defined as charging or discharging the whole capacity within one hour. A faster C-rate, e.g., 2C, refers to a higher current that charges and discharges the cell in 30 min each, while a slower C-rate, e.g., 0.1C indicates a 10 times lower current and a charge/discharge time of 10 hours, respectively. The capacity of charge and discharge can be set into relation to determine the Coulombic efficiency (CE), allowing to access the efficiency of the cell's cycling performance.[16]

Chapter 2.2
Lithium-Ion Batteries

A major breakthrough in battery research came through the development of new batteries with lithium-based electrode materials. Lithium has a high reduction potential of -3.01 V compared to the standard hydrogen electrode (SHE), and it is the lightest metal known. These properties led to the development of LIBs in the 1980s by Scrosati, Whittingham, Goodenough and Yoshino, and their first commercialized use in 1991 by the Sony corporation.[17] The rechargeable LIBs could be produced with a more compact and lighter design compared to previous batteries, reaching a much higher energy density (Figure 2.2) compared to, e.g., lead-acid or nickel metal hydride batteries.[13,18]

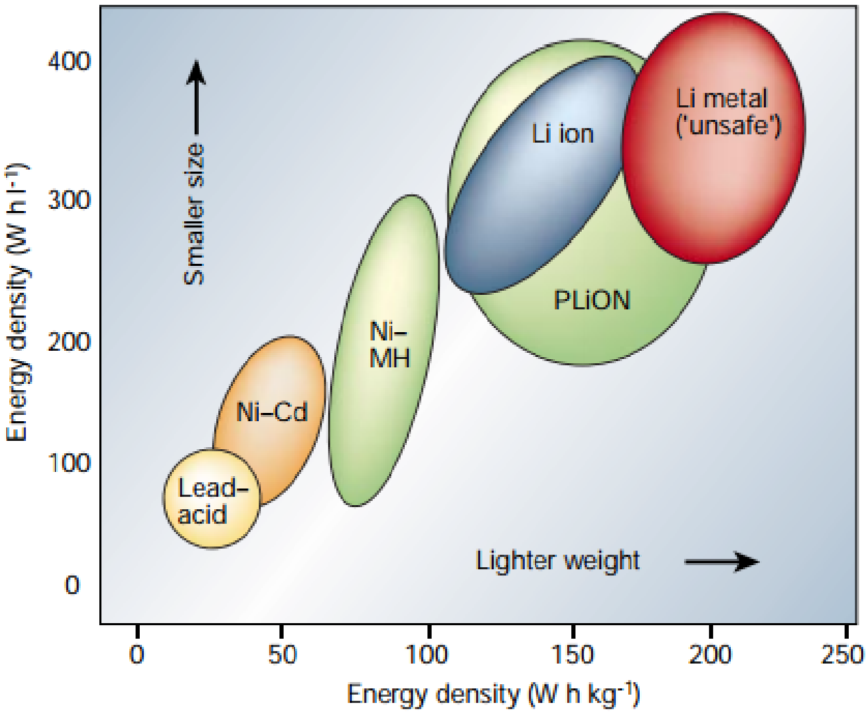

Figure 2.2: Volumetric vs gravimetric energy density plot, where different battery chemistries are compared. Reprinted from ref.[19] ©2016 IEEE

LIBs use the rocking-chair mechanism allowing the ionic charge carriers to reversibly intercalate and de-intercalate into the positive and negative electrodes (Figure 2.3), allowing for fast and efficient energy storage. The rocking-chair mechanism comes with many advantages, such as low self-discharge, long cycle life, high energy density and high supported operation voltage, which let LIBs secure a dominant position in the battery market ever since their first discovery.[20]

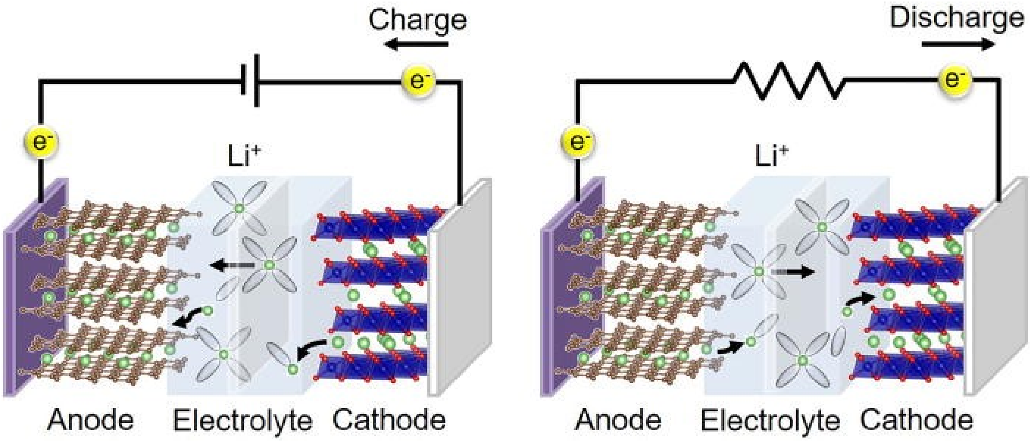

Figure 2.3: Scheme of LIBs, a) upon charge and b) discharge, Li ions intercalate into the anode (during charge) and the cathode (during discharge) structure. Reprinted from Energy Storage Materials, Vol. 60, Deng et al.[20], Recent advances in rocking chair batteries and beyond, 102820, 2023, with permission from Elsevier.

During the charging process, Li ions leave the positive electrode, resulting in its oxidation (Equation 2.1), and migrate to the negative electrode through the electrolyte. The Li ions intercalate into the graphite layers of the negative electrode, which takes up the Li ions and becomes reduced, leading to a charged battery state (Equation 2.2). The stored energy can be released by reverting the reaction when an electric device is connected to both electrodes, allowing Li ions to flow through the electrolyte back to the positive electrode, where they intercalate into the electrode material while electrons arriving via the external circuit complete the reduction/oxidation reaction. This reaction restores the oxidized state of the positive electrode, while the generated electron flow (Equation 2.3) powers electronic devices.

$$Negative\,electrode: \quad C_6 + x\,Li^+ + x\,e^- \rightleftharpoons C_6Li_x \tag{2.1}$$

$$Positive\,electrode: \quad LiMO_2 \rightleftharpoons Li_{1-x}MO_2 + x\,Li^+ + x\,e^- \tag{2.2}$$

$$Total: \quad C_6 + LiMO_2 \rightleftharpoons C_6Li_x + Li_{1-x}MO_2 \tag{2.3}$$

The electrodes in LIBS exhibit crystalline structures to allow for efficient Li ion insertion. Commercial negative electrodes are mainly based on carbon, i.e., graphite coated on copper foil, showing a low reduction/oxidation potential of about 0.1 V vs Li^+/Li, while most commercial cathodes are metal oxides coated on aluminum foil that utilize nickel, manganese, and cobalt oxide (including their mixtures), or iron phosphate. Additives like conductive carbon and a binder are mixed into the electrodes to improve, respectively, the electron transport within the active material and the electrode´s self-consistence and adhesion towards the current collector. The electrodes are separated by an electrolyte to avoid a direct electronic contact, which would lead to a short circuit and, thus, a loss of the cell's capacity. This electrolyte is often a mixtures of cyclic and/or linear organic carbonates (Figure 2.4) like ethylene carbonate (EC), propylene carbonate (PC), fluoroethylene carbonate (FEC), dimethyl carbonate (DMC) or diethyl carbonate (DEC), dissolving a lithium salt like, e.g., lithium hexafluorophosphate ($LiPF_6$), lithium bis(fluorosulfonyl)imide (LiFSI) or lithium bis(trifluoromethanesulfonyl)imide (LiTFSI), while the mechanical integrity is provided through a rather inert porous separator (like poly(olefins)).

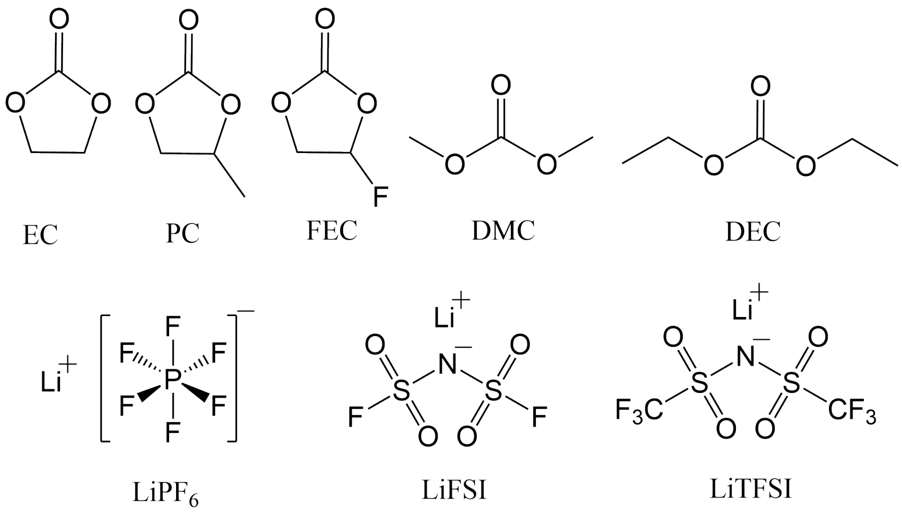

Figure 2.4: The chemical structures of common carbonate solvents (upper row) and conducting salts (lower row).

LIBs were further improved since their first development and now provide specific energy densities up to 300 Wh kg^{-1} due to various optimizations, such as e.g., a better cell geometry, a reduced weight of the inactive components, and better contact interfaces. This specific energy density is predicted to grow even more to a maximum energy density of up to 350 Wh kg^{-1} in the near future.[20,21] LIBs are nowadays used to empower EVs, which will drastically increase battery demand in the next years. More specifically, the required energy for EVs is predicted to reach 5000 GWh in 2035 (Figure 2.5).

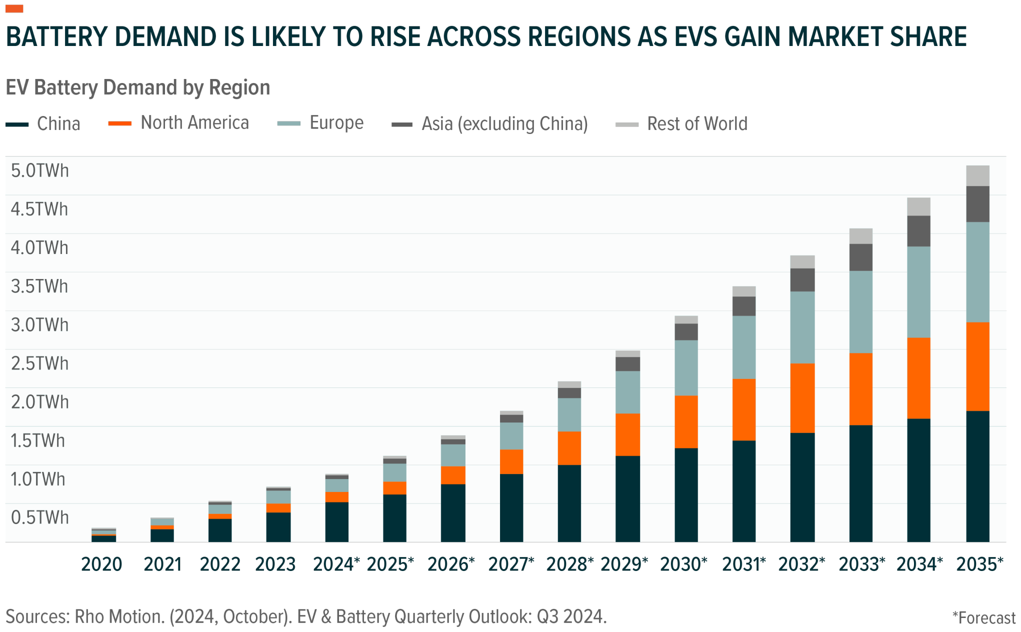

Figure 2.5: Predicted growth of LIBs in EVs. The demand is expected to steadily increase and reach up to 5000 GWh in the next 10 years. Reprinted with permission from Rho Motion, 2024

2.2.1 Lithium-Metal Batteries

While LIBs are promising candidates for energy storage, the world demands more and more battery capacity every year. Thus, the energy density, the price, the availability of LIBs' components and the maximum energy density of 350 Wh kg^{-1} might not be sufficient in the future. The limitations of the energy density originate from the insertion mechanism of the negative electrode material. LMBs can circumvent this problem removing the weight of the negative host material, but still share the similar working mechanism of LIBs at the cathode, using reactive lithium-metal as anodic electrode. This results in highly increased anode specific capacity (3860 mAh g^{-1}), enabling, e.g., Li||NCM88 (nickel cobalt manganese oxide) cell with 560 Wh kg^{-1}, far exceeding LIBs.[22] However, the total worldwide available amount of lithium reserves is predicted to be between 25 million metric tons (https://www.statista.com, July 2024) and 80 million tons (https://www.nsenergybusiness.com, July 2024). Assuming a demand between 113 g and 246 g (170 g on average) of lithium per kWh (Tahil, W. (2010), Meridian) suggests that using all reported lithium reserves for LMBs would lead to a maximum lithium battery capacity between 147 and 470 thousand GWh (Equation 2.4). Comparing this maximum capacity with the expected demand of batteries only for EVs, suggests that between 1% and 4% of the world reserves of lithium will be used up for new lithium powered electronic vehicles alone in the year 2035 (5000 GWh). The demand for new EVs is predicted to increase even more in the following years, suggesting that lithium-based batteries will face a serious material shortage within the next 100 years.

$$\frac{25-80\cdot 10^{12} g\,(predicted\,lithium\,reserves)}{170\frac{g}{KWh}\,(lithium\,per\,KWh)\cdot 10^{6}\frac{KWh}{GWh}\,(conversion\,factor)} = 117-470\cdot 10^{3}\,GWh \qquad (2.4)$$

In addition to the resource limitations of lithium, the positive metal oxides incorporated in LIBs also have finite availability. Most of the elements used in the metal oxide positive electrodes, such as e.g., cobalt or nickel, are mined in South America, South Africa and Australia, and purified in China, being considered critical raw materials by the EU.[10,23] Alternative energy storage solutions with local production chains, widely available resources, environmentally friendly components, low costs and high energy densities that can complementarily fulfill the energy storage requirements have to be investigated to satisfy the energy market and realize a carbon-neutral future.

Chapter 2.3
Sodium-Ion Batteries

An attractive alternative or complementary technology to LIBs and LMBs are Na ion batteries (SIBs), which have a similar working mechanism, offer comparable performance to $LiFePO_4$-based LIBs, already available on the market for light EVs and grid applications.[24,25] Common sodium salts such as Na_2CO_3, Na_2SO_4 and NaCl are of low-cost and highly abundant, as they can be obtained from minerals and brine world-wide ($2.4\cdot10^4$ ppm in the Earth's crust and $1.1\cdot10^4$ ppm in the ocean compared to 20 ppm and 180 ppm for lithium, respectively. Figure 2.6), adding up to over 1 trillion tons of sodium reserves.[26,27]

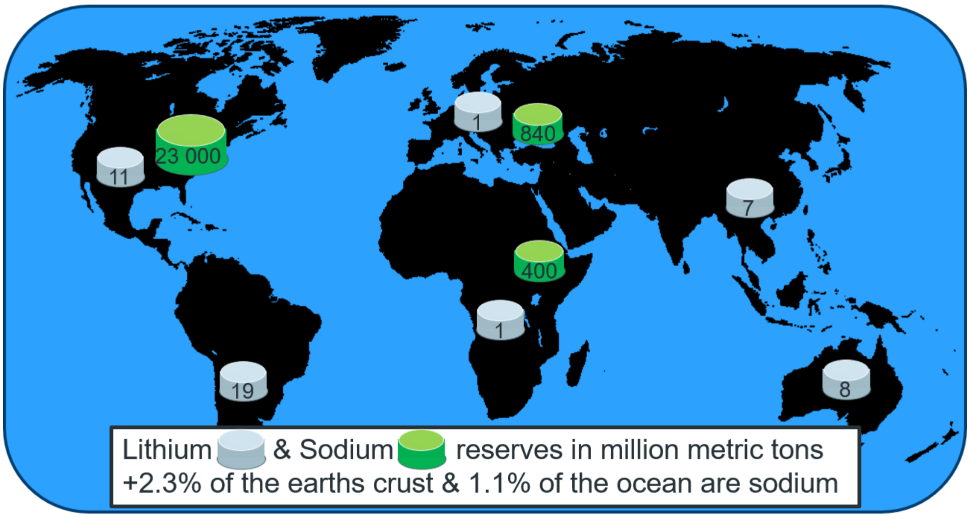

Figure 2.6: Li and Na reserve distribution on the world.

Additionally, SIBs can also use aluminum as a cheaper alternative instead of the most expensive copper as a negative current collector because sodium does not have the drawback of forming an alloy with aluminum at low voltages.[20,28–30] Nonetheless, sodium has several disadvantages in comparison with lithium, such as lower reduction potential of -2.71 V vs -3.04 V (both versus SHE), higher atomic mass (23 g mol^{-1} for sodium and 7 g mol^{-1} for lithium) and larger size (Shannon ionic radius of 1.02 Å and 0.76 Å, respectively), resulting in a decrease of the theoretical energy density.[30,31] These drawbacks reflect in the small current market share (less than 4%) of sodium-based batteries (Figure 2.7). However, SIBs are a promising candidate for various energy storage devices where their wide availability outweighs their reduced energy density.[32] Thus, their production is expected to grow up to 186 GWh year^{-1} by 2030, which equals 4.6 million new EVs per year.[24,33,34]

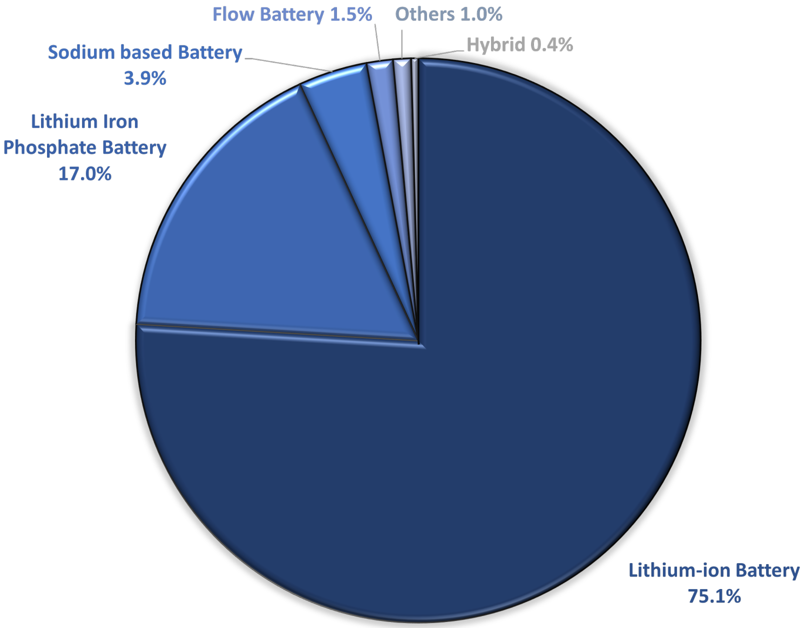

Figure 2.7: Market share of different battery chemistries in 2023. Lithium-ion battery refer to cells employing Co, Mn and Ni based cathodes.[35]

2.3.1 Negative and Positive Materials for SIBs

The negative material for SIBs can be divided into three main categories: metal oxides/sulfides, alloys, and carbon-based materials. Metal oxide and metal sulfide anode materials that use, e.g., Fe, Sb, Sn, Mo or Mn, store Na ions by conversion, insertion and alloying reactions, forming sodium oxides and sulfides in the process. However, these materials often show slow kinetics, large volume expansion, and reach only rather high potentials vs Na^+/Na, which hinder their practical application.[33] Alloying anode materials such as SnSb/C composites use carbon for electronic conductivity and mechanical stability, while a thin alloy allows for potentially high capacities.[33,36,37] However, alloys often suffer from significant volume expansions compared to their Li equivalents. Additionally, the reaction of the sodiated host material with the electrolyte builds an unstable solid-electrolyte interphase (SEI) due to the solubility of SEI components in commonly used organic electrolytes, leading to the continuous growth of the SEI and consumption of Na.

Various carbon-based anode materials are used in SIBs, such as, e.g., graphite,[38,39] soft carbon,[40,41] hard carbon (HC),[42,43] doped carbon fibers,[39,44] doped carbon sheets,[45] or biomass-derived carbon materials (including HC).[46] Among these anode materials, HC is considered the most promising candidate due to its good cycling performance, high stability, wide availability and low production cost. However, SIBs with insertion-type anode materials inevitably have a limited energy density due to the charge-storage limitations of Na ions. This bottleneck originates from the size of Na ions, which either require a lot of space or produce large volume expansions in combination with insertion-type electroactive materials.[47]

The positive electroactive material for SIBs primarily consists of metal-layered oxides due to their high specific capacity, rate capability and cycling stability. These metal layered oxides have the general formula $Na_xT_MO_2$ and are composed of repeating sheets of T_MO_6 layers alternating with Na ions in between the interlayers. Layered oxides can be present in various phases depending on the coordination of Na, such as, e.g., prismatic (P2 or P3) or octahedral (O3) coordination, whereof the number indicates the number of unique interlayers in the structure (P2: A-B-A-B vs P3/O3: A-B-C-A-B-C). Metal-layered oxides can be further modified with anions such as PO_4^- to increase the working voltage of the cell and its cycling stability. Polyanionic-type compounds, represented by sodium superionic conductors (NASICON), have large channels, high structural stability and allow fast ion insertion. The most common NASICON material is $Na_3V_2(PO_4)_3$ (NVP), which can show long cycling and high capacity retention at high charge/discharge rates. This material can be further improved by replacing one PO_4^{3-} polyanion with 3 F^-, resulting in $Na_3V_2(PO_4)_2F_3$ (NVPF), which offers a theoretical capacity of 128 mAh g e^{-1}, equaling energy density above 500 Wh kg^{-1} when combined with an ideal Na metal anode. These materials are considered rather promising for high-voltage cathodes.[48,49]

Among the positive materials for SIBs, Prussian White (PW) cathodes are also of special interest. PW cathodes belong to the Prussian Blue analogues family (PBA, $A_{0\text{-}2}B[B'(CN)_6]$), but have a high sodium and low vacancy content. PW often forms distorted, rhombohedral (R3) phases with the formula $Na_{1.92}Fe[Fe(CN)_6]$.[50,51] A cooperation between Altris and Northvolt focused on commercializing low-cost SIBs with PW as cathode material, which can be produced from non-toxic, globally abundant, and low-cost raw materials. These PW-based SIBs are not aiming to achieve high operation voltages or high specific energies, they are designed to take advantage of the cheap and local production, long cycle life, and good rate capability of PW.

Several companies, such as Contemporary Amperex Technology Co., Ltd. (CATL), Build Your Dreams (BYD), HiNa, and Faradion, manufacture SIBs, employing different layered oxides as positive and hard carbon as negative material. However, a cost comparison of the commonly used NMC811 and LFP-based cathode materials for LIBs with polyanion, layered oxide, and PW cathode materials for SIBs by Wood Mackenzie[52] in 2023 (Figure 2.8) revealed that PW ($Na_2Fe[Fe(CN)_6]$) is outperforming the other cathode materials in terms of price per Watt hour (Wh) since it is cheap to produce and comes with a high specific energy. Additionally, it is environmentally friendly,

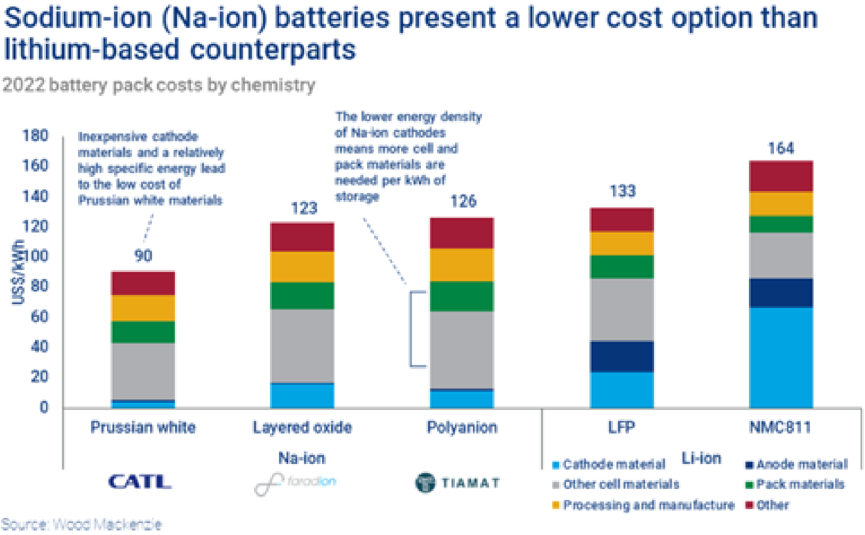

Figure 2.8: Cost analysis of LIBs and SIBs using different cathode materials, such as layered oxides, phosphates and PW. Reprinted from ref.[52]

2.3.2 Sodium-Metal Batteries

SMBs partially avoid the anodic charge-insertion bottleneck by utilizing sodium-metal in combination with a high-performance positive electrode such as PW. Sodium-metal has a high theoretical specific capacity of 1166 mAhg^{-1}, which is 3-fold higher than the most used insertion-type anode material (HC).[10,53] However, sodium-metal as negative material is more demanding during cycling compared to other electroactive negative materials. Na ions are directly removed from the surface during the discharge process (stripping), and deposited on the surface (plating) upon charging, creating an uneven surface that becomes more textured during cycling and forming mountain-like structures (dendrites). These dendrites can grow until they penetrate the separator to establish a direct contact between both electrodes, resulting in the short circuit of the cell (Figure 2.9).

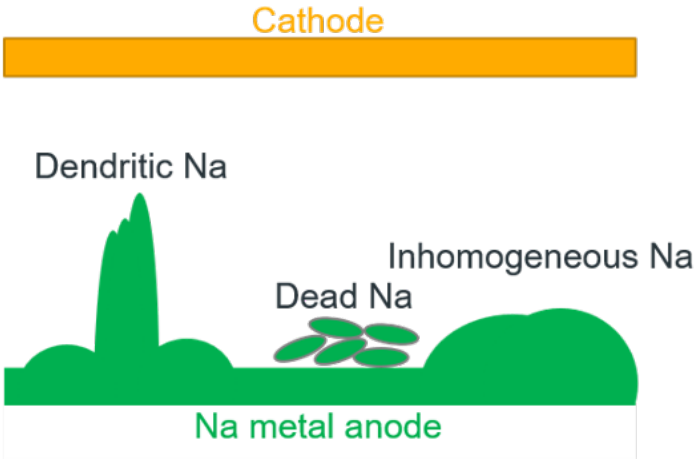

Figure 2.9: Common side reaction in SMBs.

Such short circuits can have dangerous consequences, potentially leading to fire outbreaks or even explosions in the worst case. Usually, the electrolyte would decompose, forming a passivation layer during the first cycles that should be stable for ongoing cycles and conduct Na ions. However, in the case of sodium-metal this SEI is repeatably stripped off, resulting in ongoing electrolyte decomposition and dynamic SEI behavior. The continuous SEI formation consumes Na ions and results in a partial enclosure of sodium-metal particles that are not connected to the sodium-metal bulk, both contributing to reduce the Coulombic efficiency of the cell. Additionally, the strong reactivity of sodium-metal can cause further side reactions with the electrolyte during cycling.[15]

Most commercial electrolytes are based on either ether or carbonate solvents.[54] However, carbonate-based electrolytes are not stable in sodium-metal-based cells upon prolonged cycling[55] and ether-based electrolytes are vulnerable to oxidation (stable up to 4 V vs Na^+/Na), thus limiting the voltage range that can be used during cycling. Both solvent families bear safety risks due to their volatility, flammability and toxicity.[56] The thermal stability is rather important, since high charge/discharge rates tend to generate heat inside the cell. This can lead to a thermal runaway when the SEI on the anode is failing enabling further heat generation via the reaction of the sodiated anode and the electrolyte. The volatile electrolyte becomes gaseous, resulting in a pressure build-up which could produce cell leakage or lead to an explosion of the battery in the worst case that oxygen is also release at the desodiated cathode. Moreover, some ether components themselves are dangerous or toxic, which poses an issue during cell assembly and for potential cell recycling at the end of life (EOL) of the battery, as well as during any form of accidents where the electrolyte may leak into the environment. Last, the use of liquid electrolytes does not prevent dendrite growth, which again bears the risk of short circuits, cell heating and thermal runaway.

Chapter 2.4
Solid-State Electrolytes

SMBs exhibit great potential, but the discussed safety risks and dendrite formation limit their practical application. However, these hurdles can be suppressed by using electrolytes with high mechanical strength, such as solid-state electrolytes (SSEs), and uniform, homogeneous, and reversible sodium stripping and plating.[57–63] SSEs are solid, rigid, non-flammable electrolytes, often having excellent chemical, electrochemical, mechanical, and thermal stability compared to liquid solvent-based electrolytes.[64] Replacing the potentially hazardous liquid electrolytes with SSEs may reduce the risk of dendrite formation, short circuits, leaking solvents, and thermal runaways. Furthermore, SSEs can potentially reduce the amount of dead sodium and increase the energy density of the battery by replacing the thick separator, which contains the liquid electrolyte, with a thinner SSE. However, SSEs come with their disadvantages, such as their generally lower ionic conductivity at room temperature (RT, below 1 mS cm^{-1}) compared to liquid electrolytes (1 - 10 mS cm^{-1}). SSEs can be roughly divided into three categories depending on their components: i) inorganic (ceramic) electrolytes, ii) organic (polymer) electrolytes and iii) composite/hybrid versions of the former two. Inorganic ceramic electrolytes, either oxide- or sulfide-based and often brittle, require high pressure to achieve good contact with the electrodes, and their production is difficult to scale up. In contrast, polymer electrolytes and polymer-rich hybrid materials are relatively "soft" and flexible, not requiring high pressure to establish good contact with the porous positive material and the sodium-metal surface.[65]

2.4.1 Solid-State Polymer Electrolytes

Solid-state polymer electrolytes (SSPEs) provide high thermal stability, mechanical flexibility, a cost-effective and light-weight design (depending on the exact chemistry), high safety, and good processability, and they can compensate for volume changes of the electrode during charging and discharging due to their flexible nature.[66] Typically, SSPEs consist of long polymer chains that can support ion transport through segmental motion.

Most SSPEs are semi-crystalline, featuring crystalline domains as well as amorphous, disordered regions. Still, the morphology can be more crystalline for more linear polymers and more amorphous for, e.g., branched polymers. The mobility of the polymer chains is crucial for ionic transport, as ions are "hopping" from one coordination site to the next unoccupied coordination site, either in the same chain (intrachain hopping) or to another chain (interchain hopping) to travel from one electrode to the other. This hopping effect is more favorable if most of the chains are amorphous and not crystalline; thus, the operation temperature of most SSPEs is often elevated to retain the majority of the polymer electrolyte in amorphous condition.[67,68]

Armand and Berthier discovered the first and most well-known SSPE in 1983.[69] They proposed a combination of poly(ethylene oxide) (PEO) with alkali metal salts as SSPE. PEO shows a high ion dissociation capacity thanks to the strong interactions between the metal salt and the polymer ether oxygens, which can provide additional hopping sites that create ion-conducting pathways for ion conduction.

Follow-up studies investigated different polymers and different salts to improve the ionic conductivity further and to overcome the issue of PEO being crystalline at RT. Some of the investigated polymers are polyacrylonitrile (PAN),[70] poly(vinyl alcohol) (PVA),[71] poly (vinyl chloride) (PVC),[72] poly(vinyl pyrrolidone) (PVP)[73] or poly carbonates, which also form polymer-salt complex, all of which have individual advantages and drawbacks.[74] The impact of the composition and the amount of salt in the polymer electrolyte on the PEO system was studied using different salts such as $NaClO_4$,[75] NaFSI[76] or NaTFSI.[77–79] Especially good performance is achieved when using fluorinated anions (NaTFSI and NaFSI), as their plasticizing effect decreases the crystallinity and their charge delocalization increases the number of free charge carriers in the electrolyte (fewer ion pairs), thus improving the ionic conductivity of the SSPE. PEO-based systems offer a good thermal stability compared to liquid electrolytes, but they still suffer from concentration gradient build-ups, high crystallinity and poor ionic conductivity compared to liquid electrolytes at RT.

2.4.2 Quasi-Solid-State Polymer Electrolytes

SSPEs are theoretically the best option when looking for the ideal safe electrolyte, due to their high mechanical and thermal stability. However, their ionic conductivity at RT is not excellent (10^{-5}-10^{-8} S cm^{-1}) limiting their practical application.[80,81] Thus, it becomes necessary to either increase the temperature to boost their ionic conductivity or to transform them into quasi-solid-state polymer electrolytes (QSSPEs) through the addition of plasticizers such as, e.g., ethylene carbonate (EC), propylene carbonate (PC), dimethyl carbonate (DMC), diethylene carbonate (DEC) or comparable carbonates.[82] Increasing the operation temperature for SMBs is problematic, as sodium-metal itself has a melting point of 98 °C. Higher temperatures would melt the negative electrode and destroy the SEI. Following, the use of plasticizers to form QSSPEs poses a more attractive alternative for practical applications of polymer electrolytes for SMBs.

QSSPEs combine the advantages of liquid and SSEs, showing high ionic conductivities, excellent electrode compatibility and increased mechanical stability.[80] QSSPEs are produced by incorporating a certain amount of plasticizer into the polymer system, however, the concentration must remain low so that the risk of leaking solvents is minimized. QSSPEs, in general, have already been known since 1975[83] and were first commercialized in 1996 for LIBs as a mixture of PVDF-HFP with 60% liquid plasticizers (1M $LiPF_6$ in EC/PC or EC/DMC),[84] while the development of QSSPEs for SIBs or SMBs began 10 years ago and is still in its early phase.[80] Recent developments in QSSPEs mainly focused on meeting the requirements for wearable devices by increasing the toughness, stretchability and compressibility of QSSPEs. The properties of a QSSPE mostly depend on the properties of the host polymer that is used to produce the QSSPE, including:

1. the flexibility and softness of the polymer film (improving the contact area),
2. the segmental motion of the polymer chains (improving the ionic conductivity)
3. the concentration and strength of functional groups that promote salt dissolution (also improving the ionic conductivity)
4. the glass transition and degradation temperature (improving the optimal and maximum operation temperature)
5. the molecular weight and amount of cross-linking (improving the mechanical stability)
6. the electrochemical stability (improving the usable voltage range).[81]

QSSPEs can exhibit different types of conductivity, including protonic, alkaline, conducting salt-based, or ionic liquid-based conductivity. The conductivity of these host materials is improved by adding a component with a high dielectric constant that boosts the conductivity through ion dissociation as well as through forming a smooth and stable interface with both electrodes.

Chapter 2.5
Single-Ion Polymer Electrolytes

SIPEs are a special class of polymer electrolytes for which the cation is the only mobile species, while the anion (or anionic center) is covalently bound to the polymer backbone via a spacer arm, rendering it effectively immobile (Figure 2.10). The anion immobilization results in high transference numbers close to unity, allowing for a more efficient transport compared to dual-ion polymer electrolytes. Moreover, a high transference number counteracts the build-up of a concentration gradient, thus facilitating high charge/discharge current rates without producing high internal resistances or elevated temperatures.[55,66] Additionally, SIPEs also suppress dendrite growth by homogenizing the sodium-metal deposition upon plating. A target study for QSSPE batteries revealed that polymers with a low transference number of ∼0.2 would need to reach 5 mS cm^{-1}, while QSSPEs with a transference number close to unity only require 0.4 mS cm^{-1} to be applicable for EVs.[85,86]

SIPEs are easily tunable as the components themselves, as well as their respective ratios can be easily changed to adapt to various requirements; for example, the SIPE's thickness and mechanical stability can be increased to support batteries that undergo a lot of physical stress, while chemical components can be modified to support, e.g., a higher or lower temperature operation range, a higher or lower voltage window, etc..[87–93]

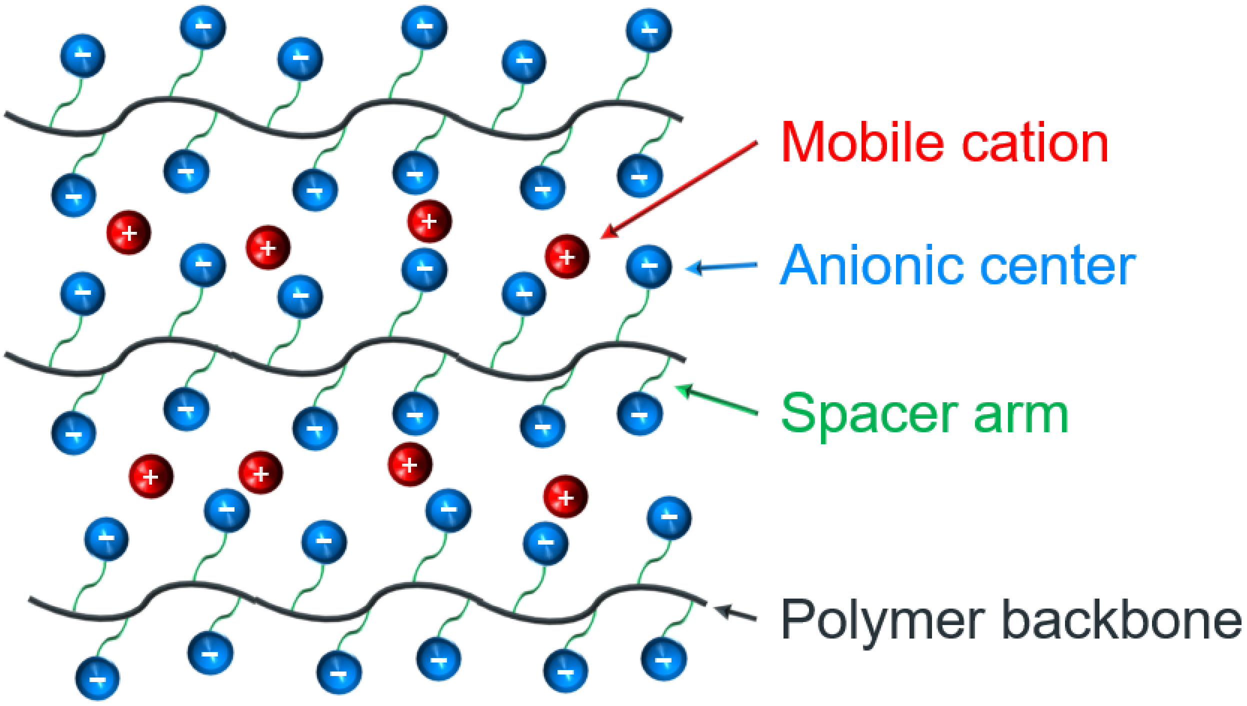

Figure 2.10: Schematic presentation of SIPEs. The anionic center (blue) is tethered to the polymer backbone (black) via a spacer arm (green), while the cation (red) is mobile.

SIPEs can be synthesized through various methods, such as homo-polymerization, co-polymerization or the modification/functionalization of an existing polymer, which all share the goal of linking the anionic center to the polymer backbone. SIPEs can further be swollen with plasticizers resulting in quasi-solid-state single-ion polymer electrolytes (QSS-SIPEs) that combine the discussed advantages of QSSPEs with the benefits of SIPEs. The properties of the QSS-SIPEs mainly depend on the properties of the SIPEs as well as the amount of added plasticizers, as assessed by Mayer et al..[86]

The key aspect of designing a SIPE that also determine its electrochemical properties are i) the chemistry, flexibility, and interconnection of the backbone, ii) the chemistry, size, and flexibility of the spacer arm that connects the anionic center to the backbone and iii) the chemistry, strength, and accessibility of the anionic center, as well as the properties of additives, such as supporting polymers or plasticizers.

2.5.1 Influence of the Anionic Center

The ionic conductivity of a SIPE strongly depends on the mobility of the cation, which, in turn, depends on its binding strength towards the anionic center. The binding strength between cation and anion depends on the delocalization of the negative charge in the anionic center, where a higher delocalization supports a higher ionic conductivity because the cation can move with fewer restrictions. Various anionic groups are reported in the literature, but they can be mainly categorized into carboxylate (-CO_2^-), sulfonate (-SO_3^-) and sulfonylimide (-$SO_2N^-SO_2$-) groups with only a few exceptions.[94]

The size and strength of the anionic group impacts how strong it binds the cation, which can be described by their dissociation energy (ΔE_D). The dissociation energies of the different anionic groups with lithium as cation was calculated using DFT calculations by Maria et al. using a modified styrene molecule as salt monomer (Figure 2.11).[95] The highest required dissociation energy was obtained for the carboxylate (-CO_2-) group of lithium 4-vinylbenzoate (LiSC, 699 kJ mol^{-1}), followed by the sulfonate (-SO_3-) group of lithium 4-styrenesulfonate (LiSS, 639 kJ mol^{-1}), the trifluoromethanesulfonylimide (-SO_2N^--SO_2-CF_3) group of lithium 4-styrenesulfonyl (trifluoromethanesulfonyl)imide (LiSTFSI, 625 kJ mol^{-1}) and lastly the dicyano methanide (-$C^-(CN)CF_2$) group of lithium 4-styrenesulfonyl(dicyano)methide (LiSDM, 511 kJ mol^{-1}). These calculations suggest that the dicyano methanide and TFSI group may be promising anionic centers for SIPEs.

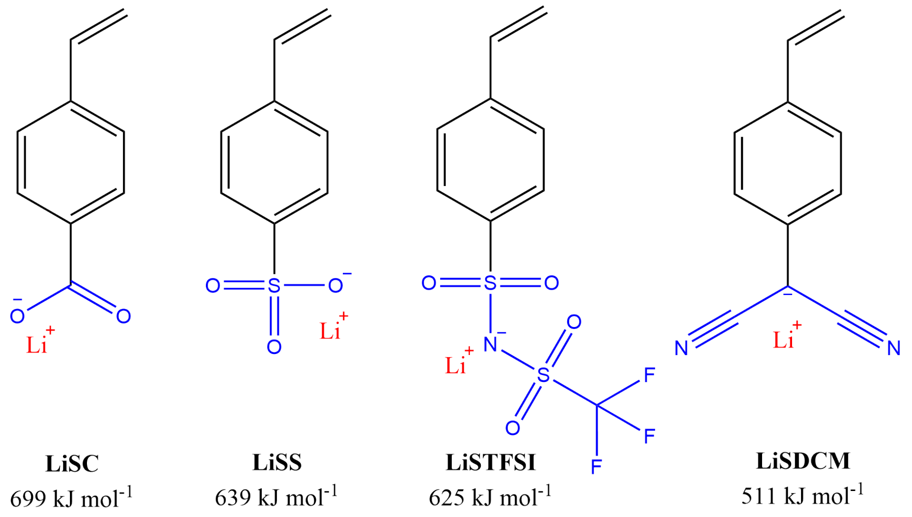

LiSC
699 kJ mol^{-1}

LiSS
639 kJ mol^{-1}

LiSTFSI
625 kJ mol^{-1}

LiSDCM
511 kJ mol^{-1}

Figure 2.11: Chemical structure and dissociation energies of lithium salt monomers with different ionic centers (blue). Reprinted from ref.[95]

2.5.2 Influence of the Spacer Arm

The ionic conductivity of the SIPE does not only depend on the charge delocalization of the anionic center itself but also on the chemical composition and flexibility of the spacer arm that tethers the anionic center to the backbone.[96] Commonly used spacer arms are either PEO-, CF_2- or Styrene-based (Figure 2.12). A higher flexibility of the spacer arm is expected to increase the mobility of the anionic center and following reducing the distance the cations have to move between, resulting in a higher ionic conductivity.[97] However, the exact influence of each spacer arm on the SIPE's performance is not fully cleared, as the anionic center and the backbone would need to be identical, for a good comparison.[96]

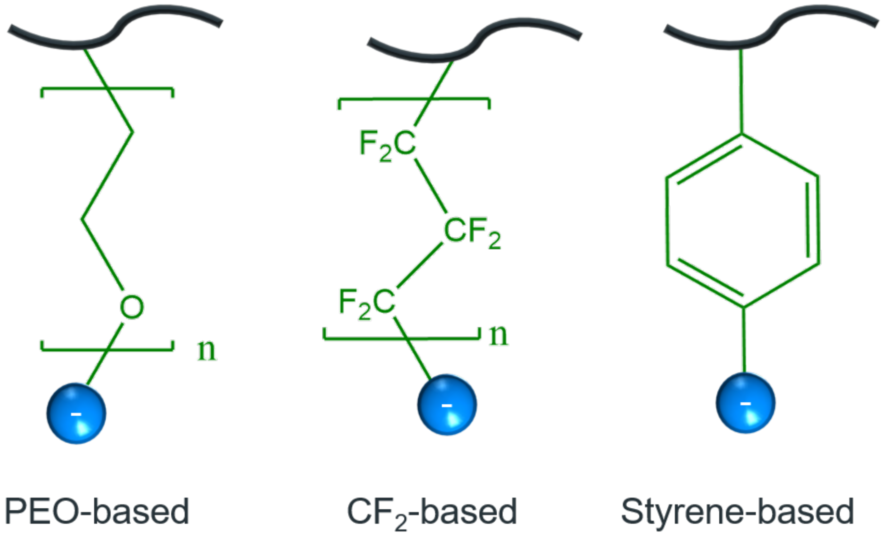

Figure 2.12: Chemical structure of common spacer arms.

2.5.3 Influence of the Backbone

The backbone of the SIPE determines its mechanical, thermal and electrochemical stability, as well as the plasticity, the porosity and many more properties of the final SIPE.[97] Backbones can be divided into inorganic, organic and hybrid backbones. The most common backbones are long linear chains that are either copolymers (consisting of a conducting salt monomer and copolymerizing agents)[98–100] or Si-O-based.[101–104] Linear backbones often suffer from high crystallinity and reduced mechanical stability (especially in QSS-SIPEs). However, a recent study by Zhong et al.[82,105] developed a cross-linked polymer backbone using pentaerythritol tetrakis(3-mercaptopropionate) (PETMP) and pentaerythritol tetraacrylate (PET4A) that offers high stability and good ionic conductivity in Li-based cells (Figure 2.13).[82,105] The SIPE can be synthesized out of LiSFSI, PETMP, and PET4A (LFPP) by cross-linking the components around an electrospun PVDF-HFP membrane using UV light. The cross-linked backbone, flexible spacer arms and the TFSI anionic group result in an "ultra-high" ionic conductivity of 5.81 mS cm^{-1} at 28 °C, which is comparable to liquid electrolytes and outperforms various other recently reported Li-based SIPEs, posing as an interesting candidate for Na-based SIPEs. The LFPP SIPE was cycled for 230 cycles at 0.2C in a Li||LFP cell and potentially offers a better cyclability compared to liquid electrolytes in the same cell setup.[82,105]

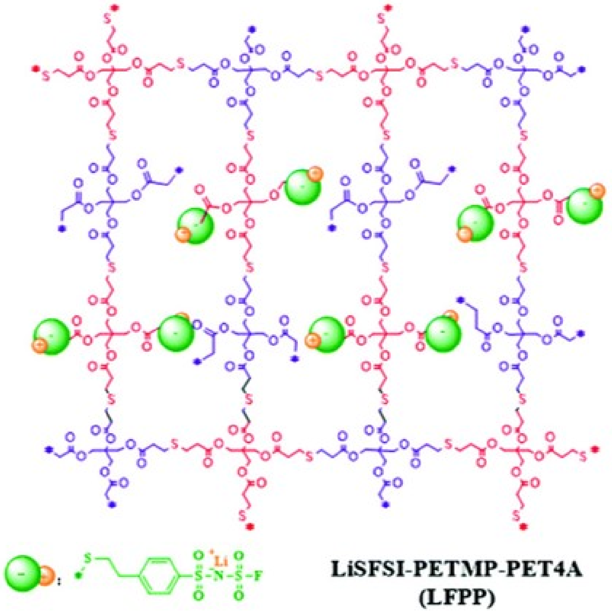

Figure 2.13: Cross-linked structure of the LiSFSI-PETMP/4A-SIPE. Reprinted with permission from ref.[82]

2.5.4 Sodium-based SIPEs

SIPEs are a relatively new field of research, with most SIPEs being optimized for lithium-based SIPEs instead of sodium-based SIPEs.[94] Dong et all. synthesized a multi-block polymer electrolyte that uses a linear backbone of functionalized benzene rings together with a highly fluorinated $CF_2CF_2OCF_2CF_2$ spacer arm and a TFSI anionic group, resulting in a high ionic conductivity exceeding 1 mS cm^{-1}, a potential window from 0 to 4.1 V vs Na^+/Na and a cycling stability of 1000 cycles at 0.2C, when using a $Na||Na_3V_2(PO_4)_3$ cell.[104] The SIPE by Olmedo-Martineu et al.[106] blends PEO with poly(sodium 1-[3-(methacryloyloxy)propylsulfonyl]-

1-(trifluoromethanesulfonyl) imide) (PNaMTFSI) using a CH_2 backbone, a $COO(CH_2)_3$ spacer arm and a TFSI anionic center to reach $7.74 \cdot 10^{-5}$ S cm^{-1} at 85 °C and can be used up to 4.5 V vs Na^+/Na. Das et al.[107] investigated a SIPE with a linear C-C based backbone with an attached $-CO_2^-$ group and an attached $-NHSO_3^-$ group, obtaining an ionic conductivity of $1.81 \cdot 10^{-5}$ S cm^{-1}, an electrochemical stability window up to 4.8 V vs Na^+/Na and cycling for 200 cycles at 0.1C using Na||NVP cell. Cross-linked SIPE backbones are a recent discovery, especially for SMBs. A cross-linked sodium bis(fluoroallyl)malonato borate and sodium tri-thiol (trimethylolpropane tris(3-mercapto propionate) SIPE was assessed by Liu et al. reaching an ionic conductivity of 2.0 mS cm^{-1} at RT, a potential window up to 5 V vs Na^+/Na and 150 cycles at 0.5C in a Na||NNMO cell (Table 2.1).[108]

Table 2.1: Table of Na-based SIPEs in the literature

Spacer arm	Anion	Conductivity	Temp.	Capacity retention	source
CF_2-based	TFSI	$2.6 \cdot 10^{-3}$ S cm^{-1}	30 °C	85% after 1,000 cycles	[104]
CH_2-based	TFSI	$\sim 2 \cdot 10^{-6}$ S cm^{-1}	30 °C	not tested	[106]
CH_2-based	SO_3^-	$1.8 \cdot 10^{-5}$ S cm^{-1}	RT	82% after 45 cycles	[107]
-	BO_2	$2 \cdot 10^{-3}$ S cm^{-1}	30 °C	87% after 150 cycles	[108]
-	BO_2	$9.4 \cdot 10^{-4}$ S cm^{-1}	30 °C	72% after 500 cycles	[109]

The variety of investigated anionic groups, spacer arms, and backbones suggests that multiple factors influence the performance of SIPEs. A deeper understanding of the different influencing factors has to be generated to enable a targeted optimization of the next generation of safe and environmentally friendly QSS-SIPEs for SMBs.

Motivation and Aim

Our modern world evolves at a rapid pace, powered by electricity in all kinds of applications. However, this energy mainly comes from fossil fuels, which are now seen as more critical due to their environmental impact and their limited availability over the next centuries. Consequently, renewable energy sources have been a major focus of recent scientific advances and are now widely available for producing green and environmentally friendly energy. This green energy has not yet replaced fossil fuels, despite the fact that it can already be mass-produced in large amounts.

Renewable energy sources cannot be relied upon consistently due to their inherent fluctuations. Therefore, large-scale storage solutions are essential to balance low and high production phases. The currently dominant LIBs represent one of the most obvious choice to solve this issue. However, they struggle with the necessary up-scaling because lithium, as well as some lithium battery components such as cobalt and nickel, are critical raw materials and expensive. Hence, there is a crucial need to discover and establish more environmentally friendly alternatives.

The most promising candidates are sodium-based batteries, as they provide a high energy density and can be produced from abundant materials all around the world. A major concern for large-scale grid storage systems is not only their environmental impact but also their safety, with the highest risk originating from the carbonate-based liquid electrolyte, as it determines much of the cell's chemistry, including SEI formation, thermal and electrochemical stability, and many aspects of the battery's overall safety. Polymer electrolytes, especially SIPEs, offer promising properties to realize safe, cheap, and environmentally friendly large-scale grid storage applications. However, these electrolytes are still not well researched, which is why this work aims to generate in-depth knowledge about the chemistry-dependent properties of SIPEs for SMBs.

The goal of this work was to create a deeper understanding of how the SIPE's components determine the electrochemical, thermal, and mechanical properties and how they can be optimized to realize mass-producible SMBs with outstanding electrochemical and thermal properties in the future. All synthesized SIPEs were electrochemically and thermally characterized, and validated in proof-of-concept SMBs. The SIPEs form a three-dimensional structure and initially consist of PETMP, PET4A, PVDF-HFP, and 50 weight percent (wt%) of molecular transporters (i.e., EC:DMC:FEC, 49:49:2 wt%). Enhanced insights into the component-driven influence on the properties of the SIPE were gained, including the influence of i) the anionic center (Chapter 5.3), ii) the spacer arm (Chapter 5.4) and iii) the backbone (Chapter 5.5) of the SIPE.

Materials and Techniques

Chapter 4.1

Materials

4.1.1 Materials for Synthesis

Thionylchloride(99.7%), trifluoromethanesulfonamide (96%) and magnesium sulfate (99.5%) were purchased from Thermo Scientific, while dimethylformamide (DMF, 99.8%), dichloromethane (DCM, $> 99\%$), acetonitrile (99%) and triethylamine ($> 99\%$), methanol (99.9%) and dimethyl sulfoxide (DMSO, $> 99\%$) were purchased from VWR chemicals. Sigma-Aldrich supplied 4-tert-Butylcatechol ($> 99\%$), sodium 4-vinylbenzenesulfonate (NaVBS, $> 90\%$) and sodium carbonate ($> 99.5\%$). PETMP (97%), PET4A (99%) and PVDF-HFP (99%) azobisisobutyronitrile (AIBN, 98%) were obtained from Merck. 5-Iodooctafluoro-3-oxapentanesulfonyl fluoride (95%) was purchased by Matrix Scientific. Sodium ((3-acetoxypropyl)sulfonyl)-((trifluoromethyl) sulfonyl)amide (NaMTFSI) was purchased from Specific polymers. 4-Bromo-1-buten (98%) was purchased from across organics. Alfa Aesar was contacted for malononitrile (99%) and 3-sulfopropyl methacrylate potassium salt was purchased from TCI.

4.1.2 NMR Solvents and Plasticizers

The solvent used for the NMR spectroscopy measurements was DMSO, purchased from VWR (DMSO-d6, 99.8% + 0.03% (v/v) TMS). The used plasticizers were purchased from Aldrich (ethylene carbonate (99%), dimethyl carbonate (99.9%) and fluoroethylene carbonate, (99%)).

4.1.3 Purifications

The synthesized chemicals were purified as described in their experimental procedures, while all commercial chemicals except AIBN were used without purification. AIBN was purified by recrystallization. First, AIBN (5g) was dissolved in dry Methanol at 45 °C, filtrated hot (to remove solid impurities), cooled down to 4 °C (to precipitate AIBN), filtered again (thus removing remaining impurities in the liquid phase), before the remaining Methanol was removed in vacuum. The obtained crystalline AIBN was stored in the fridge at 4 °C until later use.

Chapter 4.2
Synthesis of the Sodium Salt Monomers

4.2.1 Synthesis of the NaSTFSI monomer

Sodium 4-styrenesulfonyl(trifluoromethanelsulfonyl) imide (NaSTFSI) was synthesized using a two-step synthesis route (Figure 4.1).[110] A solution of thionylchloride (44 mL, 606 mmol, Thermo Scientific, 99.7%) in dry dimethylformamide (DMF, 200 mL, VWR chemicals, 99.8%) was prepared under Ar atmosphere by stirring both components together for 3 h at RT. The solution was cooled before adding the inhibitor 4-tert-butylcatechol (600 mg, 3609 mmol, Sigma-Aldrich, $>$ 99%) followed by the slow addition of the educt sodium 4-vinylbenzenesulfonate (NaVBS, 16 g, 78 mmol, Sigma-Aldrich, $>$ 90%). The solution was stirred for 16 h at RT and cooled in the fridge at 4 °C for 24 h. The obtained solution was slowly dropped into an ice-cooled solution of water (100 mL) and dichloromethane (DCM, 100 mL, VWR chemicals, $>$ 99%). The DCM phase was collected, while the water phase was washed twice with DCM ($2 \cdot 50$ mL). The DCM phases (VBSC) were combined and the solvent was removed in vacuum at 50 °C and the residue was cooled before adding acetonitrile (120 mL, VWR chemicals), trifluoromethanesulfonamide (15 g, 53 mmol, Thermo Scientific, 96%) and triethylamine (200 mL, VWR chemicals, > 99%). The solution was stirred for 72 h, filtered, and the solvent was removed at 50 °C under reduced pressure. DCM (100 mL) was added to the obtained solution before being washed with cooled water (2x50 mL). The DCM phases were combined, and the solvent was evaporated at 50 °C under reduced pressure. Sodium carbonate (18 g, Sigma Aldrich, > 99.5%) and dry methanol (100 mL) were added before the solution was stirred for 24 h at RT. The precipitate was removed using a centrifuge, and the solvent was evaporated. The resulting precipitate was washed twice with acetone (25 mL) and dried in air to obtain NaSTFSI (4.2 g, yield = 17%) as an off-white solid.

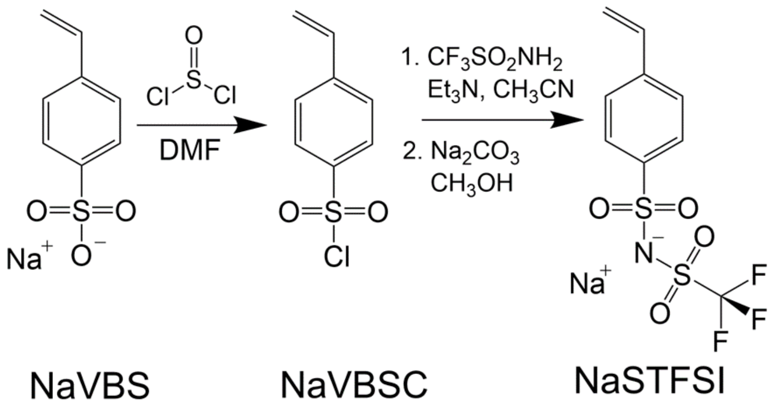

Figure 4.1: Synthesis procedure of the synthesized NaSTFSI.

The structure of the in-house synthesized sodium salt monomers was verified using ^{1}H-, ^{13}C- and ^{19}F-NMR spectroscopy.[110] The ^{1}H-NMR of NaSTFSI (Figure 4.2) shows the four benzyl proton doublets at 7.5 ppm, followed by the double doublet at 6.74 ppm. Last, the protons of the double bond are shown at 5.85 and 5.28 ppm as doublets, respectively. The ^{13}C-NMR shows all 9 carbon atoms between 110 and 150 ppm with the only exception of the terminal C of the double bond, which is shifted down to 50 ppm. Last, the ^{19}F-NMR shows all three fluor atoms at -79 ppm, which is in agreement with the literature.[110]

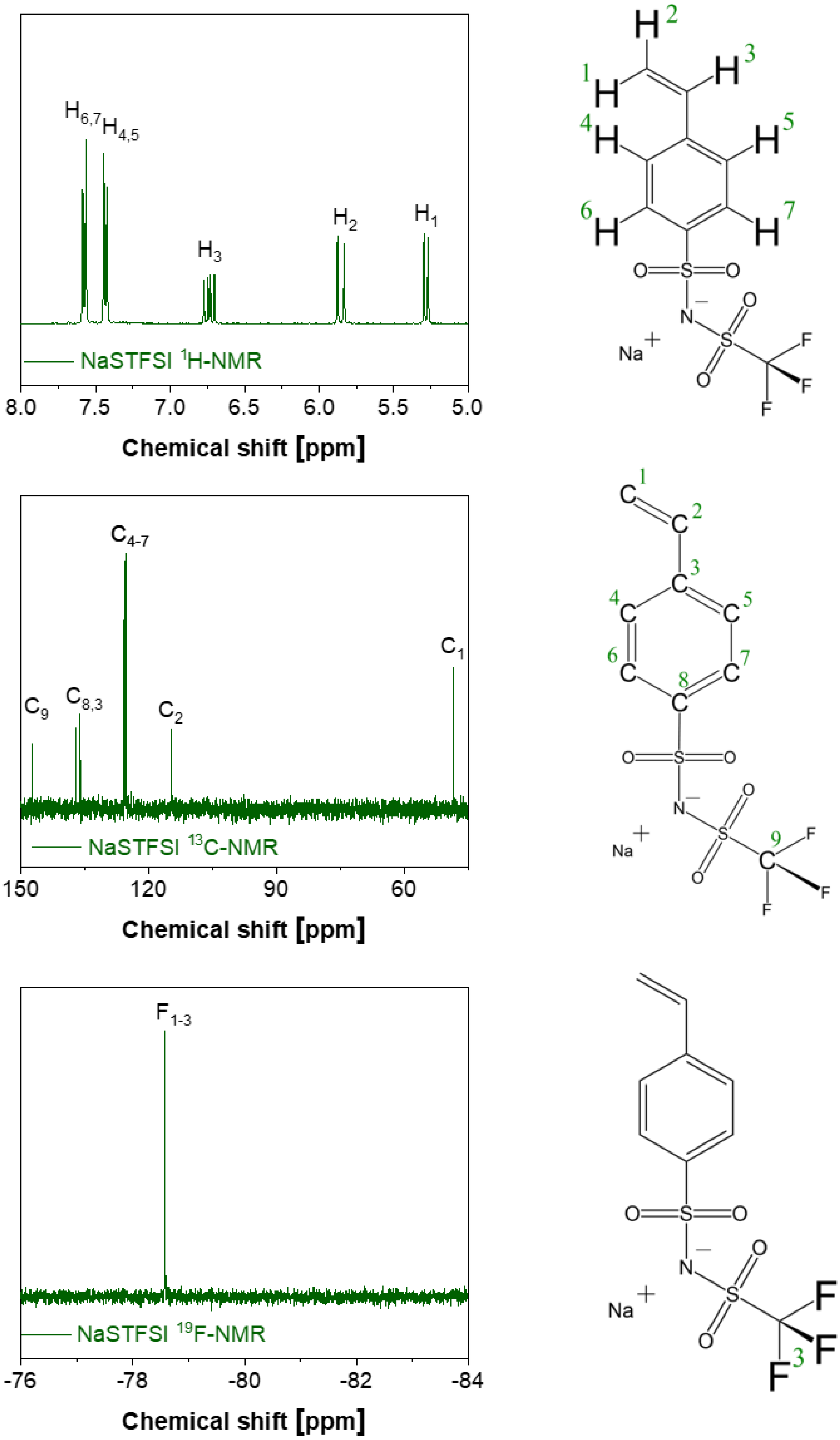

Figure 4.2: ^{1}H, ^{13}C and ^{19}F-NMR of the NaSTFSI monomer.

4.2.2 Synthesis of the NaSDCM monomer

Sodium (4 styrenesulfonyl)(dicyano)methanide (NaSDCM) was synthesized adapted from a procedure reported by Martinez-Ibanez et al. (Figure 4.3).[95] An oven-dried 100 mL Schlenk-flask equipped with a magnetic stirrer and a reflux condenser was filled with DMF (4 mL) and THF (30 mL), set under Ar atmosphere and cooled down to 0 °C. Consequently, thionylchloride (10.3 mL, 142 mmol, 5.7 eq.) was added, followed by tert-butylcatechol (80 mg, 0.5 mmol, 0.02 eq.). After stirring for 10 min, 6.67 g (32.3 mmol, 1.3 eq.) sodium p-styrenesulfonate salt was added in increments over a time frame of 15 min and the solution was stirred overnight. The reaction mixture was poured slowly in 40 mL ice-water in order to quench the remaining thionyl chloride, followed by extraction with DCM (3x20 mL). The collected organic phases were washed sequentially with 40 mL water and saturated aqueous sodium chloride solution. The solvent was removed in vacuo after drying over $MgSO_4$. The product was obtained as a yellowish oil (4.91 g, 1.0 eq., yield: 75 %), which was used without further purification by dissolving it in 40 mL anhydrous MeCN in a 250 mL two-neck Schlenk-flask equipped with a magnetic stirrer, reflux condenser and a rubber septum under Ar protection. 1.76 g (26.6 mmol, 1.1 eq.) malononitrile were added using a syringe prior to cooling to 0 °C. Whilst stirring, 16.9 mL TEA (121.1 mmol, 5 eq.) were added and the reaction mixture was stirred overnight. The solvent was removed in vacuo and the crude product was dissolved in 250 mL 1M NaOH (4 eq.) under stirring for 1 h. The solution was acidified by the dropwise addition of H_2SO_4, and extracted with 3x100 mL DCM. The solvent was again removed in vacuo, the product dissolved in 100 mL 4M NaOH and stirred overnight. Excess water was removed in vacuo, the product dissolved in MeCN and separated from left-over NaOH by filtration. After complete removal of the solvent in vacuo, 4.67 g product were obtained as a slightly yellow solid (yield: 81 %).

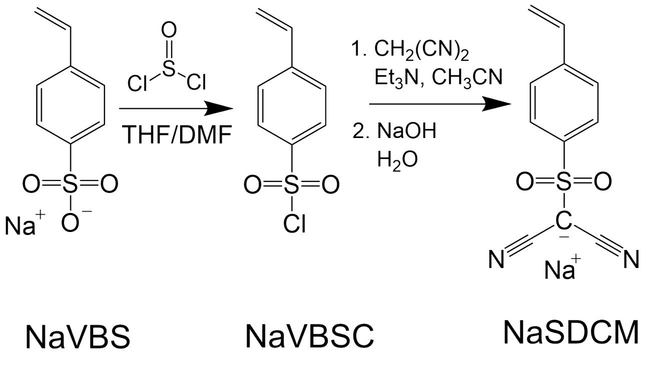

Figure 4.3: Synthesis procedure of NaSDCM.

The structure of the NaSDCM SSM was confirmed using ^{1}H- and ^{13}C-NMR spectroscopy.[95] The ^{1}H-NMR (Figure 4.4) shows the same signals as the NaSTFSI SSM. The four benzyl proton are showing around 7.5 ppm as doublets, the double doublet of H^{3} at 6.74 ppm and the protons of the double bond at 5.85 and 5.28 ppm as doublets, respectively. The ^{13}C-NMR shows 10 carbon atom signals between 110 and 150 ppm and the positive C of the anionic group at 40 ppm.[95]

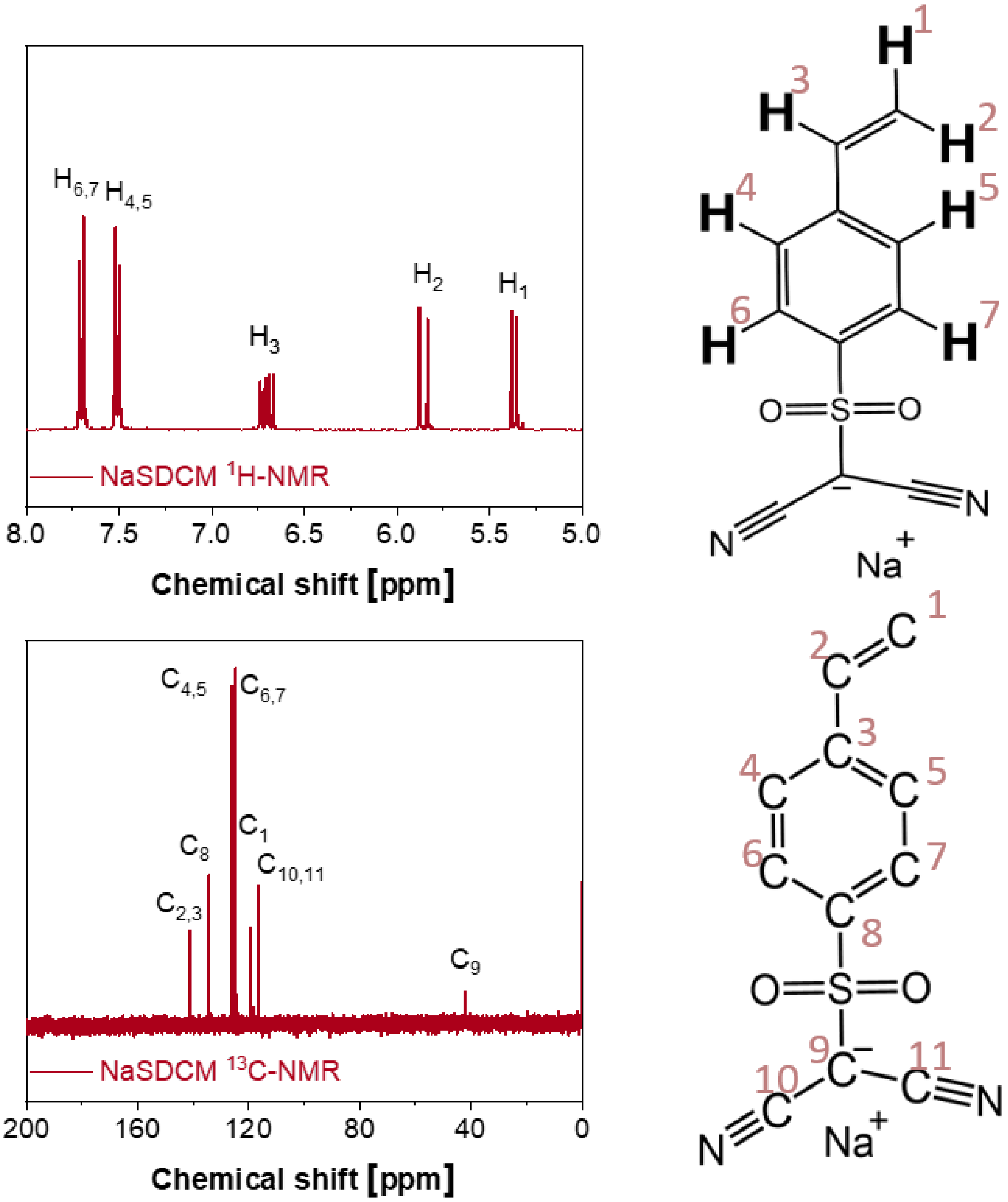

Figure 4.4: ^{1}H and ^{13}C of the synthesized NaSDCM monomer.

4.2.3 Synthesis of the NaFTFSI monomer

Sodium ((1,1,2,2-tetrafluoro-2-(1,1,2,2-tetrafluoro-2-iodoethoxy)ethyl)sulfonyl)((trifluoromethyl) sulfonyl)amide ($ICF_2CF_2OCF_2CF_2SO_2N$-(Na^+)SO_2CF_3 or NaFTFSI) was synthesized as described in the literature.[86] Trifluorosulfonamide (8g) was dissolved in acetonitrile (30 mL) together with TEA. The educt $ICF_2CF_2OCF_2CF_2SO_2F$ (I-FSC, 20 g) was slowly added and the mixture was stirred at 40 °C for 36 hours. The reaction was monitored by ^{19}F-NMR and worked up once the SO_2F peak at 44.77 ppm disappeared. The solvent was removed in vacuum at 40 °C and the organic phase was extracted in DCM, washed with water (500 mL) and dried over $MgSO_4$. The solvent was removed in vacuum again, resulting in a red oil, which was dissolved in 0.5M NaOH and stirred for 30 min. The organic phase was extracted with ethyl acetate, dried over anhydrous magnesium sulfate and the solvent was removed in vacuum at 40 °C again. The product was obtained as a yellow oil (yield: 52%).

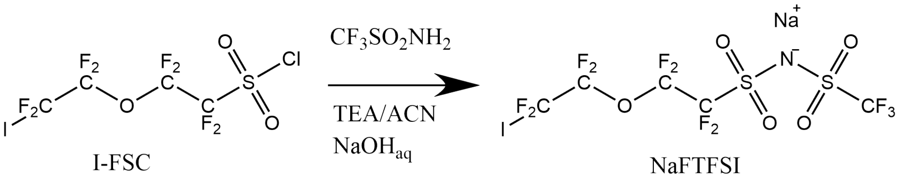

Figure 4.5: Synthesis procedure of NaFTFSI.

The structure of the synthesized NaFTFSI was verified using ^{19}F-NMR spectroscopy. The ^{19}F-NMR of NaFTFSI (Figure 4.2) shows five fluor doublets, starting with the I-terminal ICF_2 at -70 ppm, the CF_3 at -80 ppm, the ICF_2CF_2at -82 ppm, followed by the next CF_2 at -86 ppm and last the CF_2SO_2 at -117 ppm. These results are aligning with the literature.[86]

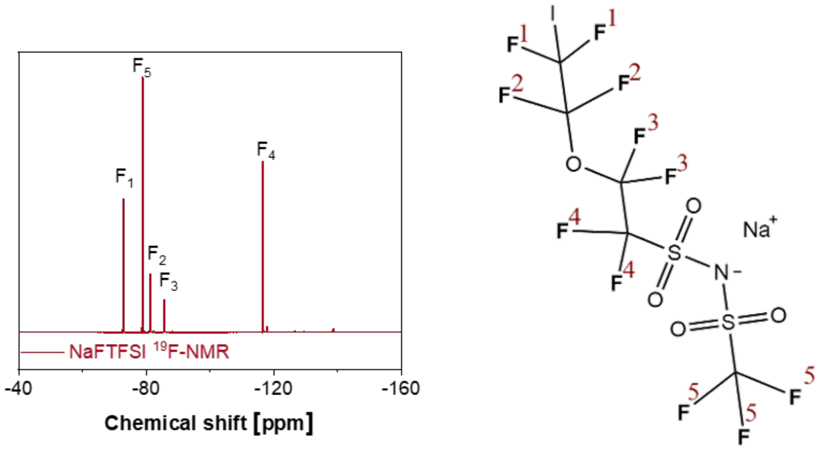

Figure 4.6: ^{19}F-NMR of the synthesized NaFTFSI monomer.

4.2.4 Synthesis of the NaMDCM monomer

Sodium dicyano((3-(methacryloyloxy)propyl)sulfonyl)methanide (NaMDCM) was synthesized out of 3-sulfopropyl methacrylate potassium salt. First, DMF (6 mL) and 3-sulfopropyl methacrylate potassium salt (15.6 g) were dissolved in THF (dry, 50 mL) and cooled to 0 °C. Next, thionyl chloride (27 mL) was stored in a dropping funnel and the aperture was set under Ar, before thionyl chloride was slowly dropped inside. The solution was stirred overnight (16h) while slowly warming up to room temperature. Ice-cooled water was stirred in a beaker and the solution was slowly dropped inside before DCM (50 mL) was used to extract the organic intermediate product. The organic phase was stirred over $MgSO_4$ and the solvent was removed in vacuum at 40 °C. Malononitrile (6 mL) was dissolved in acetonitrile (50 mL) and the solution was cooled and slowly added to the cooled extracted intermediate product. TEA (50 mL) was dropped to the solution under Ar through a dropping funnel and the combined solutions were stirred for 16 hours at RT. The solution was washed with $NaHCO_3$ (saturated, 80 mL) and HCL (1M, 100 mL, 2 times). The organic phase was extracted with DCM and the volatile components were removed in vacuum at 40 °C, followed by an additional drying step at -105 °C and $<$1 mbar (freeze dryer) for 16 hours. The obtained oil was dissolved in dry ethanol (50 mL) and stirred over Na_2CO_3 (16 g). The red-golden solution was filtered to remove unreacted Na_2CO_3 and the volatile components were removed in vacuum at 40 °C using a rotation evaporator to yield NaMDCM as a red viscous oil.

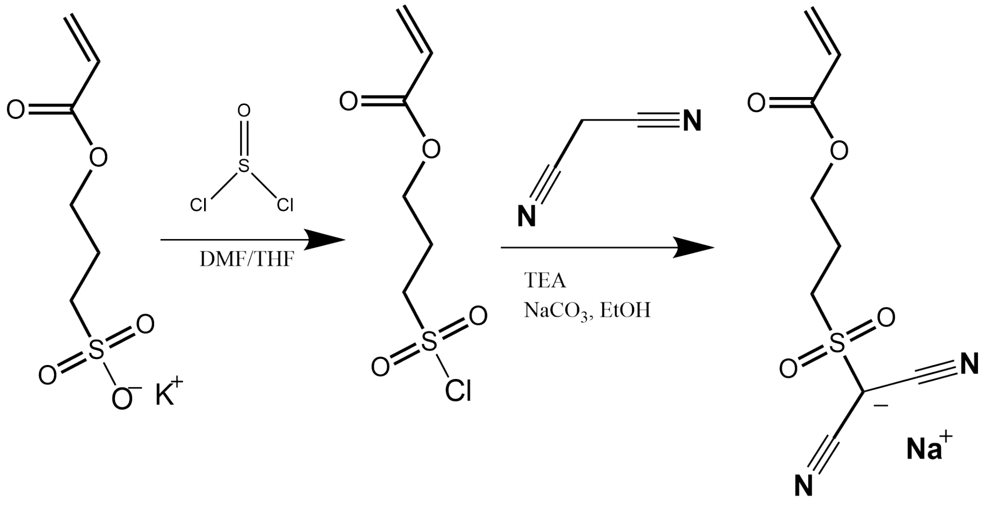

3-Sulfopropyl Methacrylate potassium salt

NaMDCM

Figure 4.7: Synthesis procedure of NaMDCM.

The structure of the NaMDCM SSM was investigated by ^{1}H- and ^{13}C-NMR spectroscopy, showing the C=C teminal protons around 6 ppm, the ester protons at 4.2 ppm, the CH_2SO_2 protons at 3.5 ppm, the -CC_2C- protons at 2 ppm and the CH_3 protons at 1.9 ppm. The ^{1}H-NMR additional features a water peak at 3 ppm, a DMSO peak at 3.5 ppm and TEA residues at 1.1 and 1.0 ppm (Figure 4.8). The ^{13}C-NMR shows the DMSO signal at 40 ppm and the TEA peaks at 55 and 10 ppm, respectively. The NaMDCM SSM has the C=C atoms at 140 and 130 ppm, while the CO_2 carbon has the highest peak at 165 ppm. the two cyano carbon atoms are at 120 ppm , while the carbon next to the oxygen is at 64 ppm. Last, the negative C$^-$ carbon is at 58 ppm, the carbon next to the sulfur group is at 47 ppm, the middle carbon of the -C-C-C- chain is at 23 ppm and the methyl carbon is at 20 ppm. All signals are matched with the NaMDCM SSM while the remaining containing solvents will be removed upon casting.

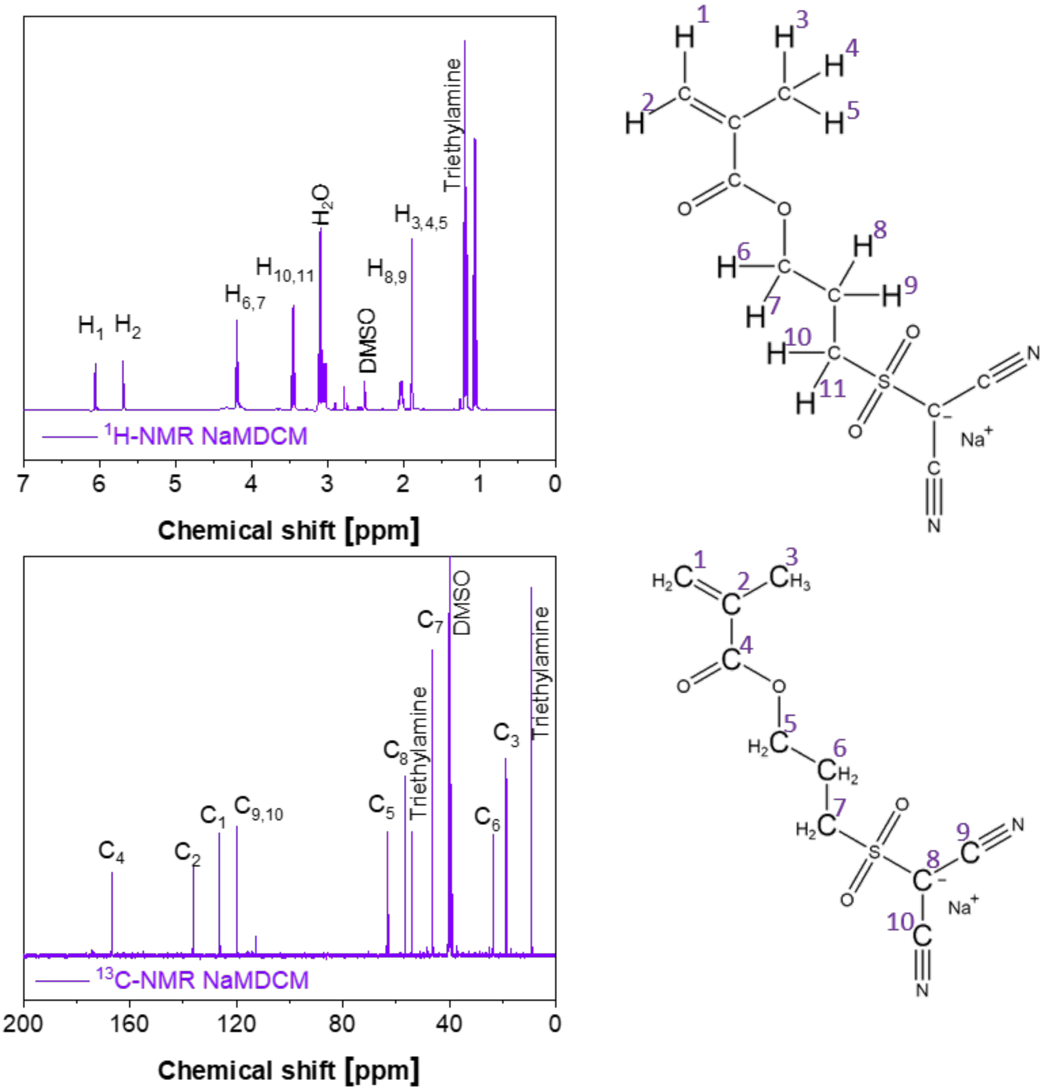

Figure 4.8: ^{1}H and ^{13}C of the synthesized NaMDCM monomer.

Chapter 4.3
Membrane Fabrication

4.3.1 NaSTFSI-SIPEs

NaSTFSI-SIPEs were prepared by solvent casting using DMSO (VWR chemicals, $>$ 99%) and DMF (VWR chemicals, 99.8%) mixture. First, the two networking monomers PETMP (500 mg, Merck, 97%) and PET4A (200 mg, VWR Merck, 99%) were dissolved together with PVDF-HFP (80 mg, Merck) in DMF (9 mL). In contrast, the NaSTFSI sodium salt monomer (70 mg) was dissolved in DMSO (3 mL) together with the thermal initiator azobisisobutyronitrile (AIBN, 9 mg, Merck, 98%). The two solutions were first stirred separately for 3 h, then mixed and stirred for an additional 2 h, and cast into a Teflon petri dish (62 mm ∅). The solution was covered with a perforated Al foil and heated to 70 °C for 28 h while the pressure was stepwise reduced to 10 mbar. This procedure resulted in self-standing NaSTFSI-co-PET-MP/4A membranes of 140 ± 40 µm. The NaSTFSI-co-PET-MP/4A membranes were cut into round discs (16 mm ∅) and further dried at 70 °C in vacuum for 3 h. The membranes were transferred in a glovebox ($O_2 < 0.1$ ppm, $H_2O < 0.1$ ppm) and swollen in a mixture of ethylene carbonate (Aldrich, 99%), dimethyl carbonate (Aldrich, 99.9%) and fluoroethylene carbonate (Aldrich, 99%) (EC:DMC:FEC, 49:49:2, vol%) (2 mL), at 60 °C for 48 h before they were used in a cell. The solvent uptake was 50 ± 4 wt%.

4.3.2 Membrane Fabrication using Alternative Components

The procedure described for the NaSTFSI-co-PET-MP/4A membranes was adapted for the fabrication of all other membranes described in this thesis. The sodium salt monomer NaSTFSI was exchanged through NaFTFSI, NaMTFSI, NaSDCM, NaVBS or NaMDCM, respectively to produce the accordingly labeled membranes, while PET4A was replaced with either PET6A, Dione or Trione to produce the membranes labeled accordingly. The ratio of solvents was changed to 7 mL of DMF and 2 mL of DMSO for the membranes that were synthesized in a non-vacuum oven, while the NaMDCM-based membranes were synthesized purely in 7 mL DMF. All obtained membranes were dried at 70 °C in vacuum for 3 h, transferred to the glovebox and soaked with molecular transporter as described above.

4.3.3 Membrane List

A list of all SIPE membranes used in this thesis, as well as their molar ratio and composition is shown in the following table. The NaSTFSI-SIPE was investigated in chapter 5.1. The SIPEs T1 to T5, P1 to P6 and M1 to M6 were used for a ratio optimization in chapter 5.2. The NaSTFSI, NaVBS and NaSDCM SIPEs were used in chapter 5.3 and the NaSTFSI, NaMTFSI and NaFTFSI SIPEs were investigated in chapter 5.4. Next, the Diene, Trione, PET4A and PET6A SIPEs were studied in chapter 5.5 and last, the NaMDCM SIPE was investigated in chapter 5.6.

Table 4.1: Membrane list of chapter 5.1 and 5.2

<table>
<tr><th></th><th colspan="4">Molar ratio [mol]</th><th>Composition [mol%]</th></tr>
<tr><td>SIPE label</td><td>NaSTFSI</td><td>PETMP</td><td>PET4A</td><td>PVDF-HFP</td><td>NaSTFSI|PETMP|
PET4A|PVDF-HFP</td></tr>
<tr><td colspan="6">Baseline</td></tr>
<tr><td>NaSTFSI-SIPE</td><td>2</td><td>10</td><td>6</td><td>4.4</td><td>9|46|25|20|</td></tr>
<tr><td colspan="6">PET4A content</td></tr>
<tr><td>T1</td><td>2</td><td>10</td><td>4</td><td>4.4</td><td>10|49|19|22|</td></tr>
<tr><td>T2</td><td>2</td><td>10</td><td>5,5</td><td>4.4</td><td>9|46|25|20|</td></tr>
<tr><td>T3</td><td>2</td><td>10</td><td>7</td><td>4.4</td><td>9|42|30|19|</td></tr>
<tr><td>T4</td><td>2</td><td>10</td><td>8,5</td><td>4.4</td><td>8|40|34|18|</td></tr>
<tr><td>T5</td><td>2</td><td>10</td><td>10</td><td>4.4</td><td>8|38|37|17|</td></tr>
<tr><td colspan="6">PVDF-HFP content</td></tr>
<tr><td>P1</td><td>2</td><td>10</td><td>7</td><td>0</td><td>11|53|36|0|</td></tr>
<tr><td>P2</td><td>2</td><td>10</td><td>7</td><td>2.2</td><td>10|50|30|10|</td></tr>
<tr><td>P3</td><td>2</td><td>10</td><td>7</td><td>4.4</td><td>10|43|29|18|</td></tr>
<tr><td>P4</td><td>2</td><td>10</td><td>7</td><td>6.6</td><td>10|43|29|18|</td></tr>
<tr><td>P5</td><td>2</td><td>10</td><td>7</td><td>8.8</td><td>8|40|26|26|</td></tr>
<tr><td>P6</td><td>2</td><td>10</td><td>7</td><td>11</td><td>7|36|25|32|</td></tr>
<tr><td></td><td colspan="4">Molar ratio [mol]</td><td>Composition [mol%]</td></tr>
<tr><td>SIPE label</td><td>NaSTFSI</td><td>PETMP</td><td>PET4A</td><td>PVDF-HFP</td><td>NaSTFSI|PETMP|
PET4A|PVDF-HFP</td></tr>
<tr><td colspan="6">Monomer content</td></tr>
<tr><td>M1</td><td>1</td><td>10</td><td>7</td><td>4.4</td><td>4|48|29|19|</td></tr>
<tr><td>M2</td><td>2</td><td>10</td><td>7</td><td>4.4</td><td>9|44|28|19|</td></tr>
<tr><td>M3</td><td>3</td><td>10</td><td>7</td><td>4.4</td><td>13|43|26|18|</td></tr>
<tr><td>M4</td><td>4</td><td>10</td><td>7</td><td>4.4</td><td>17|40|25|18|</td></tr>
<tr><td>M5</td><td>5</td><td>10</td><td>7</td><td>4.4</td><td>20|38|25|17|</td></tr>
<tr><td>M6</td><td>6</td><td>10</td><td>7</td><td>4.4</td><td>23|36|25|16|</td></tr>
</table>

Table 4.2: Membrane list of chapter 5.3 and 5.4

	Molar ratio [mol]				**Composition [mol%]**
SIPE label	SSM as indicated	PETMP	PET4A	PVDF-HFP	SSM|PETMP|PET4A|PVDF-HFP
Anionic center					
NaSTFSI	4	10	7	4.4	17|40|25|18|
NaVBS	4	10	7	4.4	17|40|25|18|
NaSDCM	4	10	7	4.4	17|40|25|18|
Spacer arm					
NaSTFSI	4	10	7	4.4	17|40|25|18|
NaMTFSI	4	10	7	4.4	17|40|25|18|
NaFTFSI	4	10	7	4.4	17|40|25|18|

Table 4.3: Membrane list of chapter 5.5 and 5.6

	Molar ratio [mol]				**Composition [mol%]**
Different backbone monomers					
	NaMTFSI	PETMP	Monomer as indicated	PVDF-HFP	NaSTFSI|PETMP|X|PVDF-HFP
Diene	4	10	14	4.4	12|31|43|14|
Trione	4	10	9	4.4	15|36|33|16|
PET4A	4	10	7	4.4	17|40|25|18|
PET6A	4	10	4.5	4.4	18|44|19|19|
NaMDCM					
	NaMDCM	PETMP	Diene	PVDF-HFP	NaMDCM|PETMP|Diene|PVDF-HFP
NaMDCM	4	10	7	4.4	12|31|43|14|

Chapter 4.4
Characterization Techniques

4.4.1 Nuclear Magnetic Resonance Spectroscopy

NMR is an important technique to determine the structure of organic molecules by utilizing the interaction of the magnetic field that is produced by the spin I of a nucleus with an external magnetic field. Every nucleus is moving and rotating thus has a spin larger than 0. This spin creates a magnetic moment μ that is proportional to its spin over the gyromagnetic ratio γ using the formula:

$$\mu = \gamma \, I$$

The obtained magnetic moment μ reacts with other magnetic fields thus a strong and homogeneous external magnetic field B_0 can be applied to force an orientation on the spins, thus creating different energy levels. The amount of different energy levels is defined as 2 I +1, where I equals $\frac{1}{2}$ for the ^{1}H nucleus in the standard NMR experiment, thus two different energy levels are obtained (Figure 4.9).[111–114]

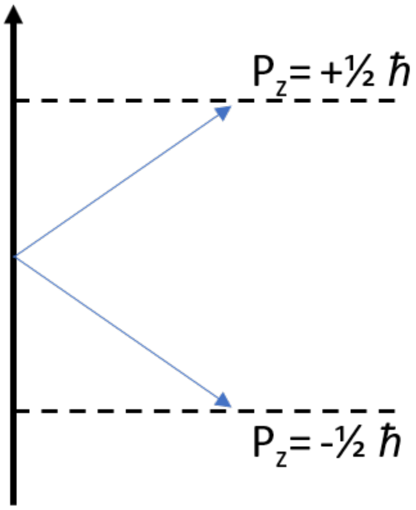

Figure 4.9: Direction depending separation of the magnetic moment μ into two different energy levels.

The difference between these energy levels can be expressed as ΔE and depends on the aforementioned gyromagnetic ratio γ, the magnetic field B_0 and the reduced Planck constant. Spins in the lower energy level can be stimulated to the higher energy level by using a fitting resonance frequency (MHz area). The exact frequency that is required to match the energy difference depends not only on the nucleus itself but also on the electron structure around it, as electrons also create a weak magnetic field that influences the magnetic moment of the nucleus. The NMR spectroscopy utilizes the resulting shift to create separate peaks that can be matched to different chemical shifts of the different nuclei of the molecule. Additional to the chemical shift, the ratio of the integrals of all peaks, the splitting pattern (singlet, doublet, etc) and the coupling constant can be used to determine/confirm the chemical structure. NMR spectra could be obtained by simply changing the frequency in small steps and observing the current applied to the electromagnetic field, however, this procedure is rather time consuming thus Fourier-transformed NMR spectroscopy is used instead. FT-NMR allows to simultaneously stimulate a wide range of resonance frequencies with an electromagnetic pulse and observing the relaxation of the spins back to equilibrium. Two main relaxation processes can be observed, the spin-lattice and the spin-spin relaxation, which match the longitudinal and transversal relaxation time, respectively. The «free induction decay» is measured by a current induced to a detector coil, which can be Fourier transformed to result in a regular NMR spectrum with spin specific shifts. The shifts are often normalized against a reference substance (Like DMSO-d6) in order to be comparable independent of the field strength.[111–114]

1,3-Dichloropropane for example (Figure 4.10) shows two peaks that refer to the C-CH_2-C and -CH_2Cl protons. The peaks are labeled as proton peak A and B, respectively. Proton peak B is shifted to higher ppm compared to proton peak A, due to the close proximity to the electron-drawing Cl group. The integral of both peaks confirms the peak B belongs to the two -CH_2Cl groups with 4 protons and peak A to the C-CH_2-C group with 2 protons. The peak of proton B is a triplet, since it has two neighboring protons, while the peak of proton A is a quintet, since the four protons of the -CH_2Cl group are in close proximity. The coupling constant of 6.2 Hz can be used to confirm that the interacting protons are sitting on neighboring CH atoms.[115]

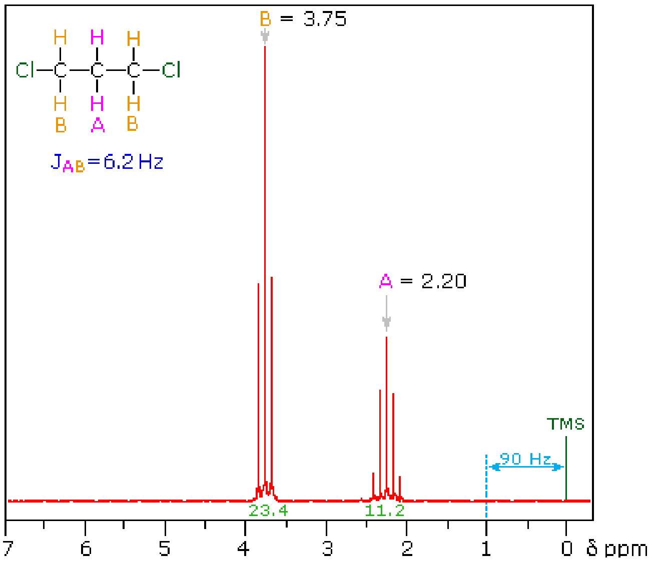

Figure 4.10: Example NMR graph of 1,3-dichloropropane. Reprinted from ref.[115]

The NMR of not dissolvable solids is not possible for liquid NMR spectroscopy, thus cross-polarization magic angle spinning NMR (CPMAS-NMR) has to be used for further insight. CPMAS-NMR combines cross-polarization, high-speed sample rotation and pulsed NMR to obtain high quality data. The proton-carbon cross polarization ($^1H \rightarrow ^{13}C$) allows for a high sensitivity of carbon atoms that would otherwise not give sufficient data by transferring magnetization from abundant nuclei with high γ (like ^1H), to low γ nuclei (like ^{13}C) via dipolar coupling. The magic angle spinning at 54.74° also improves the resolution by averaging out anisotropic interactions.[116,117]

4.4.2 Fourier-Transform Infrared Spectroscopy

Infrared (IR) spectroscopy allows to get a deeper understanding of the chemical structure of a molecule by using an interferometer. An interferometer (Figure 4.11a) consists of an infrared light source (s) that emits light on a beam splitter. This beam splitter (dashed line) allows roughly half of the light to pass through while reflecting the other half. The reflected part of the beam hits mirror M_1 after traveling a distance L, where it is reflected and hits the splitter again after traveling a total distance of 2L. The second part of the beam that travels through the splitter travels towards mirror M_2 where it is also reflected and travels back to the splitter, however, the distance between the second mirror and the splitter can be varied by the distance x. The exact distance x is practically determined by a He-Ne laser that controls the change in optical path difference. The difference in path lengths results in spatially coherent interference between both beams once they recombine. The recombined beam then passes through the sample and is collected on detector D as a distance x depending intensity function I(x) called the interferogram. The constructive interference of the partial waves yields a maximum detector signal if the optical retardation equals a multiple of the wavelength lambda ($2x=n*\lambda$ for ($n=0,1,2,...$)), while a minimum detector signal is obtained when the waves have a destructive interference (2x is not a multiple of $\lambda/2$). The conventional IR spectra would measure the intensity as a function of the wave number v which is equal to $1/\lambda$, however, FTIR allows to detect all frequencies that are emitted by the IR source at the same time and decoupling them using Fourier transformation, thus only requiring as much time as the mirror needs to move the desired distance.[118]

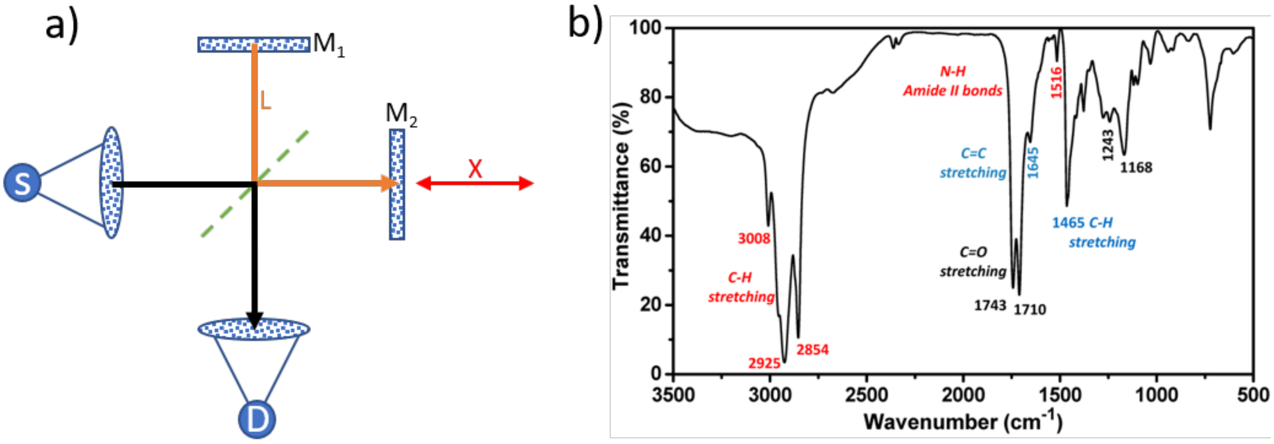

Figure 4.11: a) Sketch of an interferometer used for FT-IR spectroscopy. b) Example spectrum of a lipopeptide with marked absorbant' bands.[119]

The measured intensity of the signals is characteristic for certain bonds, such as C-C stretching around 3000 cm^{-1} or C=O stretching at ~1700 cm^{-1}. An example FT-IR spectrum of a lipopeptide is shown in figure 4.11b.

4.4.3 Thermogravimetric Analysis

Thermogravimetric analysis (TGA) allows to get insights of the thermal stability of a sample by measuring the change of mass of the sample during a set temperature program. Usually, a constant heating rate is used to determine any physical or chemical changes of the material upon heating to verify temperature depending structural changes. The setup is simply a high-precision balance that measures the samples weight while the sample is inside an oven. The resulting mass-vs-temperature curve can be used to identify the stable temperature range of the sample as well as the onset, velocity and remaining mass of the decomposition products. A constant flow of gas can be used to transport any decomposition products into a connected mass spectrometer (MS) to measure the masses of the decomposition products, thus allowing further insight about the decomposition reactions.[120,121]

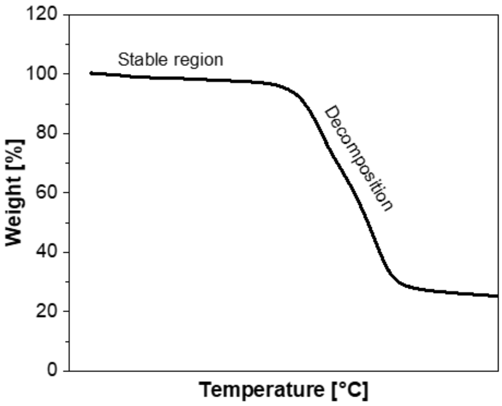

Figure 4.12: A schematic TGA curve. No mass loss is detected in the stable region, while decomposition is visible as a mass loss with increasing temperature.

4.4.4 Differential Scanning Calorimetry

A DSC measurement is used to get insight into the structural properties of a sample by measuring the heat flow of a sample during a controlled temperature program (heating and cooling cycles) and comparing this heat flow to a reference. The samples are prepared in a small sealed metal pan that is put together with an empty reference pan into a furnace. Both pans are heated at a linear rate, while a sensor measures the heat flow. Subtracting the heat flow of the reference pan from the tested sample allows to detect the heat transport effects that occur in the sample. The heat flow is plotted against the temperature to obtain a DSC thermogram that shows thermally induced transitions such as heat release upon crystallization, heat absorbance upon melting or decomposition or changes in the morphology such as a glass transition. A typical DSC curve is shown in figure 4.13.[121,122]

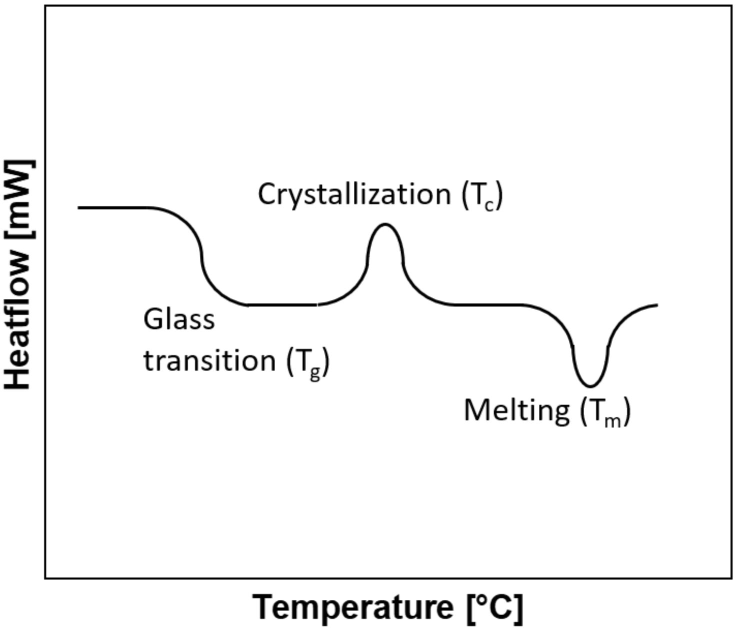

Figure 4.13: A typical DSC curve. Reprinted from ref.[122]

4.4.5 Chronopotentiometry

Chronopotentiometry represents the most common cycling technique and is used to study the variation of the potential of a working electrode with time upon imposition of a controlled current, while the current can be reversed to obtain the reversed reaction. The obtained voltage response is recorded and analyzed as a function of time, resulting in a stripping and plating graph (Figure 4.14) where the maximum obtained voltage per applied current density is referred to as the overpotential. The value of the overpotential as well as the shape of the potential vs time curve can be used to analyze the electrochemical properties of the system.[123,124]

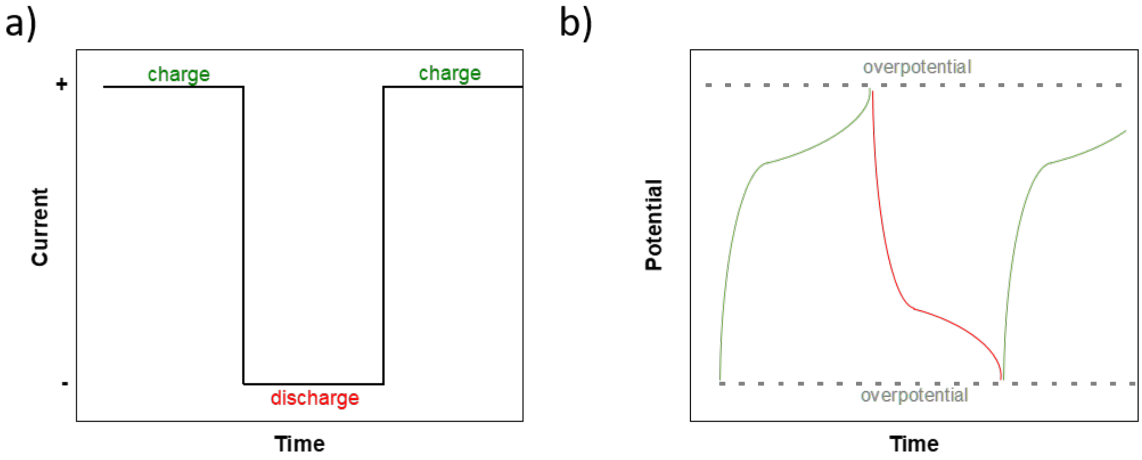

Figure 4.14: Schematic illustration of a) the applied current and b) the resulting potential response upon cycling.

4.4.6 Linear Sweep Voltammetry

Linear sweep voltammetry is used to assess the anodic and cathodic electrochemical stability of the material by increasing (anodic/oxidative stability) or decreasing (cathodic/reductive stability) the potential until decomposition reactions occur. The current is recorded as a function of the applied potential to pinpoint the start of the decomposition reaction. The voltage range between the cut-off potentials of the anodic and cathodic scan together represents the electrochemical stability window (ESW, Figure 4.15) that determines the range in which no unwanted side reactions or decomposition reactions occur. The cathodic cut-off potential is 0 V vs Na^+/Na if no prior reactions are observed, as Na^+ will plate as sodium-metal below 0V vs Na^+/Na.[125,126]

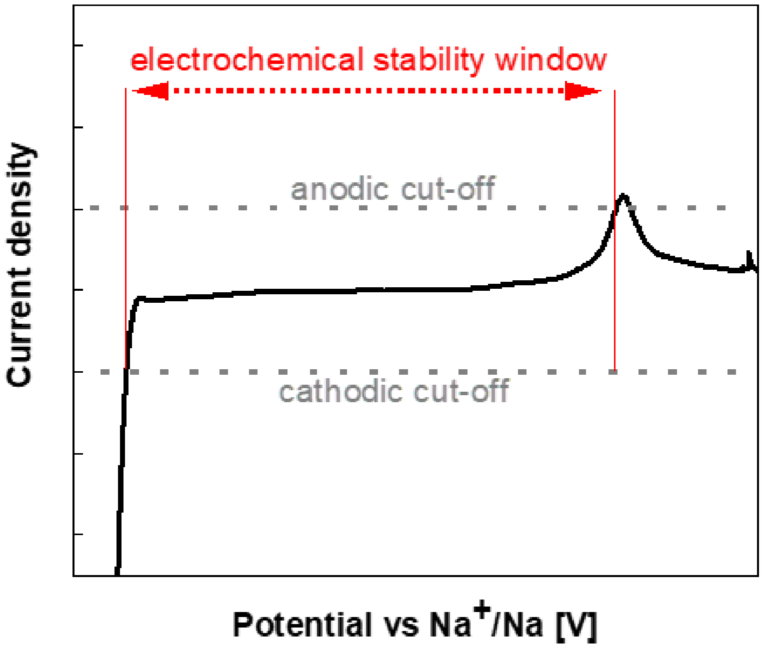

Figure 4.15: Schematic illustration of an anodic and cathodic LSV scan to determine the ESW.

4.4.7 Galvanostatic Cycling

Galvanostatic cycling summarizes a technique where a defined current is applied and the potential of the system is recorded. The current is reversed after the cell reaches a specific potential (upper and lower cut-off potential). The resulting data can be plotted to either analyze the voltage profile (Figure 4.16a) by plotting voltage vs capacity to assess the charge and discharge behavior or the cycling performance (Figure 4.16b) by plotting capacity per cycle to determine the capacity retention.[127]

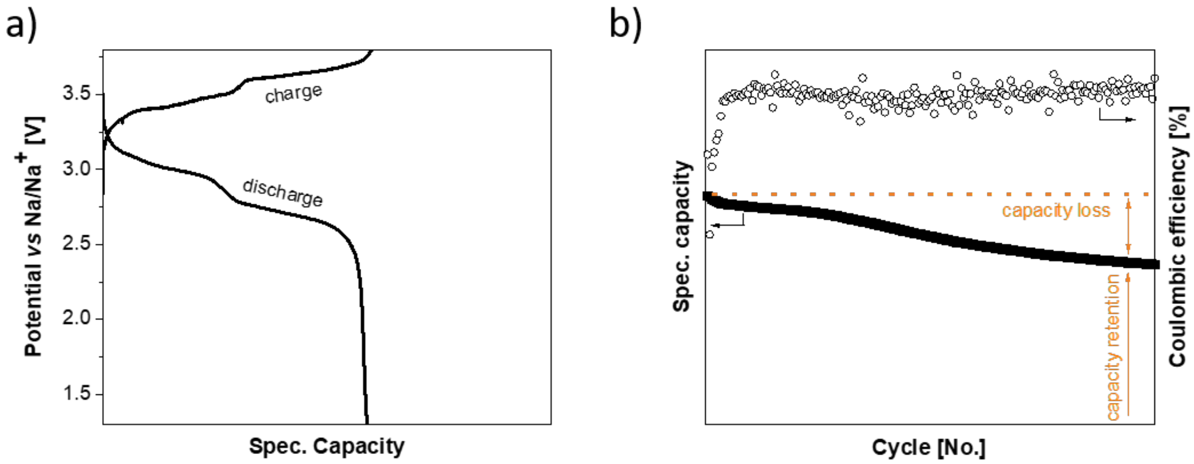

Figure 4.16: a) Schematic voltage profile and b) cycling performance.

4.4.8 Mechanical Properties

The mechanical properties of polymer membranes are important for their potential application. The mechanical stability can be measured by elongating the polymer until failure and recording a stress-strain curve (Figure 4.17). The first region marks the elastic region, where the deformation is rather small, and a linear ratio between stress and strain can be observed. The next region defines the yield stress, followed by the materials hardening. The last region marks the area where the material begins to becomes more and more unstable, until it breaks.

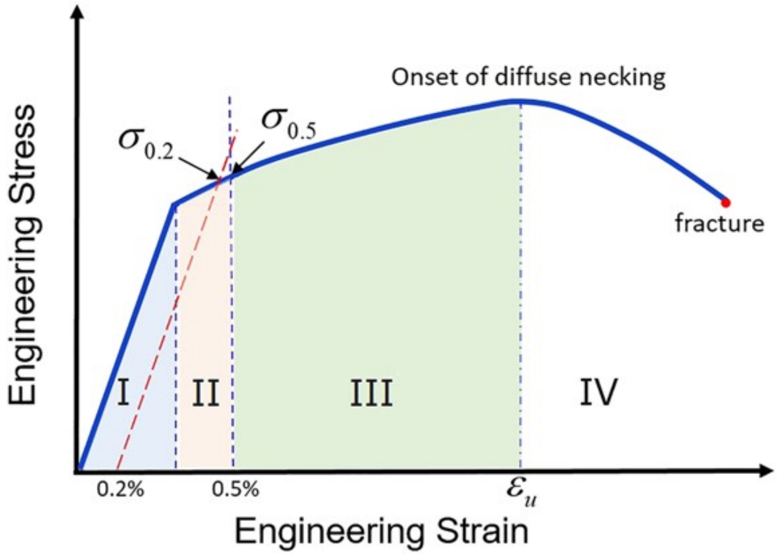

Figure 4.17: Schematic stress-strain curve via uniaxial tensile test. Reprinted from ref.[128]

4.4.9 Electrochemical Impedance Spectroscopy

EIS is a technique to investigate the electron transfer properties of electrodes, electrolytes and interfaces, among others. The reactions at the electrode-electrolyte interface for example involve a series of multi-step processes such as mass transport in the electrolyte, ion desolvation and charge-transfer at the interface, each happening at their own rates. EIS allows to separate and analyze these time-dependent mechanism by measuring the response (current or potential) of the system at different frequencies. EIS is commonly used to analyze time-invariant systems, thus the system is kept in a stationary state during the measurement by applying a small potential to excite the system at different frequencies. The response of the system can be used to calculate the electrochemical impedance. The obtained data can be plotted in form of a Nyquist plot (Figure 4.18).[129]

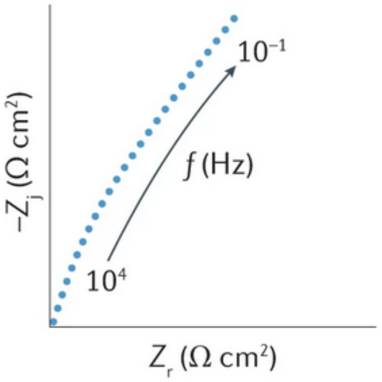

Figure 4.18: Nyquist plot of a typical EIS scan. Reprinted from ref.[129]

The ionic conductivity of the electrolyte (σ), for example, can be calculated using the formula $\sigma = d/RA$, where R is the obtained resistance from the impedance measurements (usually the X-axis at high frequency), and d and A are, respectively, the thickness and the area of the electrolyte.

4.4.10 X-Ray Photoelectron Spectroscopy

Surface chemistry of the samples before and after cycling was investigated by using a combination of X-ray photoelectron spectroscopy (XPS) and Time-of-Flight secondary ion mass spectrometry (ToF-SIMS). XPS allows to identify and quantify elemental compositions of the surface of any solid surface, revealing not only which elements are present but also which chemical environment they have. XPS uses photons of a specific frequency range to stimulate electrons of the inner orbitals of an atom, which are then transported to the surface of the sample and emitted into a vacuum before being detected. The kinetic energy of the detected photoelectron is specifically characteristic to the atom and orbital it originates from thus the chemical analysis of the surface can be conducted.[130] The measured kinetic energy $\mathrm{E_{kin}}$ depends on the energy of the photon (hν), the binding energy of the electron ($\mathrm{E_{binding}}$) and the work function of the spectrometer (ϕ_s) and can be expressed using the formula:

$$E_{kin} = h\nu - E_{binding} - \phi_s$$

The observed binding energy is specific for the elemental composition, chemical states, and electronic structure. A sample S2p XPS graph is displayed in figure 4.19. The raw data are fit using two components as indicated. The intensity of both peaks can be set into relation to

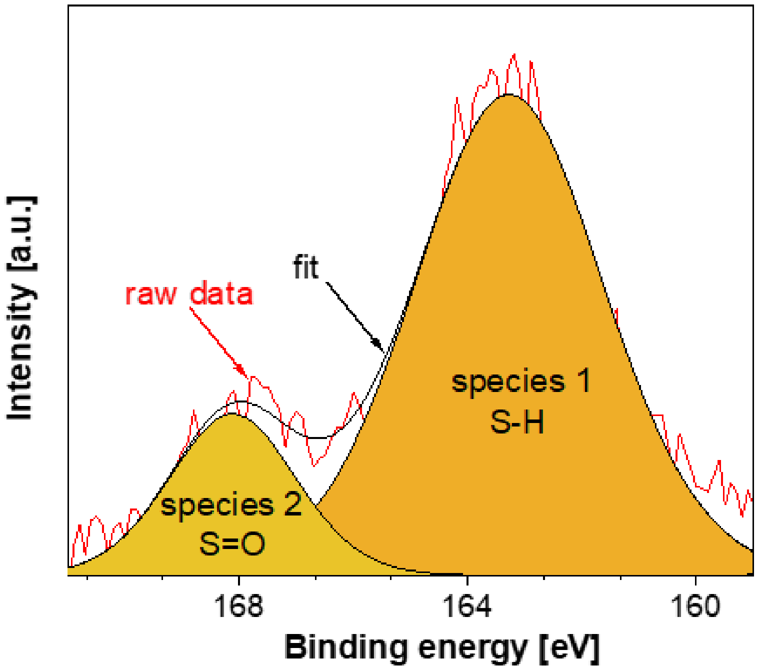

Figure 4.19: Sample XPS spectrum of surface species with binding energy peaks corresponding to specific elemental composition and chemical state.

4.4.11 Small- and Wide-Angle X-ray Scattering

X-ray Scattering uses the interactions of X-ray kα radiation of a wavelength of 0.01 to 0.2 nm with the sample and detecting the amount and direction of the scattered beam, which depends on the refractive index, the scattering length and the electron density (Figure 4.20). Keeping the first two constant, the obtained scattering patterns can be transformed into a function of q, where q inversely depends on the average distance L between consecutive crystalline lamellae ($L=2\pi/q_{max}$), also called long-period, in the sample.[131] The q-depending signals of the small- and wide angle X-ray scattering (SWAXS, Figure 4.20) can be analyzed to reveal structural properties of the sample.

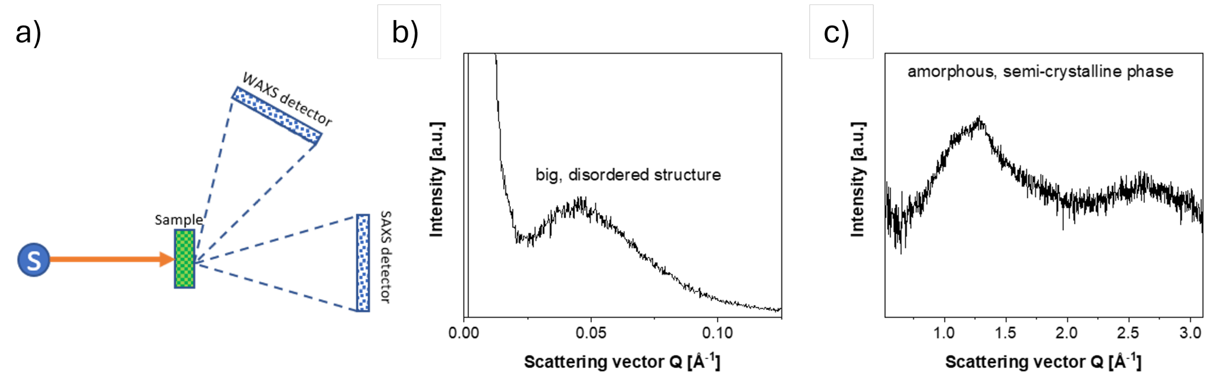

Figure 4.20: a) Schematic diagram of a SWAXS setup. b) Small- and c) wide-angle X-ray scattering of the diene-SIPE.

The shape and shift of the detected peaks can be used to analyze the size, shape, and organization of nanoparticles, micelles, polymer chains, or porous materials. The SAXS spectra (Figure 4.20a) of the diene-SIPE shows a peak at low q-values, indicating a bigger structure, while the broad peak indicates a disordered system. The peak at high q-values (Figure 4.20b) indicates a crystalline or semi-crystalline phase. This peak is also broad, suggesting again a disordered or amorphous orientation.

Chapter 4.5
Instrumental Procedures

The electrochemical properties of the SIPEs were investigated in four different coin cell (S4R, CR2032) configurations employing: i) two Al current collectors for ionic conductivity tests, ii) two Na metal discs (∅12 mm, Merck) for stripping/plating tests and interfacial resistance analysis; iii) one Al current collector and a Na metal disc for linear sweep voltammetry (LSV), and iv) one PW electrode (Altris) and a Na metal disc as positive and negative electrodes, respectively, for galvanostatic tests. The coin cells were sealed using a hydraulic coin cell crimping machine (CR2032, S4R, pressure of $\sim$ 800 psi). All electrochemical tests were performed at 40 °C since EC is at risk of crystallization below this temperature.

4.5.1 Nuclear Magnetic Resonance Spectroscopy

The ^{1}H, ^{13}C and ^{19}F NMR spectra in this thesis were recorded using a Bruker Avance 400 NMR spectrometer with DMSO-d6 as solvent. ^{1}H$\rightarrow$^{13}C CPMAS-NMR experiments of NaSTFSI and NaSTFSI-SIPE were performed similarly to a previous report[74] on a Bruker Avance III HD 600 NMR spectrometer with a 14.1 T magnet operating at a frequency of 600.12 MHz for ^{1}H and 150.92 MHz for ^{13}C. A 3.2 mm rotor was used to spin the samples at 10 kHz. For the ^{1}H$\rightarrow$^{13}C CPMAS spectra, a $\pi/2$ excitation pulse on ^{1}H was applied with a duration of 2.3 μs. A linear ramp (50-100) was used on the ^{1}H channel during cross-polarization transfer with a contact time of 2 ms. 512 scans were collected employing a repetition delay of 4 s, corresponding to 35 min of measurement time for each spectrum. For heteronuclear ^{1}H decoupling, the ppm 15 sequence was applied during acquisition.[75] ^{13}C CPMAS NMR chemical shifts were referenced with respect to tetramethylsilane (TMS = 0 ppm) using glycine as an external standard (C=O signal at 176.5 ppm). The signal assignment was based on the ^{13}C NMR chemical shifts predicted from the chemical structure of NaSTFSI using the ACD Lab/NMR software.

4.5.2 Fourier-Transform Infrared Spectroscopy

Fourier transform infrared spectroscopy (FT-IR) was performed on an FT-IR spectrometer (PerkinElmer Spectrum Two) between 400 and 4000 cm^{-1} to study the characteristic bonds in the synthesized monomers and membranes.

4.5.3 Thermogravimetric Analysis

TGA (coupled with mass spectroscopy (MS) for the NaSTFSI-SIPE) were carried out on a Netzsch TG 209 F1 with a heating rate of 5 K min^{-1} using He as protective gas. The membranes were sealed in Al crucibles and were measured between 30 and 600 °C using a sample mass of $\sim$ 5 mg, while a N_2 flow was used to collect and then measure the produced fractions during heating. Each TGA experiment was carried out at least two times to confirm reproducibility.

4.5.4 Differential Scanning Calorimetry

Differential scanning calorimetry was performed on a DSC Discovery series from T.A. Instruments using $\sim$ 10 mg of sample in sealed Al pans in three sweeps between -20 and 200 °C using a heating rate of 5 K min^{-1} under N_2 (gas flow: 10 mL min^{-1}). The analysis was performed using the TRIOS software provided by TA Instruments. Every DSC experiment was carried out at least two times to confirm reproducibility.

4.5.5 Chronopotentiometry

A Biologic SAS VMP-3e was used to measure the stripping/plating behavior, the anodic/cathodic stability, and the interfacial resistance at 40 °C, storing the cells in a Binder climatic chamber KB23. In the stripping/plating tests, the current density was varied between 10 and 50 μA cm^{-2}, starting with 10 μA cm^{-2}. The current at each step was reversed every 30 min until 5 cycles completed, at which point the current was increased by 10 μA cm^{-2}. Additional EIS tests were conducted after the 1st and 5th cycle at each current density and after prolonged cycling for 25 cycles at 50 μA cm^{-2}, using the Biologic SAS VMP-3 (frequency range: 1 kHz to 1 MHz, amplitude: 10 mV).

4.5.6 Linear Sweep Voltammetry

The cells that were used for linear sweep voltammetry were rested for 6 h and later tested at a scan rate of 30 μV s^{-1} up to 7 V or down to -2 V, respectively.

4.5.7 Galvanostatic Cycling

The galvanostatic tests of Na||PW cells were carried out at 40 °C (Binder climatic chamber KB 115) by using a Maccor 4000 battery testing system to apply a current of C/50 for the initial cycle followed by 5 cycles of C/20 and ongoing cycles of C/10 until failure (1C = 150 mAh g^{-1}). The cathode consisted of 80% PW ($Na_2Fe[FE(CN)_6]$, Altris), 10% carbon additive (Super P45), 5% carboxymethyl cellulose (CMC), and 5% styrene-butadiene rubber (SBR, Zeon) with a mass loading of 1.3 ± 0.4 mg cm^{-2}. The PW electrodes were dried at 70 °C at 10^{-7} bar for 24 hours and stored in a glovebox ($O_2 < 0.1$ ppm, $H_2O < 0.1$ ppm).

4.5.8 Mechanical Properties

The solvent-casted polymer membranes were cut into dumbbell specimen using the cutting press ZwickRoell ZCP 020. The thickness of the membranes was around $100\,\mu m \pm 10\,\mu m$. The tensile tests were performed on a universal testing machine Inspect Table from Hegewald and Peschke (Nossen, Germany), equipped with a 1.5 kN force transducer. The tests were performed at room temperature with a testing speed of 5 mm min^{-1}.

4.5.9 Electrochemical Impedance Spectroscopy

Electrochemical impedance spectroscopy (EIS) measurements were carried out with the Solartron SI 1260/ 1287 Impedance Analyzer or the Biologic SAS VMP-3 (frequency range: 1 kHz to 1 MHz, amplitude: 10 mV) in the temperature range between 10 and 90 °C for ionic conductivity determination. The temperature was controlled using a Binder climatic chamber (KB23). The cell rested for 3 h after reaching a new temperature prior to measurement. The thickness of the electrolyte was measured ex-situ using a Mitutoyo Absolute digital thickness gauge 547-401. The impedance response was analyzed using the RelaxIS 3 software with an R.P. fit.

4.5.10 X-Ray Photoelectron Spectroscopy

In this thesis, XPS analyses were measured on a PHI Versaprobe II spectrometer. Charging effects were controlled during analysis with a combination of a low-energy electron gun (negative charge) and a low-energy argon gun (positive charge). The X-ray source was an Al Kα monochromatic beam (1486.7 eV, 200 W, 12 kV), and the takeoff angle was set at 45°. Pass energy was set to 23.5 eV for high-resolution spectral acquisition, providing an energy resolution of ~0.6 eV. Data treatment was performed using the MultiPak software. Spectra were calibrated by using C 1s in C-C/C-H as a reference binding energy (at 284.8 eV).[132] ToF-SIMS measurements were carried out with a ToF.SIMS.5 spectrometer (IONTOF GmbH), equipped with a 30 kV Bi cluster primary-ion gun. High-resolution imaging analyses were performed in negative ion mode using Bi_3^+ (30 keV) as primary ion species for analysis with a primary ion current of ~ 0.1 pA. Cycle time was set at 100 μs. Analysis was carried out in delayed extraction mode. Surface areas of 50 × 50 μm^2 were rasterized in random mode with 512 × 512 pixels, 1 shot per frame per pixel, and 1 frame per patch. Measurements were stopped when the total count for total ions reached ~ 107 counts. During all measurements, charge compensation was applied with a low-energy electron flood gun. Evaluation of ToF-SIMS data was achieved with the software SurfaceLab 7.3.

4.5.11 Small- and Wide-Angle X-ray Scattering

SWAXS patterns were collected using a Xeuss 3.0c (Xenocs – Grenoble, France) equipped with an Eiger2 1M detector. The sample-to-detector distance was set to 1100 mm, obtaining an overall usable Q-range from 0.00014 to 0.247 $Å^{-1}$. A Cu Kα source was used with a beam size of 0.35x0.35 mm^2, obtaining a flux of ~10^7 photons per second. The samples were stuck to a perforated metal plate using standard Scotch Tape. The powders were simply stuck to the adhesive tape, completely covering the holes of the plate, while membranes were stuck in a way that only the membrane was covering the hole. The sample chamber of the instrument was kept under vacuum (p = 80 μbar) during the experiment. Each measurement was performed for 10 min, repeated 2 to 6 times and the average was taken to ensure a good signal-to-noise ratio. The collected 2D scattering patterns were integrated over the entire circumference to obtain the scattering curves as a function of q. The intensity was scaled to absolute units using the sample transmission and the calibration with a glassy carbon secondary standard. The plain scotch tape background was also collected and subtracted from the total scattering curve. Data treatment was performed with the Xsact software from Xenocs.

Results and Discussion

The findings in this thesis were presented on various conferences and were published as indicated.

Chapter 5.1

The initially designed SIPE was electrochemically and thermally characterized and tested in proof-of-concept sodium metal cells. In addition, the interfacial layer of the SIPE against sodium-metal was investigated. The results were published under:

Wunder et al. *Sodium 4-styrenesulfonyl (trifluoromethanesulfonyl) imide-based Single-ion Conducting Polymer Electrolyte incorporating Molecular Transporters for Quasi-Solid-State Sodium Batteries*, Journal of Materials Chemistry A, 12 (32) , 2024, p. 20935-20946.

Chapter 5.2 & 5.3

The component driven influence of the backbone components, supporting polymer, and sodium salt monomer as well as the influence of the charge delocalization on the anionic center was assessed and will be published under:

Wunder et al. *Understanding the Component-driven Influence on the Electrochemical Properties in Single-Ion Polymer Electrolytes for Sodium-based Batteries*, ACS Applied Polymer Materials, 7 (8), 2025, p. 4895–4907.

Chapter 5.4 & Chapter 5.5

The mobility of the spacer arm and the influence of the backbone on the electrochemical, mechanical and thermal performance were investigated:

Wunder et al. *Influence of the Backbone Chemistry and Side-Chain Spacer Flexibility in Sodium Single-Ion Conducting Polymer Electrolyte for Sodium-Batteries*, EES Batteries, 2026.

Chapter 5.1
NaSTFSI-SIPE Development

A novel SIPE was produced and studied based on a NaSTFSI SSM that is tethered to a PETMP/PET4A backbone and is supported by PVDF-HFP. The SIPEs ionic conductivity and SEI is further improved through the incorporation of EC:DMC:FEC as plasticizers. The structure of the SSM and the 3D-polymer network, the thermal and electrochemical properties and the cyclability in proof-of-concept Na||SIPE||PW cells were studied and analyzed.

5.1.1 NaSTFSI SSM and NaSTFSI-SIPE Characterization

A Na ion carrying monomer was synthesized to develop a new ionic conducting SIPE for SMBs. The mobility of the Na ion inversely depends on the binding strength toward the anion. This can be reduced by increasing the size of the anionic center since a delocalized negative charge results in a weak anionic strength towards the cation. Therefore, the designed SSM was based on the literature known bis(trifluoromethanesulfonyl)imide ($TFSI^-$) anionic center synthesized from NaVBS (Chapter 4.2.1). The structure of the in-house synthesized NaSTFSI SSM was verified using ^1H, ^{13}C, and ^{19}F NMR spectroscopy (Chapter 4.2.1, Figure 4.2).[110] The NaSTFSI-SIPE was manufactured by mixing the homemade NaSTFSI SSM with PETMP, PET4A, and PVDF-HFP, resulting in a cross-linked polymer membrane structure (Figure 5.1) .

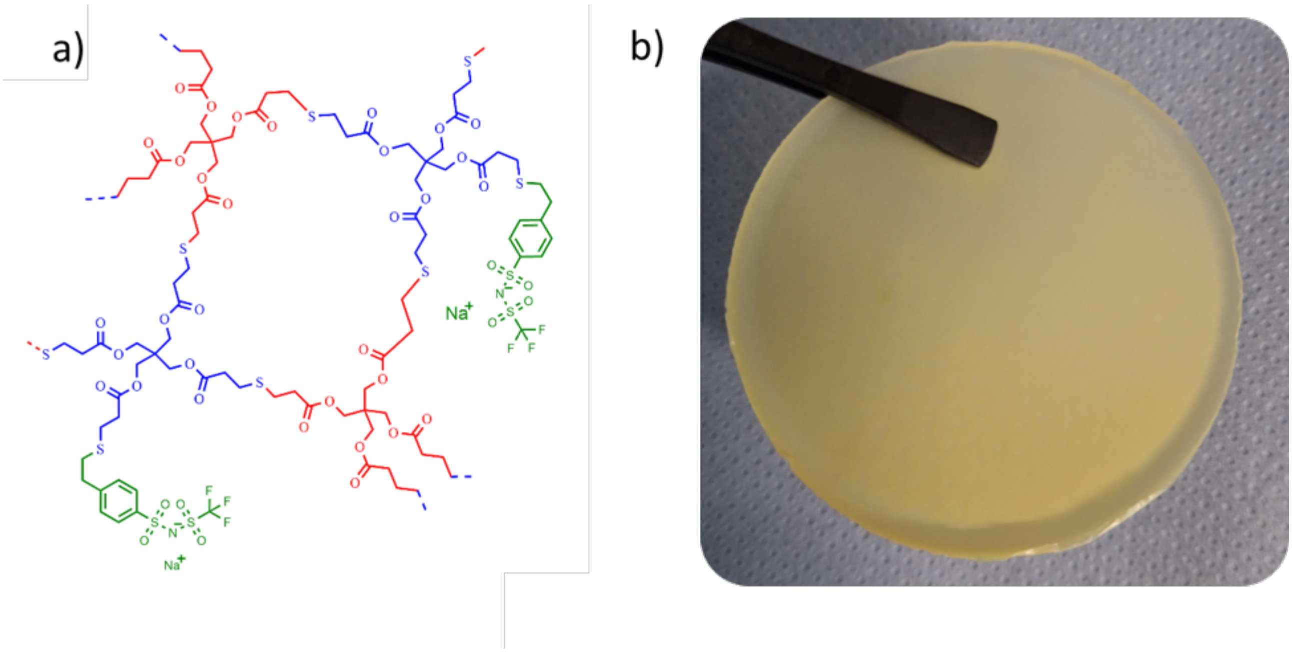

Figure 5.1: a) Cross-linked structure (NaSTFSI in green, PETMP in blue, and PET4A in red) and b) image of the self-standing NaSTFSI-SIPE.

The three-dimensional network structure of the NaSTFSI-SIPE could be confirmed through the creation of a new sulfur-carbon bond between PETMP and PET4A or NaSTFSI observed by combined FT-IR and NMR investigations as follows. Figure 5.2a illustrates the FT-IR spectra of the three monomers, i.e., NaSTFSI, PET4A, PETMP, and the NaSTFSI-SIPE. The NaSTFSI shows the characteristic stretching peaks of C-H around 3065 cm^{-1}, C=C at 1630 cm^{-1}, SO_2 at 1237 cm^{-1}, S=O at 1045 and 1008 cm^{-1}, and aromatic C-H at 676 cm^{-1}, and deformation vibration of N-SO_2 at 1182 and 1129 cm^{-1} and =C-H at 991, 906 and 843 cm^{-1}, confirming the successful synthesis of the NaSTFSI SSM, and in agreement with literature.[82,133] Meanwhile, the NaSTFSI-SIPE shows characteristic features of the three monomers, such as the stretching peaks of C-H (2960 cm^{-1}), C=O (1728 cm^{-1}), C-O-C (1130 cm^{-1}) and C-O (1015 cm^{-1}) groups, as well as the CH_2 (1411 and 1346 cm^{-1}), C-H (952 cm^{-1}) and =C-H (880 cm^{-1}) deformation vibrations. Noteworthy, the FT-IR spectrum of the membrane is similar to that of PETMP due to its highest weight fraction. Moreover, the FT-IR spectrum of the NaSTFSI-SIPE displays a new IR peak at 3400 cm^{-1}, corresponding to C-H bonds. However, the characteristic peak of the S-H group (2564 cm^{-1}) of PETMP vanished, suggesting the reaction of the S-H groups with free vinyl groups to form the new S-C bond, thus creating the proposed three-dimensional NaSTFSI-SIPE structure (Figure 5.1).[134,135]

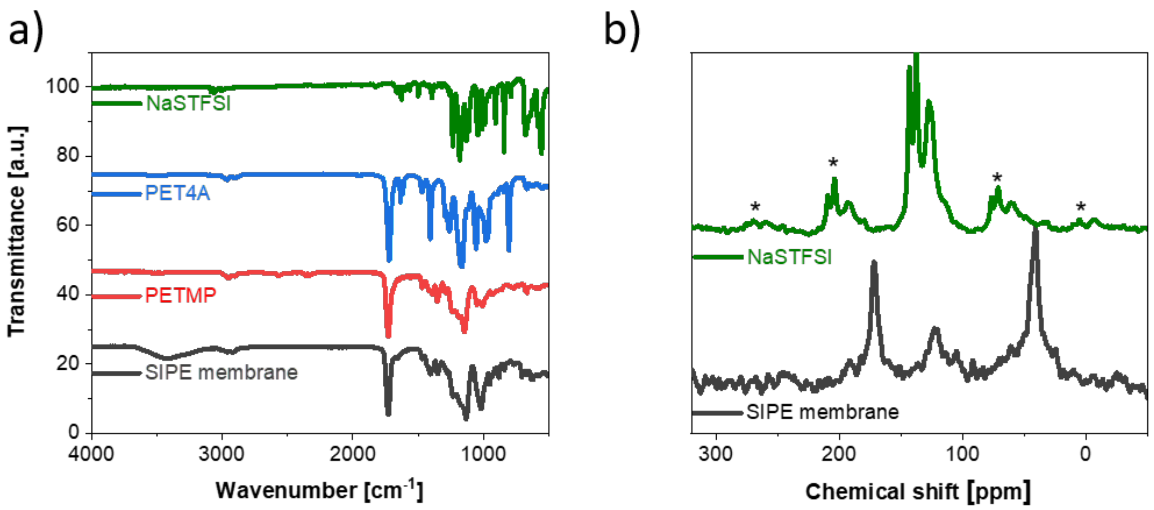

Figure 5.2: a) FT-IR spectra of NaSTFSI, PET4A, PETMP, and NaSTFSI-SIPE. $^1H \rightarrow ^{13}C$ CPMAS NMR spectrum of b) NaSTFSI and NaSTFSI-SIPE, recorded at 10 kHz. Note: Signals marked with asterisks (*) are spinning side-bands.

The $^1H \rightarrow ^{13}C$ CPMAS NMR spectrum of NaSTFSI (Figure 5.2b) exhibits overlapping resonances in the chemical shift range between 100 and 160 ppm, which contain spinning side-bands marked with asterisks. At least four different signals are distinguished, which overlay into a broad signal, probably referring to quaternary carbons in the aromatic ring. The signal at 115 ppm is attributed to the $-CH_2$ of the vinyl group. The signals at 128 and 138 ppm are originating from the carbons in the benzene ring. The signal at 143 ppm most probably refers to the -CH carbon of the vinyl group attached to the aromatic ring. Therefore, the $^1H \rightarrow ^{13}C$ CPMAS NMR confirms once more the successful synthesis of NaSTFSI. Significant changes are obtained by comparing the spectra of NaSTFSI and NaSTFSI-SIPE (Figure 5.2b). The NaSTFSI-SIPE shows signals at 41 and 171 ppm that do not refer to spinning side-bands. The asymmetric signal at 41 ppm is attributed to aliphatic species, whereas the narrow peak at 171 ppm is assigned to carbonyl groups (C=O) in the polymer network.[136] The line broadening makes it difficult to match the signals between 95 and 150 ppm to the different components. The resonances may originate from aromatic sp2 carbons,[136] as well as from fluorine-containing moieties such as CF_2/CF_3 groups, according to the literature.[137,138] To prove this hypothesis, additional ssNMR measurements, including 2D techniques, have to be performed, which are beyond the scope of the present work. Nevertheless, the obtained results agree well with the FT-IR, suggesting the three-dimensional structure of the NaSTFSI-SIPE.

5.1.2 Thermal Properties of NaSTFSI-SIPE

The thermal stability of the NaSTFSI-SIPE was investigated via TGA coupled with MS to identify the decomposition species. The NaSTFSI-SIPE is stable up to 280 °C (black curve, Figure 5.3a), which is comparable with other Na ion SIPEs.[104,107,139] The mass loss in the 130 and < 280 °C range is negligible, and the collected mass losses (colored curves in Figure 5.3a) indicate the release of N_2 ($m/z = 28$), O_2 ($m/z = 32$), O ($m/z = 16$), and N ($m/z = 14$) associated to air bubbles trapped inside the NaSTFSI-SIPE. At temperatures higher than 280 °C, a species with a mass of 19 is released, suggesting that fluorine is released upon membrane degradation.

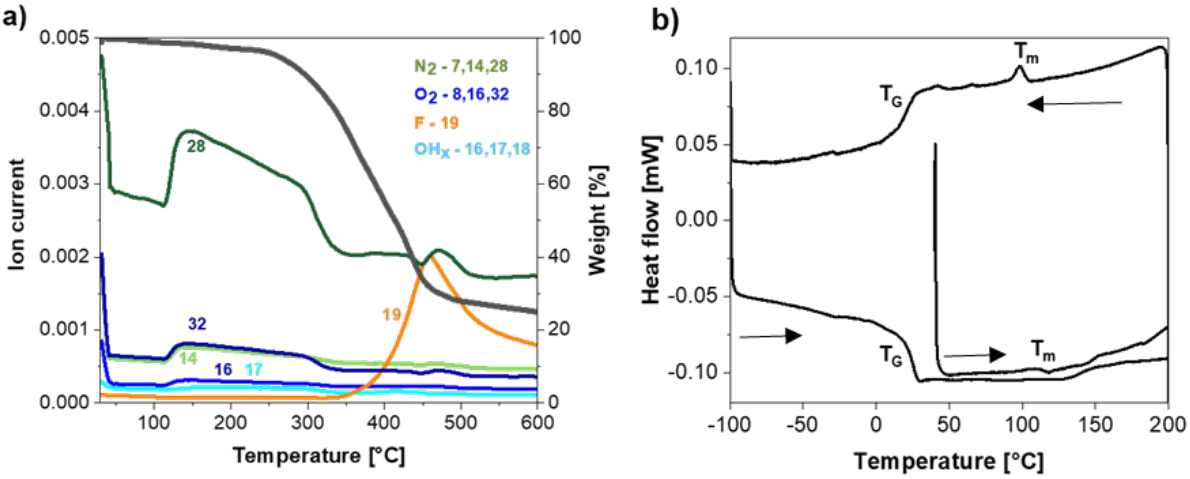

Figure 5.3: a) TGA/MS and b) DSC of the NaSTFSI-SIPE.

The DSC measurement confirms the high thermal stability of the membrane, showing a minimal heat flow (below 1 mW) when heating up to 200 °C, down to -100 °C, and then up to 200 °C again. The increase in the heat flow at 20 °C corresponds to the membrane's glass transition temperature (T_g), which is in the same range as for the Li-based SIPE analogue.[82] In addition, the NaSTFSI-SIPE exhibits a small peak (T_m) around 110 °C for the heating and cooling scan, related to the crystallization and melting temperature of the polymer membrane.[140,141]

5.1.3 Electrochemical Characterization of the NaSTFSI-SIPE

The electrochemical properties of the SIPE, consisting of NaSTFSI-SIPE (50 wt%) impregnated with 50 wt% of EC:DMC:FEC (49:49:2, vol%) as molecular transporter to favor the Na ion mobility, have been investigated through various techniques. The ionic conductivity was studied within the temperature range from 10 °C to 90 °C. The first measurement was performed at 40 °C and increased stepwise up to 90 °C. In the following cooling scan, the temperature was reduced stepwise down to 10 °C. The ionic conductivity (Figure 5.4) displays the Vogel-Tamman-Fulcher behavior, as commonly observed for Li and Na-based SIPEs.[82,142] This suggests that the Na ion transport is supported by the motion of the anionic center in addition to the support of the molecular transporters (EC:DMC:FEC) facilitating the jump of the Na ions between two anionic sites. The electrolyte exhibits an ionic conductivity of $1.4 \cdot 10^{-5}$ S cm^{-1} at RT (20 °C), which increases with increasing temperature due to higher chain flexibility and ion mobility. The ionic conductivity reaches $1.3 \cdot 10^{-4}$ S cm^{-1} at 90 °C, showing ionic conductivity comparable to that of other SIPEs blended with PVDF-HFP.[107,139,142] Additionally, the ionic conductivity values overlap those obtained in the first sweep, confirming the thermal reversibility of the NaSTFSI-SIPE. Finally, the activation energy of NaSTFSI-SIPE was calculated from the logarithm of the ionic conductivity against 1000/T (Figure S8.1). The NaSTFSI-SIPE exhibits a low activation energy of 0.13 eV, which results in a fluent Na ion transport as Na ions require only minimal energy to hop from one ionic center to the next.[143]

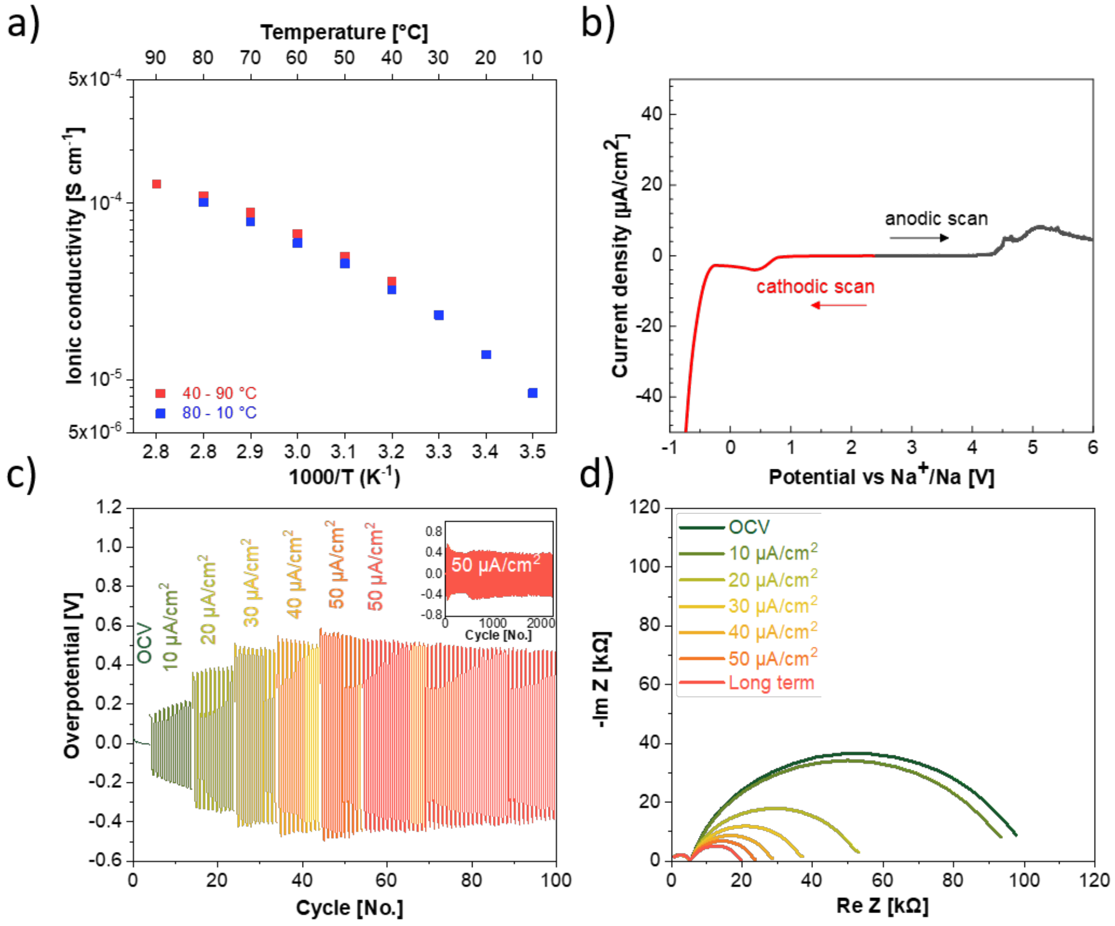

Figure 5.4: Electrochemical characterization of the NaSTFSI-SIPE: a) ionic conductivity in the temperature range of 10-90 °C, b) anodic and cathodic scan in Na||Al cells, c) Na stripping/plating test over 2000 h at different current densities in Na||Na symmetric cells, and d) the corresponding Nyquist plot after cycling for 10 cycles at each current density. Additionally, the EIS was measured after 100 cycles at 50 µA/cm^2 (red line). All tests were performed at 40 °C.

The electrochemical stability window of the NaSTFSI-SIPE was investigated by LSV (Figure 5.4b). The LSV measurements were carried out using two pristine cells to avoid cross-talking effects from the contamination of the decomposition products. Selecting the stability threshold at 5 µA cm^{-2} reveals a stability window up to 4.5 V vs. Na$^+$/Na while no limitation on the cathodic side prior to sodium-metal plating. This suggests that the designed NaSTFSI-SIPE could be used with the most common sodium-based cathode materials, such as layered oxides and Prussian Blue analogues (PBAs).

The compatibility with the sodium-metal electrode was further investigated by stripping and plating tests (Figure 5.4c) carried out at increasing current densities from 10 µA cm^{-2} to 50 µA cm^{-2}. Following, prolonged cycling at 50 µA cm^{-2} was performed to investigate also the long-term stability of the NaSTFSI-SIPE against sodium-metal. The tests show the expected increase of the overpotential with increasing current density. The observed overpotential of 0.15 V at 10 µA cm^{-2} increases to 0.35 V, 0.40 V, 0.41 V, and 0.42 V at 20, 30, 40, and 50 µA cm^{-2}, respectively. These values are comparable to those reported for other sodium-based SIPEs.[104] Additionally, the NaSTFSI-SIPE showed stable behavior at all investigated current densities. Finally, the electrolyte could be cycled at 50 µA cm^{-2} for over 2000 cycles with a rather stable overpotential. Noteworthy, in the initial cycles after the EIS test and current density increase, a variation in the overpotential is observed (see inset Figure 5.4c) due to a re-formation of the SEI, which needs to be readapted. Nevertheless, after a few initial cycles, the overpotential stabilized, showing promising compatibility properties with sodium-metal for developing long-cycling quasi-solid-state SMBs.

The interface established by the NaSTFSI-SIPE and the sodium-metal electrode was also investigated via EIS experiments. The Nyquist plots (Figure 5.4d) show the impedance spectra collected after the application of the different current densities and upon prolonged cycling. The ionic conductivity (first semicircle) does not change upon cycling; however, the second semicircle (charge transfer resistance at the sodium-metal/electrolyte interface) is reduced upon cycling. The NaSTFSI-SIPE shows an initial (OCV) interface resistance of around 100 kΩ. After applying a current density of 10 µA cm^{-2}, the resistance slightly decreases, exhibiting about 95 kΩ. This reduction might be related to the SEI formation, which behaves as a “buffer” interlayer, facilitating the Na ion transport across the solid-solid interface (further investigation in the section below). Indeed, the obtained impedance response and the size of the second semicircle are further reduced when cycling with 20 µA cm^{-2} for 10 cycles afterwards, suggesting the formation of a stable and probably homogeneous SEI, in agreement with the observed in the Na||Na symmetric stripping/plating test. The overall impedance and the size of the second semicircle are further reduced at each higher current density. This suggests that the formed SEI is growing and homogenizes with increasing current density to support the faster Na ion diffusion and provide good compatibility between the NaSTFSI-SIPE and sodium-metal and that the ion transport in the SIPE is stable even at higher current densities. In addition, the stability of the formed SEI is further confirmed by measuring the impedance after cycling for an additional 100 cycles at 50 µA cm^{-2}, showing an even lower interface resistance of 20 kΩ (red line).

5.1.4 Study of the Solid Electrolyte Interphase

EIS data reveals the formation of a stable SEI upon cycling. Hence, Na||Na symmetric cells after 5 cycles at 10 µA cm^{-2} were disassembled, and ex-situ XPS analysis was performed on the surface of the NaSTFSI-SIPE to identify the SEI chemistry. For the sake of comparison, XPS analysis was also performed on the dry NaSTFSI-SIPE and the pristine NaSTFSI-SIPE (soaked). Figure 5.5 illustrates the high-resolution C 1s, S 2p, and F 1s photoelectron spectra. In the C 1s spectra, five species are identified in the three investigated NaSTFSI-SIPEs, which correspond to hydrocarbons (C-C, 284.8 eV), carbon-oxygen species (C–O$_x$, ∼286 eV and ∼287 eV), carbonates (CO$_3$, ∼289 eV) and carbon-fluor compounds (CF$_x$, ∼290.5 eV),[132,144,145] in agreement with the O 1s region (Figure 5.6). The main component of the dry NaSTFSI-SIPE corresponds to the hydrocarbon groups in the PETMP and PET4A blocks.

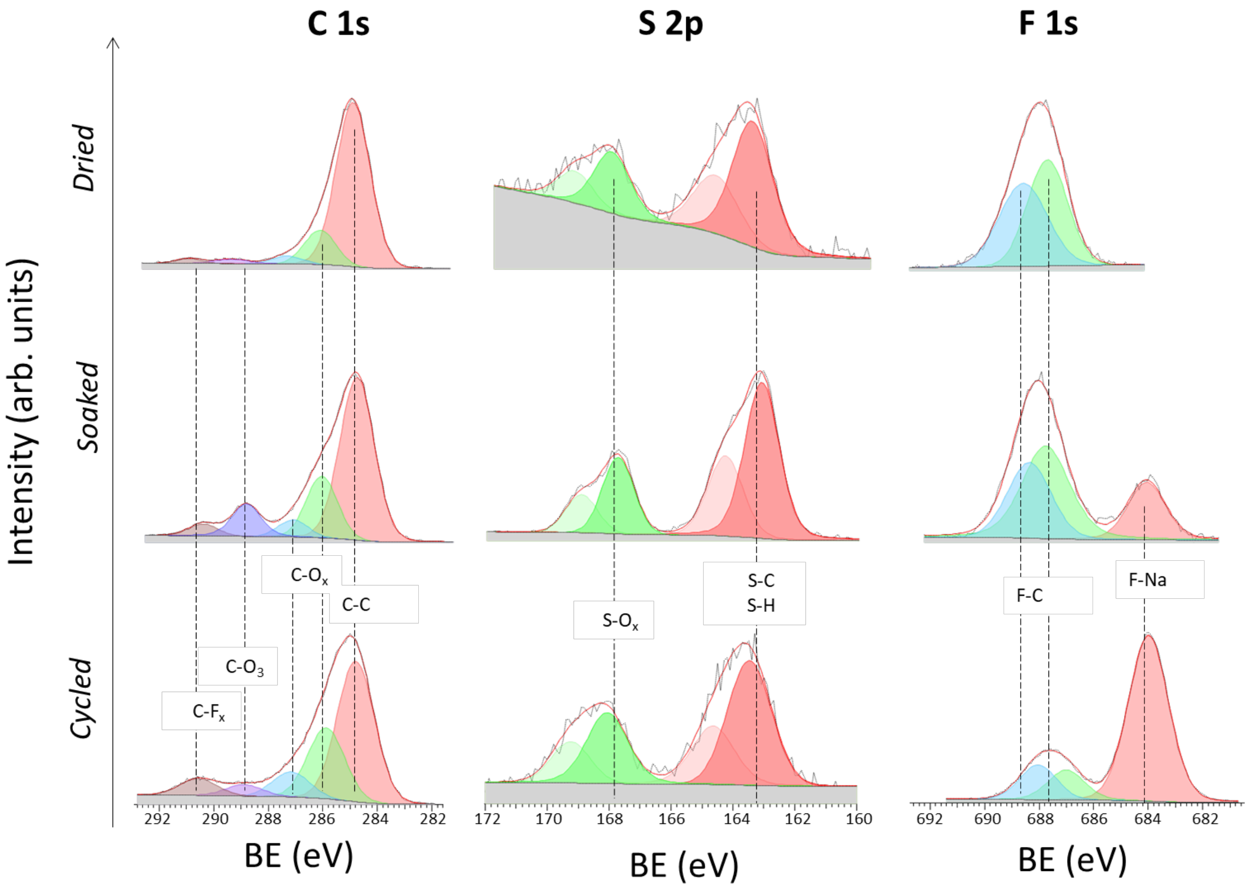

Figure 5.5: Ex-situ C 1s, S 2p, and F 1s XPS spectra of the surface of the NaSTFSI-SIPE (dried), incorporating EC:DMC:FEC molecular transporters (soaked) and after cycling for 5 cycles in a Na||Na symmetric cell under 10 µA cm^{-2} (cycled).

The addition of EC:DMC:FEC to the membrane (soaked) results in an increase in the intensity of carbonates (CO_3) and CF_x species. The concentration of the carbon-oxygen species further increases after cycling, indicating the reduction of the molecular transporters, e.g., EC, DMC, and FEC.[146] The S 2p spectra display two main components, i.e., S-C/S-H (∼163 eV) and S-Ox (∼168 eV) species, associated with the two monomers (NaSTFSI and PET4A).[145,147,148] The absence of other contributions suggests the stability of NaSTFSI and PET4A upon cycling. However, the F 1s spectra indicate the degradation of fluorine-containing components upon incorporation of the molecular transporters in the NaSTFSI-SIPE. Considering that the S 2p spectra confirm the stability of sulfur species, it can be reasonably assumed that NaF formed as a result of FEC decomposition (poor thermal stability) and/or PVDF-HFP dehydrofluorination.[149,150] Upon cycling further, NaF formed from the decomposition of FEC as well as other fluorinated species, becoming the main fluorine-containing component of the SEI (Figure 5.6).[151]

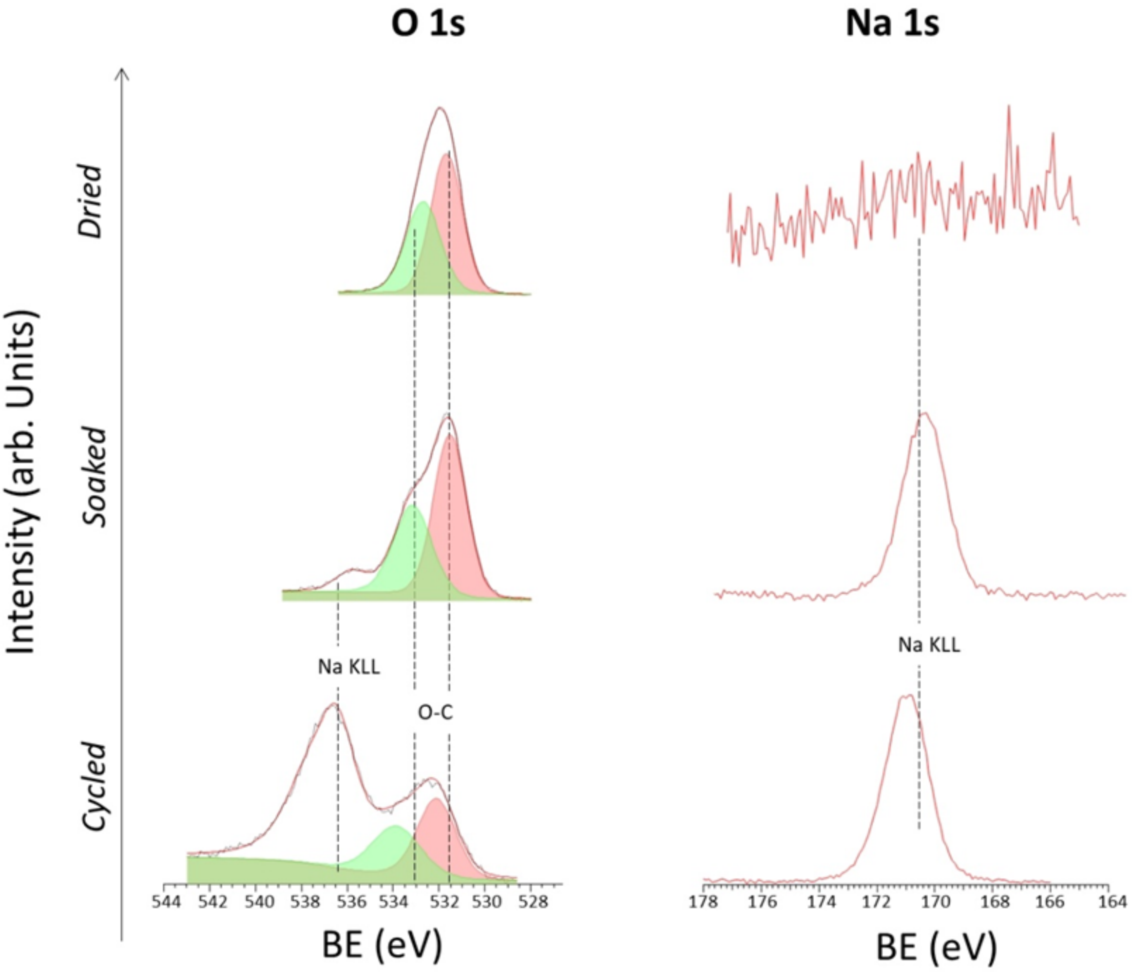

Figure 5.6: Ex-situ XPS spectra of O 1s and Na 1s of NaSTFSI-SIPE surface after cycling for 5 cycles in a Na||Na symmetric cell under 10 µA cm^{-2}.

Its distribution along the SEI was further investigated by ToF-SIMS imaging, which was conducted across various surface areas of each sample. Figure 5.7 (dried) shows the clear distribution of the NaSTFSI SSM (red) and PVDF-HFP (green) along the dry NaSTFSI-SIPE. Once the EC:DMC:FEC molecular transporters are incorporated in the NaSTFSI-SIPE (Figure 5.7, soaked), the surface is mainly covered by the fluorine species, mainly from FEC. After cycling (Figure 5.7, cycled), the surface of the NaSTFSI-SIPE is still covered by fluorine species but, as indicated by the XPS investigation, mostly associated with NaF originating from the FEC's decomposition.[151]

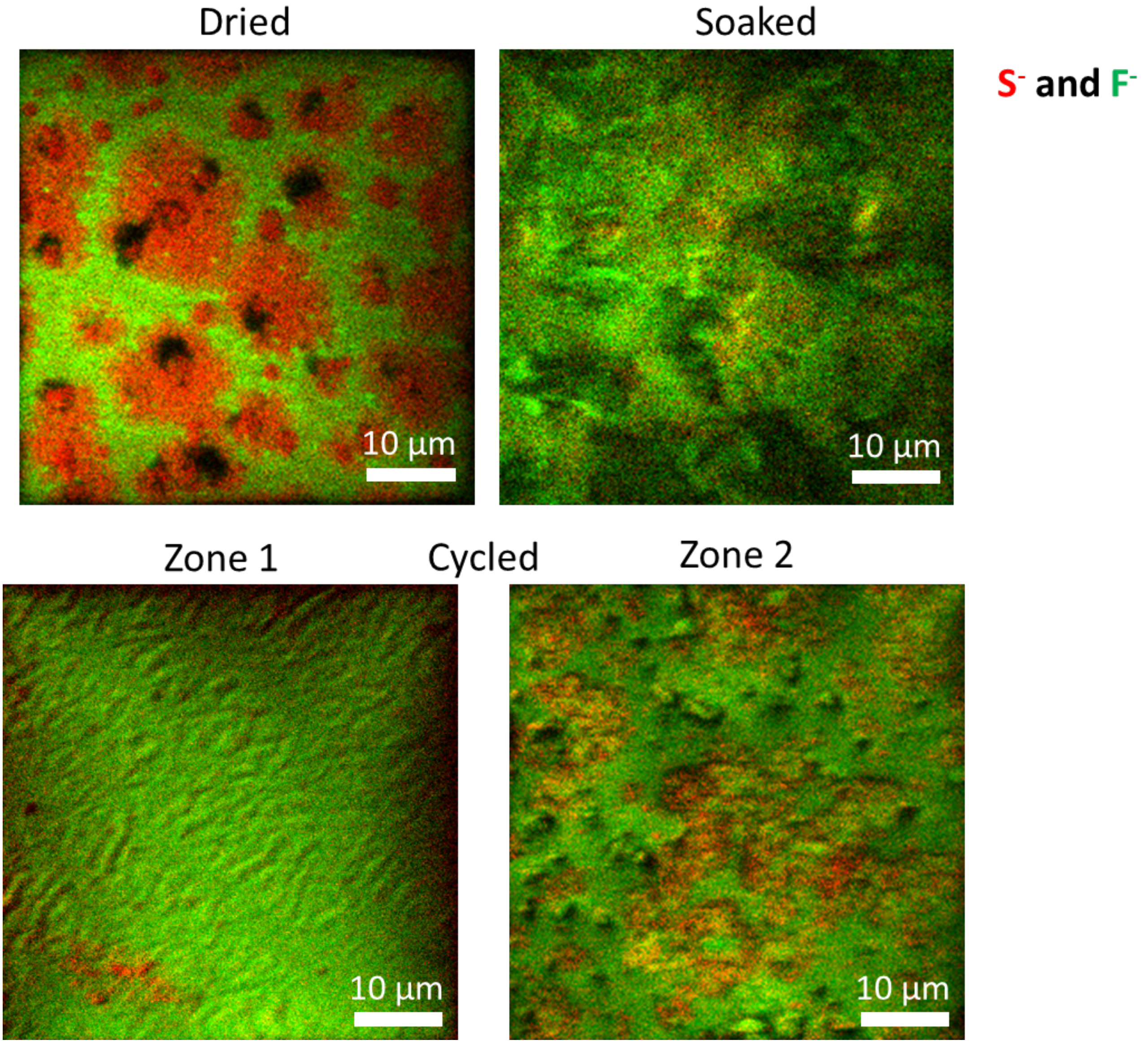

Figure 5.7: ToF-SIMS combined mappings of S- (red) and F- (green) ionic fragments on the surface of the NaSTFSI-SIPE (dried), incorporating EC:DMC:FEC molecular transporters (soaked) and two zones after cycling for 5 cycles in a Na||Na symmetric cell under 10 µA cm^{-2} (cycled).

The surface of cycled NaSTFSI-SIPE has been investigated in two different regions (Zone 1 and Zone 2). Although both regions show high concentrations of fluorine species, the Zone 2 mapping indicates larger areas with higher S-containing compounds. Nonetheless, NaF is also present, confirming the beneficial effect of FEC to induce the formation of a NaF-rich SEI and, thus, stabilizing the SEI and providing excellent compatibility to the NaSTFSI-SIPE against sodium-metal.

5.1.5 Electrochemical Performance of NaSTFSI-SIPE SMBs

The designed NaSTFSI-SIPE was further investigated in proof of concept, quasi-solid-state sodium-metal cells employing PW as the cathode. Before assembling the quasi-solid-state sodium-metal cells, the PW electrodes were dried at 140 °C at 10^{-7} bar to remove the water molecules and induce the formation of a phase transition from a hydrated to dehydrated rhombohedral crystal structure, finally obtaining a chemical composition of $Na_2Fe[Fe(CN)_6]$. It was observed that PW electrodes dried in mild conditions, such as 140 °C at 10^{-3} bar, maintained the water molecules, resulting in a low specific capacity for delivery (Figure 5.8).

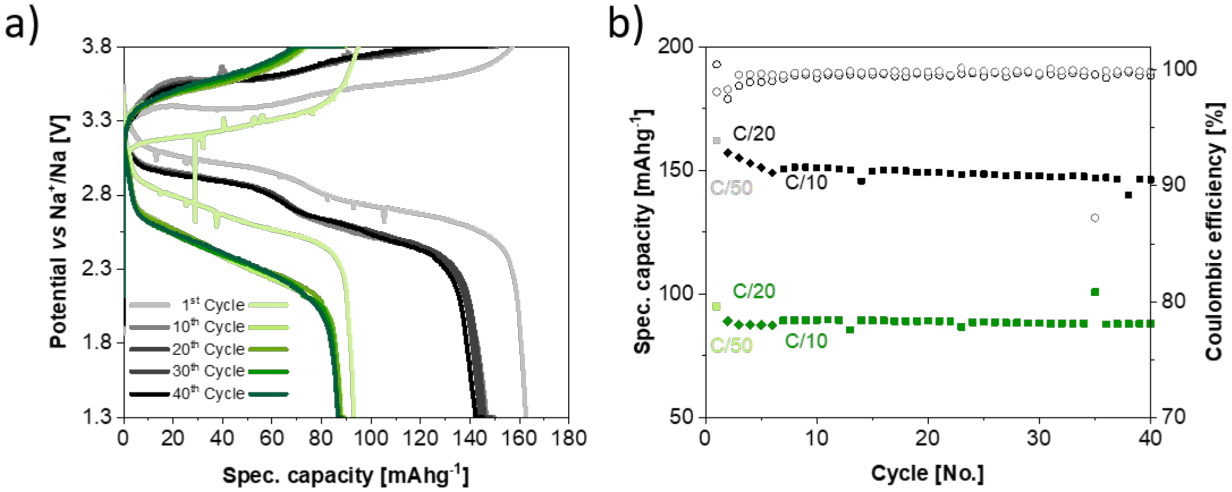

Figure 5.8: a) Voltage profile and b) cycling performance of hydrated (green) and dehydrated (black) PW cathode using NaSTFSI-SIPE at 40 °C.

The collected voltage profiles and the specific capacity upon cycling of Na‖1M $NaPF_6$ in EC:DEC (3:7 vol%)‖PW cells are illustrated in Figure 5.9a and b, respectively. In this electrolyte, the voltage profile of rhombohedral PW shows two plateaus at 3.0 and 3.3 V vs Na^+/Na. The initial charge and discharge capacity of PW were 154 and 160 mAhg^{-1}, respectively, at 0.02C. The specific capacity decayed slightly upon cycling by increasing the current from 0.02C to 0.03C and 0.1C, but the cell showed a specific capacity of 150 mAhg^{-1} and a Coulombic efficiency above 99% after 40 cycles.

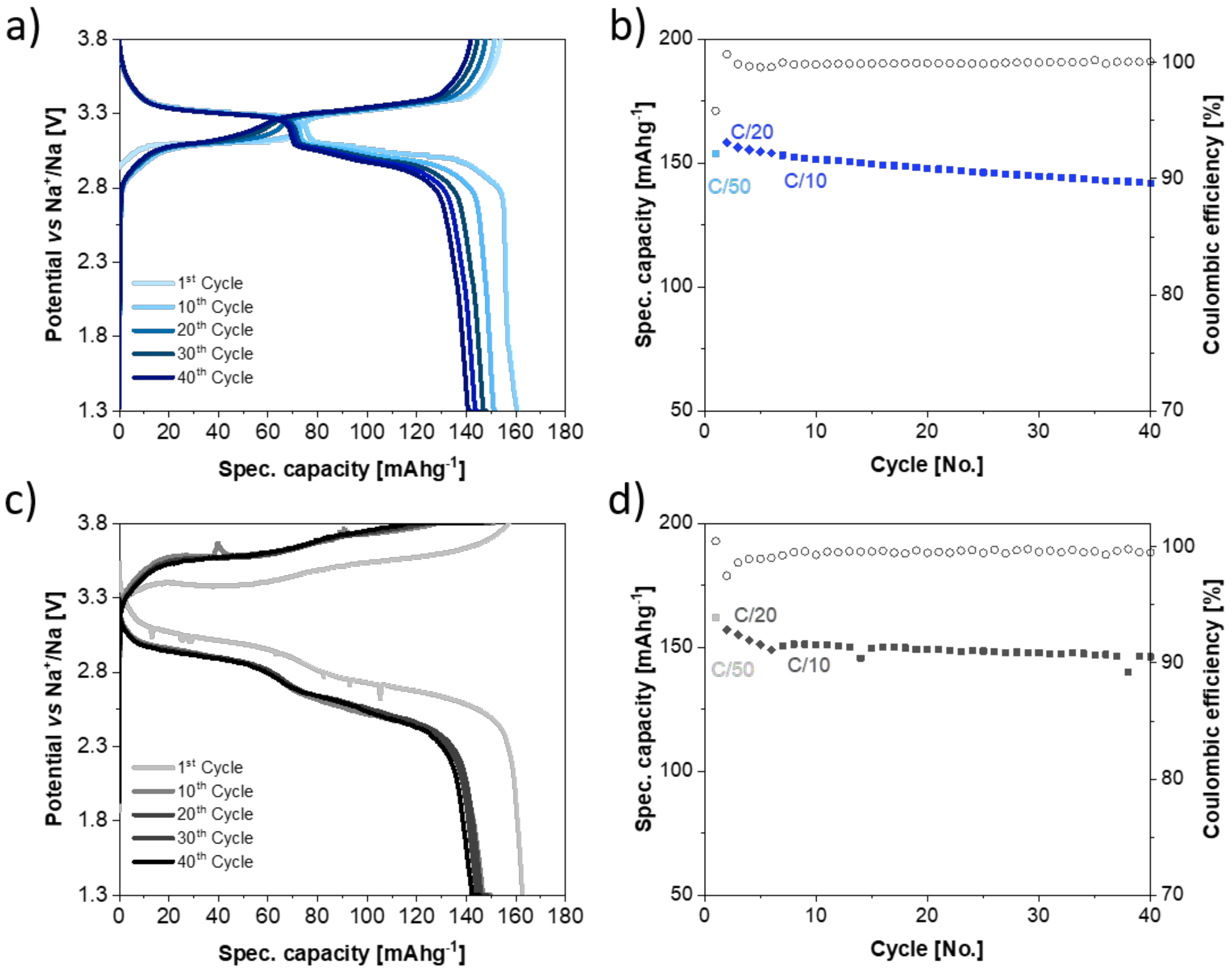

Figure 5.9: Voltage profile and cycling performance of PW cathode using a,b) 1M NaPF$_6$ in EC:DEC (3:7 vol%) liquid electrolyte and c,d) NaSTFSI-SIPE at 40 °C.

The voltage profiles of the PW tested with NaSTFSI-SIPE (Figure 5.9c) show also two voltage plateaus upon both the charge and the discharge. However, due to the lower NaSTFSI-SIPE ionic conductivity, the quasi-solid-state sodium-metal cell exhibited high polarization and sloping plateaus. The initial charge and discharge curves show a noisy signal due to side reactions and the corresponding SEI formation, as observed by XPS and ToF-SIMS experiments. Indeed, this is in agreement with the lower initial Coulombic efficiency. The noisy signal upon discharge could also be attributed to soft Na dendrites formation, which cannot be excluded. The observed overpotential of 0.4 V was expected considering the Na||Na symmetric stripping plating test. In addition, a similar overpotential was observed when Na||PW cell was tested with NaFSI in poly(trimethylene carbonate (PTMC) polymer electrolyte.[152] However, the large polarization does not influence the specific capacity of the quasi-solid-state sodium-metal cell, where the initial charge and discharge capacity of the PW at 0.02C correspond to 163 and 162 mAh g^{-1}, respectively, which are similar to those obtained in liquid cells. The cell capacity slightly dropped to 150 mAh g^{-1} and 147 mAh g^{-1} when increasing the current to 0.03C and 0.1C, respectively. However, although the capacity decays in the first cycles at 0.2C, after 5 cycles, the capacity and Coulombic efficiency remain constant, delivering a capacity retention of 98% after 40 cycles. This might be due to the stabilization of the SEI, as observed in the Na||Na symmetric cells. These preliminary results indicated the suitability of the designed NaSTFSI-SIPE for QSSSMBs.

5.1.6 Conclusion on the Performance of NaSTFSI-SIPE

The first part of this thesis showed the successful synthesis of a new, three-dimensional SIPE, consisting of in-house synthesized NaSTFSI, and PETMP, PET4A, and PVDF-HFP, as confirmed by IR, NMR and CPMAS-NMR. The SIPE, exhibiting a high thermal stability up to 280 °C, was electrochemically examined after incorporation of molecular transporter (EC:DMC:FEC, 50 wt%). The SIPE showed an electrochemical stability window up to 4.5 V vs. Na^+/Na and an ionic conductivity of $1.3\cdot10^{-4}$ S cm^{-1} at 90 °C and $1.4\cdot10^{-5}$ S cm^{-1} at RT. The NaSTFSI-SIPE showed highly stable cycling behavior against sodium-metal (more than 2000 h at 50 μA cm^{-2} at 40°C) due to the formation of a stable NaF-rich SEI, confirmed by EIS, XPS, and ToF-SIMS. Furthermore, PW||NaSTFSI-SIPE||Na QSSSMB cells operating at 40 °C delivered a first cycle specific capacity of 147 mAh g^{-1} at 0.1C with excellent Coulombic efficiency, comparable with liquid electrolyte-based cells. The cell was successfully cycled for 40 cycles with a capacity retention of 98 %. The obtained NaSTFSI-SIPE ranked among the top 5 Na-based SIPEs in terms of conductivity (Table 2.1) with comparable thermal and electrochemical stability. However, the expected high ionic conductivity of the lithium analogue[82] could not be reached. The differences might be due to a) the larger ionic radius of Na ions and following a larger coordination shell, resulting in slower movement through the polymer matrix, b) a stronger ion-polymer interaction of Na ions with the anionic center or c) the ionic conductivity of Na ions depends more on the polymer chain movement compared to Li ions due to the stronger ion-polymer interactions. To address these issues, additional insight into the polymer structure is required, which will be studied in the next chapter.

Chapter 5.2
Component-Driven Influence in NaSTFSI-SIPEs

The designed SIPE (NaSTFSI-SIPE) proved its functionality working as a QSSPE for SMBs in a proof-of-concept Na||SIPE||PW cell, however, the thermal, mechanical and electrochemical properties can potentially still be improved, thus, a deeper understanding of the polymer electrolyte is required. The synthesized polymer electrolyte consists of various components such as PETMP, PET4A, PVDF-HFP and NaSTFSI as well as the plasticizers, which work together to form and stabilize the self-standing three-dimensional polymer network and to enable efficient charge transport. The influence of each component was investigated to understand how each of them impacts the polymer electrolyte and which component ratio results in the best electrochemical performance.

5.2.1 Optimizing the Ratio of the Backbone Monomers

The main building blocks of the NaSTFSI-SIPE are PET4A and PETMP, which bind together via chemical bonding of the vinyl group of PET4A and the thiol group of PETMP. The fractions of bound and unbound groups of both components are critical parameters, as an excess of one of the groups would lead to a mismatch of both components and a homopolymerization of one of the components. PET4A or PETMP-based homopolymer regions, called sub-clusters, are not ionic conducting, since the SSM and the backbone monomers might not be in the desired ratio. Thus, the resulting structure can be considered electrochemically inactive or poorly active. Following this, these sub-cluster formations decrease the electrochemical performance of the SIPE. In our previous work,[153] it was confirmed that the NaSTFSI-SIPE could properly operate as a quasi-solid-state electrolyte for SMBs.

To gain deeper insights into the enhancement of compositional properties, the impact of each component on the mechanical and electrochemical properties has been investigated. Theoretically, the best PET4A/PETMP mole ratio should be 1:1, allowing all functional groups of both backbone's components to bind together without leaving any component unreacted. However, this ideal ratio changes when introducing the SSM, in this particular case, NaSTFSI, which has a free terminal double bond (vinyl group) to bind with a free thiol group of PETMP. Thus, the optimal amount of PET4A has to be slightly decreased so that PETMP can match all the vinyl groups of PET4A and SSM. In order to evaluate the best ratio of PET4A in relation to PETMP and NaSTFSI, PET4A/PETMP molar ratio has been varied between 40% and 100% (in 15% steps), while the molar ratio of NaSTFSI and PVDF-HFP vs PETMP was kept constant at 20% and 44%, respectively (see Table 5.1). This resulted in NaSTFSI-SIPE membranes with molar ratios ranging between 2:10:4:4.4 and 2:10:10:4.4 (NaSTFSI:PETMP:PET4A:PVDF-HFP), labeled as T1 to T5, respectively. From visual inspection, the optimal PET4A/PETMP molar ratio appears to be between 70% and 85% (Figure S8.2). Indeed, at low molar ratios (i.e., T1: 40% and T2: 55%), the thiol groups of excess PETMP might be involved in side reactions, leading to a homopolymerization not forming a self-standing membrane. Meanwhile, high molar ratios (T5: 100%) result in the formation of sub-regions in the membrane, as the excess PET4A units yield side reactions. However, both the 2:10:7:4.4 (T3) and 2:10:8.5:4.4 (T4) (NaSTFSI:PETMP:PET4A:PVDF-HFP) compositions result in self-standing membranes.

Although both SIPE membranes visually look appropriate, the former (T3) is more homogeneous, less brittle, and more flexible. Additionally, more functional groups of PETMP are available for the SSM to connect with and was thus used for follow-up tests, where the SSM content was increased up to 24 mol%. Nevertheless, further optimization tests should be carried out in the range of 70%-85% to identify the optimal SIPE composition, as well as mechanical studies to support the selection of the best composition.

Table 5.1: Composition of the dry NaSTFSI-SIPE membranes used for the evaluation of the influence of the PET4A content on the SIPE membranes.

	Molar ratio [mol]				**Composition [mol%]**	**Investigated factor**
SIPE	**NaSTFSI**	**PETMP**	**PET4A**	**PVDF-HFP**	**NaSTFSI|PETMP| PET4A|PVDF-HFP**	**PET4A to PETMP mol%**
T1	2	10	4	4.4	10|49|19|22	40%
T2	2	10	5.5	4.4	9|46|25|20	55%
T3	2	10	7	4.4	9|42|30|19	70%
T4	2	10	8.5	4.4	8|40|34|18	85%
T5	2	10	10	4.4	8|38|37|17	100%

5.2.2 Optimizing the PVDF-HFP Content

Although the stability of the NaSTFSI-SIPE originates from the PET4A/PETMP backbone, it is additionally supported by PVDF-HFP. PVDF-HFP does not chemically bind to any of the components but improves the overall mechanical properties upon the molecular solvent addition needed to increase the ionic conductivity of the electrolytic membrane. Taking constant the molar ratio of PET4A, PETMP, and NaSTFSI to 2:10:7, the number of PVDF-HFP units was varied between 0 and 11 (i.e., from 2:10:7:0 to 2:10:7:11 in NaSTFSI:PETMP:PET4A:PVDF-HFP). A total of six different compositions were explored labeled as P1 to P6 (Table 5.2), respectively.

Table 5.2: Molar ratios of dry NaSTFSI-SIPE membranes used for the assessment of the influence of PVDF-HFP on the SIPE.

	Molar ratio [mol]				**Composition [mol%]**	**Investigated factor**
SIPE	**NaSTFSI**	**PETMP**	**PET4A**	**PVDF-HFP**	**NaSTFSI|PETMP|PET4A|PVDF-HFP**	**Molar% of PVDF-HFP**
P1	2	10	7	0	11|53|36|0	0%
P2	2	10	7	2.2	10|50|30|10	10%
P3	2	10	7	4.4	10|43|29|18	18%
P4	2	10	7	6.6	8|40|26|26	26%
P5	2	10	7	8.8	7|36|25|32	32%
P6	2	10	7	11	7|34|23|36	36%

PVDF-HFP did not negatively influence either the membrane stability or the homogeneity of the different SIPEs in the examined range (Figure 5.10). Therefore, the thermal and electrochemical stability of the six SIPE membranes with compositions between 2:10:7:0 (P1, 0% PVDF-HFP) and 2:10:7:11 (P6, 36 mol% PVDF-HFP) were evaluated to select the optimal composition.

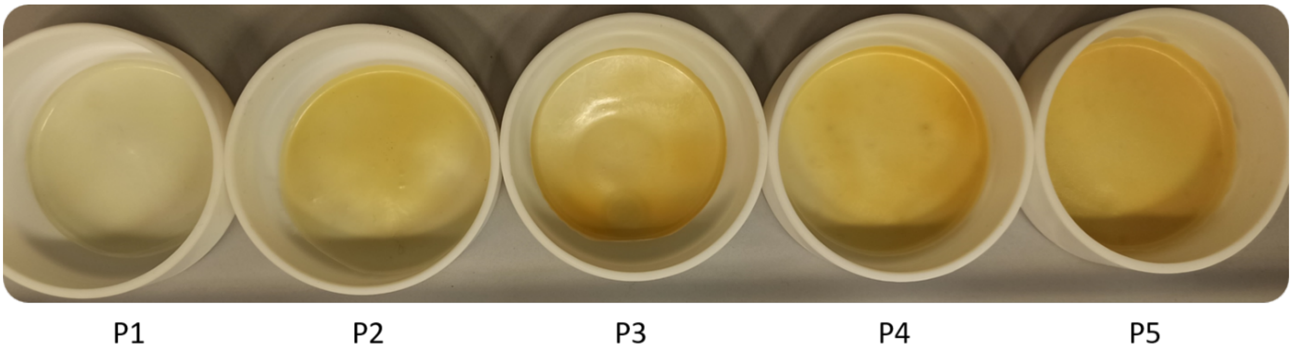

Figure 5.10: Photographs of NaSTFSI-SIPE membranes synthesized for the optimization of the PVDF-HFP content. The molar ratio of PET4A, PETMP, and NaSTFSI (2:10:7) was kept constant. Table 5.2 shows the chemical molar ratio of NaSTFSI-SIPE membranes.

The thermal stability was studied by TGA (Figure 5.11a) by heating the membranes up to 600 °C under Helium flow. All NaSTFSI-SIPE membranes are thermally stable up to 300 °C, which is comparable to other Na-based SIPEs.[104,107,139,153] The main difference between the various membranes is the increasing residual weight, which increases with increasing PVDF-HFP content.

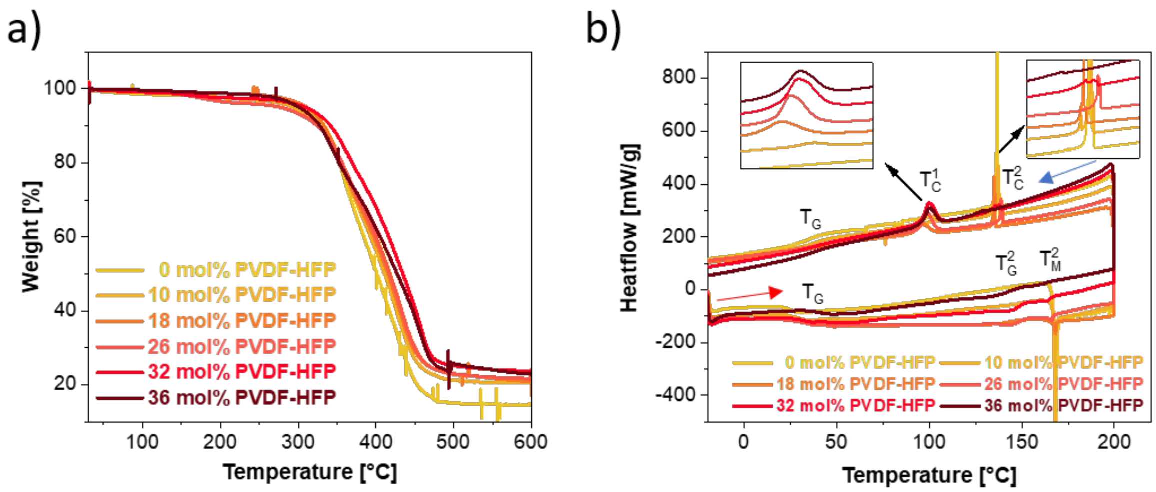

Figure 5.11: a) TGA (heating rate of 5 K min^{-1}, inert He atmosphere), and b) DSC (two cooling and heating cycles between -20 and 200 °C with a 5 K min^{-1} rate) of the dried NaSTFSI-SIPEs with different PVDF-HFP ratios from 2:10:7:0 (0% PVDF-HFP) to 2:10:7:11 (36 mol% PVDF-HFP).

In addition, DSC investigation has been carried out, involving a heating from -20 °C up to 200 °C and cooling back to -20 °C (Figure 5.11b). The scan shows an increase in the heat flow at 40 °C for all SIPEs for the heating (lower) and cooling (upper) scan, which matches the glass transition temperature (T_g) observed for this specific type of PETMP/4A-based SIPE.[153] The NaSTFSI-SIPEs with molar compositions between 2:10:7:4.4 (P3, 18 mol% PVDF-HFP) and 2:10:7:11 (P6, 36 mol% PVDF-HFP) show a crystallization point at 100 °C (T_c1), which can be linked to the crystallization of PVDF-HFP chains (Figure 5.12),[154] while the SIPEs with molar compositions between 2:10:7:0 (P1, 0% PVDF-HFP) and 2:10:7:8.8 (P5, 32 mol% PVDF-HFP) show a crystallization point at 140 °C (T_c^2), which can be linked to the crystallization of the NaSTFSI-SIPE's backbone. The intensity of the T_c^1 peak increases, while that of the T_c^2 peak decreases with an increasing PVDF-HFP content, suggesting that higher amounts of PVDF-HFP hinder the natural crystallization of the NaSTFSI-SIPE's backbone upon cooling, while PVDF-HFP chains crystallize once the amount is high enough to be completely enclosed or entangled inside the SIPE network.

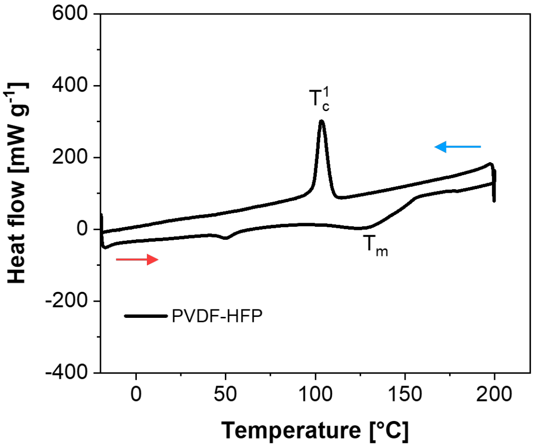

Figure 5.12: DSC of pure PVDF-HFP with a cooling and heating cycle between -20 and 200 °C at a rate of 5 K min^{-1}.

In addition, during the heating cycle, the SIPE membranes with PVDF-HFP amounts between 0% and 18% show a melting point (T_m2) at 168 °C, which can be linked to the rearrangement of the NaSTFSI-PET-MP/4A polymer into a more stable and less crystalline structure. The NaSTFSI-SIPEs with ratios between 2:10:7:6.6 (P4, 26 mol% PVDF-HFP) and 2:10:7:11 (P6, 36 mol% PVDF-HFP) do not show this melting point, but instead indicate a second glass transition point (T_g^2) at 140 °C, which can be linked to a reorganization of the NaSTFSI-PET-MP/4A polymer network. The intensity of both peaks is reduced with higher amounts of PVDF-HFP, as more PVDF-HFP results in narrower space, which creates a more amorphous structure and makes it even harder for the PETMP/4A network to crystallize, melt, or rearrange. Additionally, a high concentration of PVDF-HFP can result in the entanglement of PVDF-HFP chains with each other, which additionally could hinder the movement of the backbone during the heating (T_g^2) and cooling (T_c^2) cycle.[155–157]

The EC:DMC:FEC (49:49:2 vol.%) solvent mixture was incorporated as a molecular transporter into the NaSTFSI-SIPEs with a varying PVDF-HFP content to be used as electrolytes. The amount of the molecular transporter composition spontaneously uptaken by the different SIPEs was measured 3 times at 5 different positions of the membrane to provide a representative value (Figure 5.13a). The uptake varied between 45 and 65 wt.%. The relationship between the molecular transporter uptake and the PVDF-HFP content trend indicates a bell-shaped curve with a maximum at 32 mol% PVDF-HFP. However, considering the larger error of the P6 (36 mol% PVDF-HFP) it might also be possible that this bell-shaped curve could represent a plateau, reflecting the maximum amount of molecular transporters that the SIPE can absorb, which is around 60 wt.%. Importantly, the amount of molecular transporter uptaken by the SIPE membranes influences the electrochemical properties, particularly ionic conductivity This suggests that the first hypothesis of a bell-shaped trend is more plausible.[142,158]

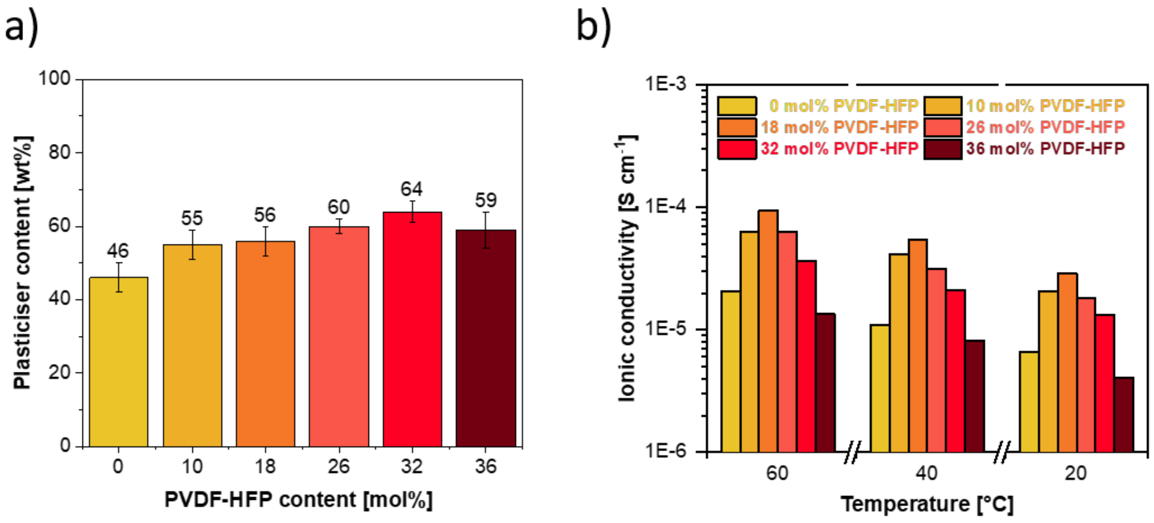

Figure 5.13: a) Molecular transporter (EC: DMC: FEC in 49: 49: 2 vol. ratio) uptake in wt.% and b) temperature-dependent ionic conductivity at 20, 40 and 60 °C of swelled NaSTFSI-SIPEs with different PVDF-HFP ratios from 0% PVDF-HFP to 36 mol% PVDF-HFP.

In fact, the ionic conductivity measured at 20, 40, and 60 °C (Figure 5.13b) support this, a it also displays a bell-shaped trend at all temperatures, with an overall increase in ionic conductivity as temperature rises. This temperature range was chosen because most practical applications of solid-state batteries operate above room temperature. Therefore, 20-60 °C represents a relevant and realistic temperature range for these batteries. This trend can be explained by the DSC results, which are linked with the amount of PVDF-HFP and the concentration of SSM in the membrane. On the one hand, the amount of PVDF-HFP that can be inside the membrane without creating excess PVDF-HFP regions that disrupt the natural behavior of the polymer backbone ($T_c^2$2 and T_m^2 still present) was found to be $>$ 18 mol% (from P3 to P6). On the other hand, the SSM concentration decreases with increasing PVDF-HFP content from P3 (10 mol%) to P6 (7 mol%). The lower amount of SSM results in a lower amount of Na ions, which leads to a decrease in ionic conductivity. Hence, P3 NaSTFSI-SIPE was selected due to the highest ionic conductivity at all temperatures, reaching an ionic conductivity of $2.9\cdot10^{-5}$ and $9.39\cdot10^{-5}$ S cm^{-1} at 20 to 60 °C, respectively.

5.2.3 Optimizing the Sodium Salt Monomer Content

Finally, the amount of SSM has been investigated since it is crucial for the ionic conductivity, as more anionic centers correspond to larger number of Na ion carriers as well as closer sites for charge transfer, facilitating the Na ion transport. The effect of the NaSTFSI content in NaSTFSI-SIPE was studied by varying its content (Table 5.3), while maintaining the molar ratio for the other components (x:10:7:4.4 SSM:PETMP:PET4A:PVDF-HFP).

Table 5.3: Investigated SSM ratios in the dry NaSTFSI-SIPE membranes.

	Molar ratio [mol]				**Composition [mol%]**	**Investigated factor**
SIPE	**NaSTFSI**	**PETMP**	**PET4A**	**PVDF-HFP**	**NaSTFSI|PETMP|PET4A|PVDF-HFP**	**Molar% of NaSTFSI**
M1	1	10	7	4.4	4|48|29|19	4%
M2	2	10	7	4.4	9|44|28|19	9%
M3	3	10	7	4.4	13|43|26|18	13%
M4	4	10	7	4.4	17|40|25|18	17%
M5	5	10	7	4.4	20|38|25|17	20%
M6	6	10	7	4.4	23|36|25|16	23%

The NaSTFSI-SIPEs with compositions between 1:10:7:4.4 (M1) and 4:10:7:4.4 (M4) were homogeneous and self-standing polymer membranes, while M5 and M6 showed inhomogeneities and cracks, and were not considered as possible candidate due to concerns about reproducibility and scalability (Figure S8.3). The observed inhomogeneities that occur in M5 and M6 can be explained by unwanted side reactions that occur through the mismatch of too many vinyl groups in relation to thiol groups. The highest ratio of NaSTFSI that results in a homogeneous membrane consists of a ratio of 4:10:7:4.4 (M4), which means that 70% of the four thiol groups of each PETMP molecule are matched with PET4A vinyl groups and 10% are matched with NaSTFSI vinyl groups. The remaining 20% of thiol groups are not bound to one of the other two monomers but face the supporting polymer PVDF-HFP, which has fluorine covering its surface, attracting the protons of the thiol groups. The thermal and electrochemical properties of M1 through M4 NaSTFSI-SIPE self-standing membranes, incorporating around 50 wt.% of carbonate-based molecular transporter (for the electrochemical properties), were investigated. The TGA curve (Figure 5.14a) shows thermal stability up to 300 °C for all studied NaSTFSI-SIPE dry membranes, comparable with other Na-based SIPEs[104,107,139,153]. The different SIPE membranes show comparable thermal stabilities independent of the SSM content, suggesting that the monomer content does not influence the thermal stability of the SIPE and that all components are either chemically bonded or enclosed in the SIPE.

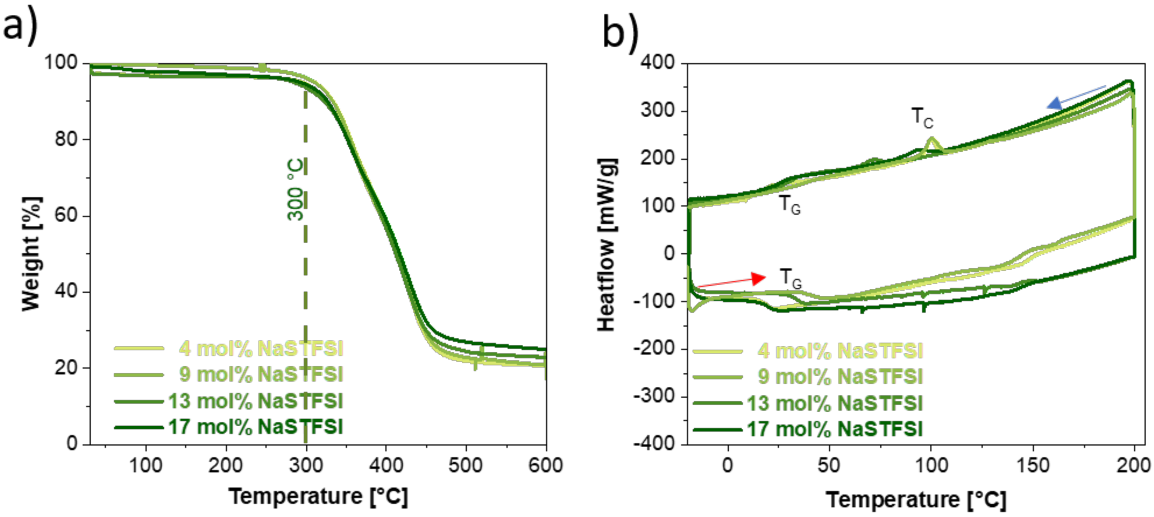

Figure 5.14: a) TGA (heating rate of 5 K min^{-1}, inert He atmosphere), and b) DSC (two cooling and heating cycles between -20 and 200 °C with a 5 K min^{-1} rate) of the dry NaSTFSI-SIPE with various SSM concentrations.

The DSC scan (Figure 5.14b) is in agreement with the TGA when heating from -20 °C up to 200 °C and back to -20 °C. The scan shows a TG at 40 °C and a crystallization feature at 100 °C (T_c1), which can be linked to the crystallization of PVDF-HFP chains (Figure 5.12).[154]

The four SIPE membranes were further electrochemically characterized after the incorporation of EC:DMC:FEC (49:49:2 vol.%). First, the ionic conductivity of the NaSTFSI-SIPEs was tested at different temperatures between 10 and 90 °C (Figure 5.15a). The ionic conductivity increases with increasing temperature as commonly observed for SIPEs.[142,158] More interestingly, the ionic conductivity increases with an increasing NaSTFSI content, reaching a maximum of $2.2 \cdot 10^{-4}$ S cm^{-1} at 90 °C for the membrane with the 4:10:7:4.4 composition (M4, 17 mol% NaSTFSI). This trend supports the assumption that more anionic centers result in a higher number of Na ion charge carriers and a shorter distance that each Na ion has to travel between two anionic centers.

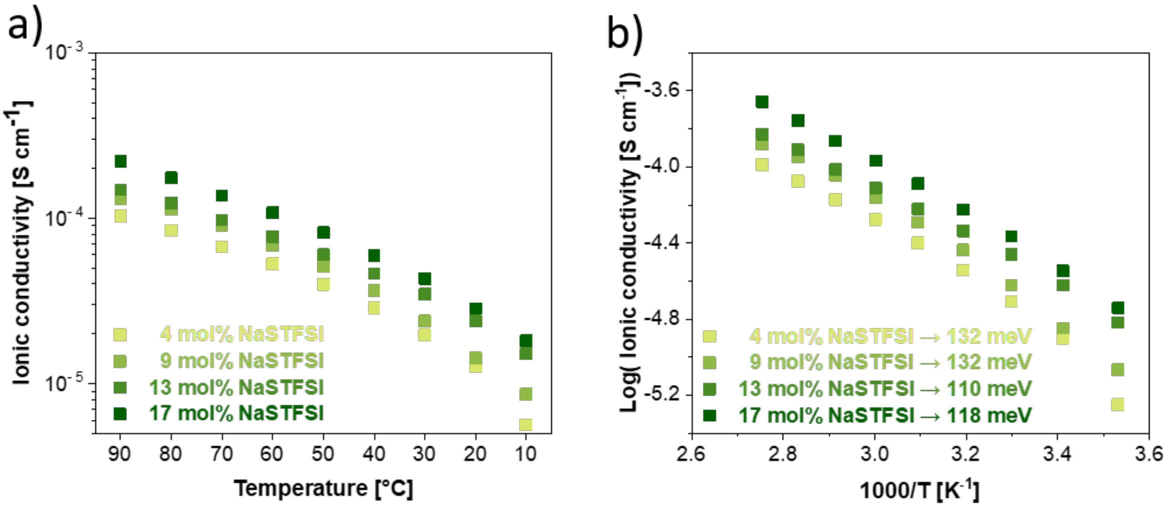

Figure 5.15: a) Temperature-dependent ionic conductivity, and b) activation energy of the NaSTFSI-SIPEs with different NaSTFSI contents (from 1:10:7:4.4 to 4:10:7:4.4) and EC:DMC:FEC molecular transporter incorporation.

The activation energy for Na ion transport (Figure 5.15b) in the investigated temperature range is between 132 and 118 meV for the M1 to M4 SIPEs with a tendency towards lower activation energy with a higher number of Na ion carriers, most likely due to closer proximity of the anionic centers. Considering the previous results, the NaSTFSI-SIPE with the 4:10:7:4.4 mole composition (M4, 17 mol% NaSTFSI), which shows the highest ionic conductivity, as well as the 2:10:7:4.4 mole composition (M2, 9 mol% NaSTFSI), having the composition comparable to the previously published SIPE,[153] have been implemented in symmetric Na||Na cells to examine the Na stripping/plating behavior, the stability against sodium-metal and the SEI formation upon cycling (Figure 5.16a). Both NaSTFI-SIPEs show stable cycling up to 50 µA cm^{-2} with no visible increase in overpotential. However, the overpotential of M2 (2:10:7:4.4) decreases upon continuous cycling at 50 µA cm^{-2}, stabilizing around 0.46 V. Meanwhile, the overpotential of M4 (4:10:7:4.4) remains stable at 0.58 V.

Impedance analysis have been conducted to identify potential differences in SEI formation. Figure 5.16b and 5.16c display the Nyquist plots of Na cells using M2 and M4 as electrolyte, respectively, after the first and last cycles at each applied current density. The M2-containing cell exhibits slightly lower overall resistance compared to M4 cells. In the case of M2, the resistance decreases upon cycling and increasing the current density. In contrast, the M4-based cell shows higher overall resistance, which increases during the initial cycles and at low currents but remains constant after applying 40 µA cm^{-2}. These results align with the trends observed in overpotential, suggesting that the higher fluorine content in M4 led to the formation of a thicker NaF-rich interphase, as previously investigated in our group,[153] due to the reactivity with the surface of Na metal. In addition, the increased resistance associated with NaF may contribute to the higher overpotential seen in M4 cells, such as LiF.[159] In the case of the M2-based cell, the decreasing overpotential suggests that the SEI is decomposing upon cycling and is likely unstable, potentially due to a lower NaF formation, which is highly soluble in carbonate molecular transporters (3.057 mg L^{-1}).[160]

The M2 and M4 NaSTFSI-SIPE were investigated in quasi-solid-state sodium-metal cells employing PW as cathode as a proof-of-concept. The voltage profiles of Na||PW cells, using both SIPEs, are shown in Figure 5.16d and 5.16e, respectively. The initial charge and discharge capacities of the cell employing M4 at 0.05C are 144 and 141 mAh g^{-1}, while those of the cell containing M2 are 225 and 211 mAh g^{-1}, respectively. The Na||PW cell with M4 shows higher cell polarization and, thus, lower initial specific capacity compared to the cell with M2, which is in agreement with the stripping/plating tests. The lower polarization of the cell employing M2, on the other hand, results in a higher initial delivered specific capacity. In addition, the delivered specific capacity of the cell containing M2 is higher than the theoretical capacity of the PW (150 mAh g^{-1}), suggesting that the extra capacity is due to the contribution of side reactions, which agrees with the rapid capacity decay and poor Coulombic efficiency. Meanwhile, the voltage profile of the M4-based PW cell is rather stable upon cycling, showing the two characteristics plateaus of PW at 3.0 and 3.3 V vs Na^+/Na.

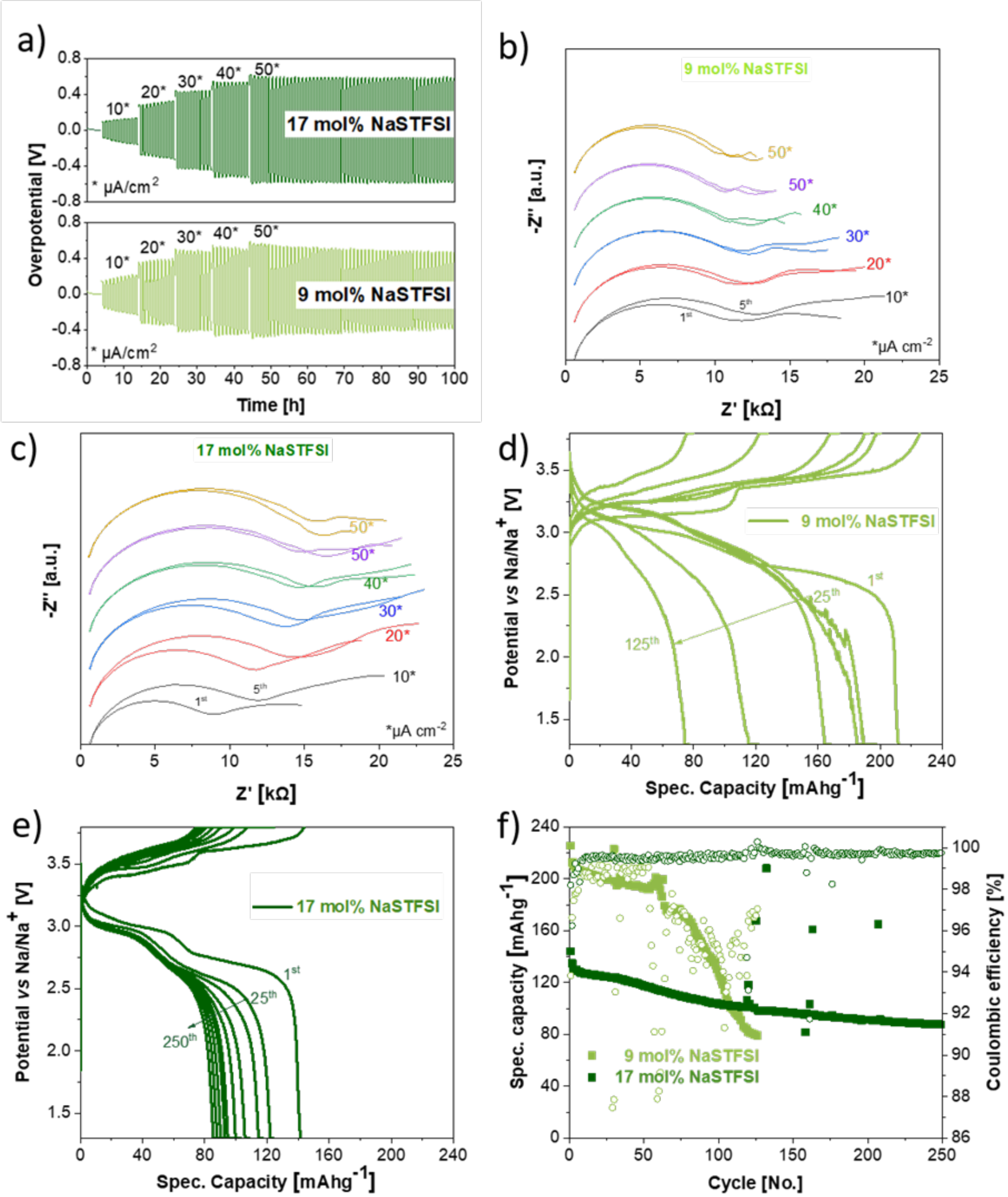

Figure 5.16: a) Na plating/stripping tests of Na‖M2‖Na and Na‖M4‖Na cells at different current densities at 40 °C. Nyquist plots after the initial and last cycles at different current densities in b) the Na‖M2‖Na and c) the Na‖M4‖Na cell. Voltage profiles of Na‖NaSTFSI-SIPE‖PW cells composed d) 2:10:7:4.4 (9 mol% NaSTFSI – light green) and e) 4:10:7:4.4 (17 mol% NaSTFSI – dark green), and f) the corresponding specific capacity and Coulombic efficiency upon cycling. EC:DMC:FEC (49:49:2 vol.%) molecular transporter is incorporated into all SIPEs. The galvanostatic cycling test with a current density of C/50 the 1st cycle, followed by 5 cycles at C/20 and ongoing ones at C/10 between 3.8 V and 1.3 V. All measurements were performed at 40 °C.

As already mentioned, the specific capacity upon long-term cycling test (Figure 5.16f) shows that the Na||PW cell employing M2 delivers an initially higher specific capacity than the M4-based cell (200 mAh g^{-1} vs. 125 mAh g^{-1}). However, the electrochemical performance of the former cell exhibits a fast and continuous fading, reaching 80 mAh g^{-1} after 120 cycles. Meanwhile, the Na||M4||PW cell shows more stable capacity, resulting in a longer-term cycling performance, delivering a specific capacity of 91 mAh g^{-1} after 200 cycles at 40 C (capacity retention of 68%). The cycling performance is in line with the Coulombic efficiency values. The M2-based cell shows an initial Coulombic efficiency of 93.8%, which increases up to 98.8% in the following 50-60 cycles, but then it drops down to 94% upon cycling, suggesting once more the occurrence of side reactions and electrolyte decomposition, as well as Na dendrite formation. In contrast, the cell with M4 exhibits an initial Coulombic efficiency of 98.2% that stabilizes around 99.9%. The highest stability upon cycling and the most stable overpotential upon stripping/plating support for the M4 SIPE to have a more homogeneous and stable SEI compared to the M2 SIPE and to have the best chemical composition among all investigated SIPEs.

5.2.4 Conclusion on the Component-Driven Influence

The influence of the different components of the SIPE was investigated to identify the best SSM:PETMP:PET4A:PVDF-HFP ratio in terms of electrochemical performance. First, the PET4A/PETMP ratio was studied and a molar ratio of 7 mol of PET4A to 10 mol of PETMP was found to result in the most stable and homogeneous membrane. Second, increasing amounts of PVDF-HFP showed to improve the solvent uptake of the membrane, which in turn improved the ionic conductivity up to a maximum with 18 mol% of PVDF-HFP. High amounts, however, showed to decrease the ionic conductivity due to enclosed PVDF-HFP regions. Third, the amount of NaSTFSI SSM was investigated and its positive influence on the ionic conductivity was confirmed. The ratio of 17 mol% of NaSTFSI in regards to the amount of PETMP resulted in the best electrolyte performance. The improved M4-SIPE (labeled as NaSTFSI-SIPE in the following chapters) reached an ionic conductivity of $2.84 \cdot 10^{-5}$ S cm^{-1} at RT (double compared with the initially developed NaSTFSI-SIPE from chapter 5.1) and $2.2 \cdot 10^{-4}$ S cm^{-1} at 90 °C (+70% compared to the initially developed NaSTFSI-SIPE). The M4-SIPE shows an improved thermal stability up to 300 °C and was successfully cycled in a Na||SIPE||PW cell at 0.1 C for 200 cycles with a capacity retention of 68%, which is a cycle life improvement of 200% compared to the previously developed NaSTFSI-SIPE. Nonetheless, the conductivity did not reach the

0.4 mS cm^{-1} required for application in EVs.[85] The strong ion-polymer interaction of the Na ions with the anionic centers of the polymer might be responsible for the low ionic conductivity, as the Na-based SIPEs in the literature (Table 2.1) use strongly delocalizing anionic charges to obtain high ionic conductivities.

Chapter 5.3
SSM Design with Varying Anionic Centers

Various SSMs carrying Na ions were synthesized to produce different SIPEs for sodium-based batteries. The mobility of Na ions inversely depends on the binding strength toward the anion, which is tethered to the backbone and is thus referred to as the anionic center. Increasing the anionic center size increases the delocalization of the negative charge, resulting in a weaker interaction between the anion and the cation, in turn improving the Na ion conductivity.

5.3.1 Structures of SSMs with Varying Anionic Centers

The effect of the anionic center's charge delocalization on the SIPE performance has been investigated using NaSTFSI, NaSDCM, or NaVBS SSMs (Figure 5.17) in SSM-PET-MP/4A-PVDF-HFP-based SIPE with the mole composition 4:10:7:4.4 (optimized from the section above). The three SSMs have the anionic centers attached to a benzene ring containing a vinyl group in para-position, which is used to build a chemical connection to the polymer backbone. However, NaSTFSI comprises a TFSI- group that widely delocalizes the negative charge on a nitrogen atom via two SO_2 groups, as well as a neighbored electron-drawing CF_3 group. Meanwhile, NaSDCM carries the negative charge on a carbon atom that has two neighbored CN groups to delocalize the charge, and NaVBS carries the negative charge on an oxygen atom that is attached to SO_2 group.

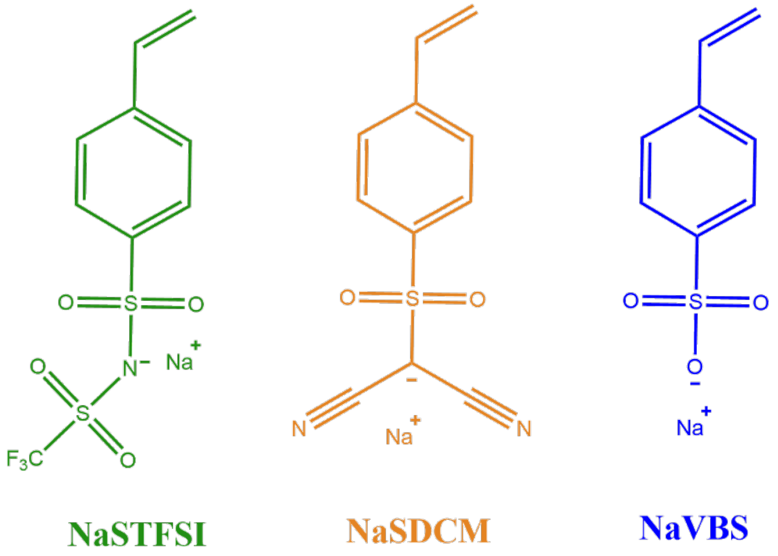

Figure 5.17: Chemical structure of the three investigated SSMs: NaSTFSI (green), NaSDCM (orange), and NaVBS (blue).

The thermal stability of the SIPE membranes, incorporating one of the three SSMs, was investigated by TGA measurements (Figure 5.18a). Each SIPE membrane is labeled by its containing SSM in the following. The NaSTFSI and NaVBS-based SIPEs remain thermally stable up to 300 °C, while the NaSDCM-based SIPE membrane shows slightly lower thermal stability (up to 250 °C). This reduced thermal stability can be linked to the C-CN bonds of the SDCM monomer.[161]

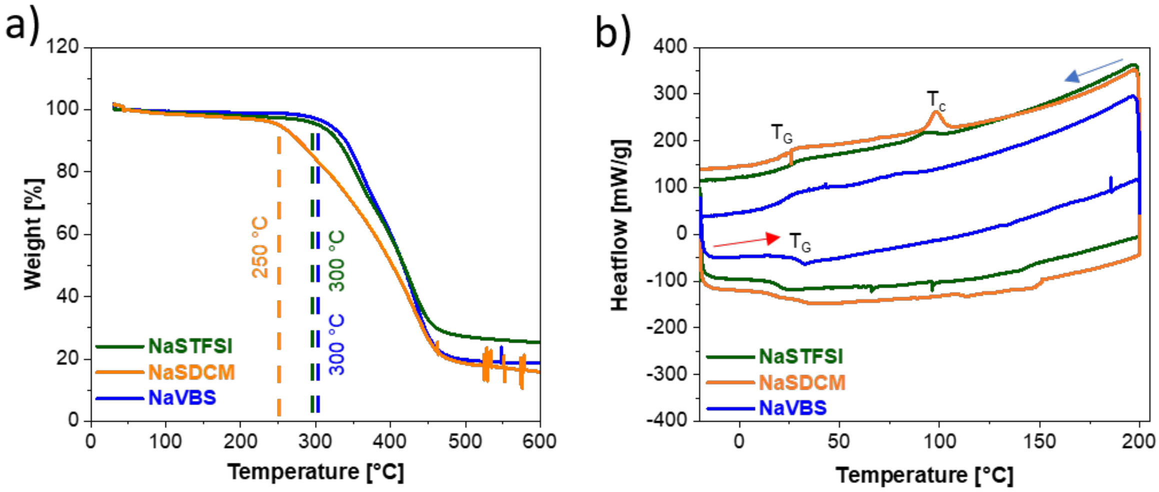

Figure 5.18: a) TGA (heating rate of 5 K min^{-1}, inert He atmosphere), and b) DSC (cooling and heating cycles between -20 and 200 °C with a 5 K min^{-1} rate) of the dried NaSTFSI-, NaSDCM-and NaVBS-SIPEs with the 4:10:7:4.4 molar composition.

The DSC measurements (Figure 5.18b) show a T_g at 40 °C for all samples and a T_c at around 100 °C for the NaSTFSI and NaSDCM-based SIPEs. The absence of a visible crystallization peak for the NaVBS-based SIPE indicates that the crystalline content of the polymer is smaller compared to the other SIPEs upon cooling. This can be explained by the small, unshielded negative SO_3 group, which has a stronger repulsive force against the PVDF-HFP chains and against itself compared to the other two SSMs. This increased repulsive force reduces the degree of crystallinity by hindering the formation of a semi-crystalline orientation of the membrane, thus, resulting in the absence of the crystallization peak.

5.3.2 Ionic Conductivity Dependence on Anionic Center

The ionic conductivity of the three SIPEs with 50 wt.% of molecular transporters was studied between 10 and 90 °C. The measurement was performed in two sweeps, starting at 20 °C and increasing to 90 °C, followed by cooling to 10 °C. All SIPEs show their capability to transport Na ions and reach ionic conductivities comparable to other SIPEs blended with PVDF-HFP.[107,139,142] The ionic conductivity (Figure 5.19a) results reveal that the NaVBS-SIPE shows the lowest ionic conductivity with $8.9 \cdot 10^{-6}$ S cm^{-1} at RT ($9.1 \cdot 10^{-5}$ at 90 °C), followed by NaSTFSI-SIPE, which reaches an ionic conductivity of $2.84 \cdot 10^{-5}$ S cm^{-1} at RT ($2.2 \cdot 10^{-4}$ at 90 °C), and NaSDCM-SIPE, which displays the highest ionic conductivity of $4.2 \cdot 10^{-5}$ S cm^{-1} at RT ($2.9 \cdot 10^{-4}$ at 90 °C), slightly higher to those observed in dry dual-ion SPEs and comparable with other Na-based SIPE.[107,139,142,162,163] These values match with the charge delocalization, i.e., dissociation energy, of the various SSMs with NaVBS having the weakest charge delocalization, i.e., the highest required dissociation energy and the lowest ionic conductivity. On the other hand, NaSDCM has the lowest dissociation energy and the highest ionic conductivity. This result clearly demonstrates the importance of the dissociation energy on the ionic conductivity, making it an essential parameter to consider when designing an SSM.

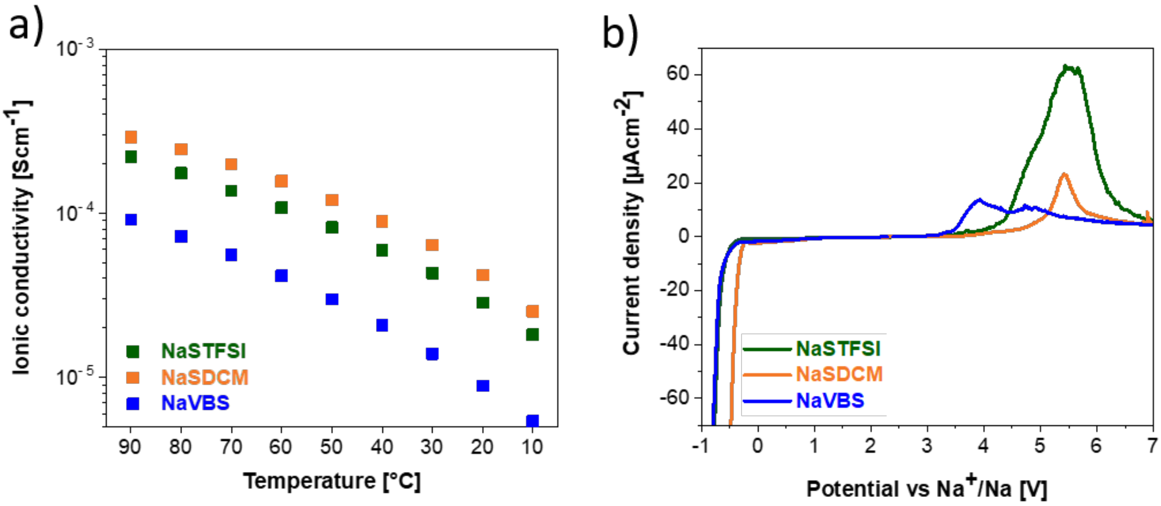

Figure 5.19: a) Temperature-dependent ionic conductivity and b) anodic and cathodic stability LSV curves (Na||SIPE||Al, scan rate of 30 µV s^{-1}, temperature 40 °C) of the NaSTFSI-, NaSDCM-, or NaVBs-SIPE with 50 wt.% of carbonate-based molecular transporters.

The electrochemical stability window of the different SIPEs has been investigated by LSV (Figure 5.19b). All of them do not show any limitation on the cathodic side prior to Na plating below 0 V vs. Na^+/Na. Only the NaSTFSI-SIPE displays a fragment at 0.25 V, which might be related to the remaining DMSO inside the SIPE. The current flowing during the anodic scan is higher for NaSTFSI- compared to NaSDCM- and NaVBS-SIPEs, which suggests that the NaSTFSI-base SIPE oxidizes faster than those consisting of NaSDCM or NaVSBs. More important, however, is the onset potential for the electrolyte oxidation, which is the lowest for NaVBS and the highest for NaSDCM. The former SIPE exhibits the current onset slightly above 3.0 V vs. Na^+/Na, suggesting a high reactivity of the -SO_3 group. The NaSDCM-SIPE instead shows rather high anodic stability with no current flowing below 4.5 V vs. Na^+/Na. Finally, NaSTFSI shows the anodic current flow starting at 4.0 V vs. Na^+/Na. These results support the highest resistance of the DCM anionic center (and the SIPE) toward oxidation, which combines well with its highest ionic conductivity.

5.3.3 Cycling Performance in Symmetric Sodium-Metal Cells

To further characterize the SIPEs, stripping and plating tests were performed in Na||Na symmetric cells (Figure 5.20), which showed an increase in the overpotential for all SIPEs when the current was increased from 10 to 50 µA cm^{-2}. The NaSTFSI-SIPE exhibits an initial overpotential of 0.3 V vs. Na$^+$/Na at 10 µA cm^{-2}, which increases with increasing current density to 0.52 V at 50 µA cm^{-2}. Meanwhile, the NaSDCM-SIPE displays a similar initial overpotential of 0.3 V at 10 µA cm^{-2}, which is slightly lower than NaSTFSI-SIPE upon cycling and increasing the current (e.g., 0.45 V). Moreover, the overpotential remains constant and slightly decreases upon cycling, suggesting that NaSDCM-SIPE exhibits a thinner and/or less resistive SEI and thus represents a better choice as an electrolyte for sodium-metal cells. Finally, the NaVBS-SIPE exhibits an initial overpotential of more than 0.4 V, which increases to 0.85 V at 50 µA cm^{-2}, indicating that this electrolyte cannot support high current densities and, therefore, was excluded from subsequent experiments. The interfacial resistance analysis supports this theory with a stabilizing ∼15 k interfacial resistance for the NaSTFSI-SIPE and ∼12 kΩ for the NaSDCM-SIPE upon cycling, while the NaVBS-SIPE does not show a stabilizing interfacial resistance at any current density.

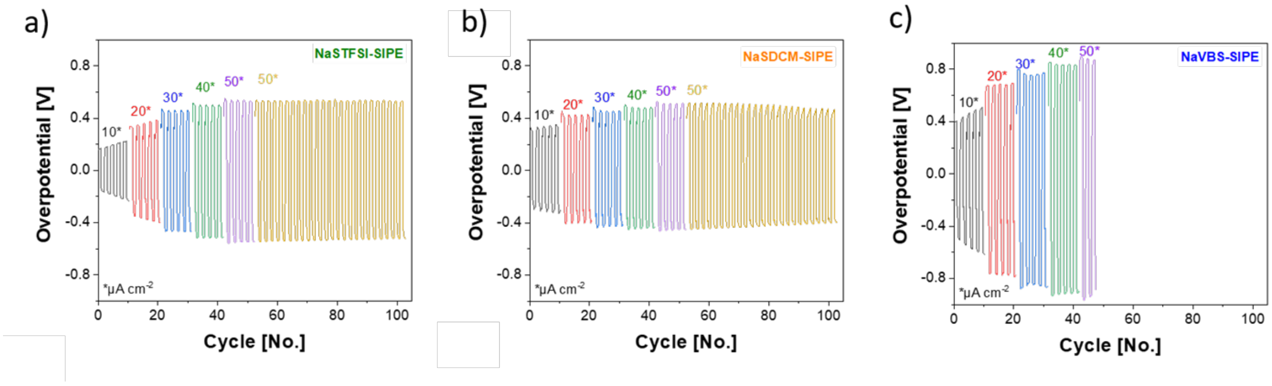

Figure 5.20: Stripping and plating tests of a) NaSTFSI-, b) NaSDCM- and c) NaVBS-SIPE at different current density at 40 °C.

5.3.4 Study of the Solid Electrolyte Interphase

The slightly lower overpotential observed for NaSDCM-SIPE when cycled at 50 µA cm^{-2} may be related to the formation of a thinner and less resistive SEI. An ex-situ XPS analysis was conducted to compare the SEI chemistry formed on the surface of NaSDCM-SIPE with that formed on NaSTFSI-SIPE after cycling Na‖Na symmetric cells. Figure 5.21 displays the high-resolution C 1s, F 1s, and S 2p photoelectron regions for NaSDCM-SIPE, while Figure 5.5 shows the corresponding regions for NaSTFSI-SIPE. The C 1s spectrum reveals five main species: hydrocarbons (C–C at 285.0 eV), carbon-oxygen species, including ether-based species (C-O at 286 eV) and -COx- (287 eV), carbonates (-CO at 290 eV), and carbon–fluorine-containing compounds (-CF at 291 eV).[132,145] These species are indicative of the molecular transporter mixture and its reduction products,[146] consistent with those detected for NaSTFSI-SIPE.[153] Notably, the F 1s spectrum shows that the fluorine-containing species undergo dehydrofluorination, resulting in the formation of NaF (684 eV).[149,150,153] However, the degradation of these species to form NaF is less pronounced in NaSDCM-SIPE compared to NaSTFSI-SIPE, suggesting a lower degree of decomposition and a thinner SEI. The main peaks in this region are associated with C-F species originating from PVDF-HFP.[145] Similarly, the S 2p spectrum indicates that the primary compound is SIPE (S-H/S-C at 164 eV), with a lower concentration of -SOx- (169 eV) species observed, contrasting with the findings for NaSTFSI-SIPE. These results demonstrate that NaSDCM is more stable against Na metal than NaSTFSI-SIPE, leading to the formation of a thinner SEI that results in a lower overpotential and a less resistive layer.

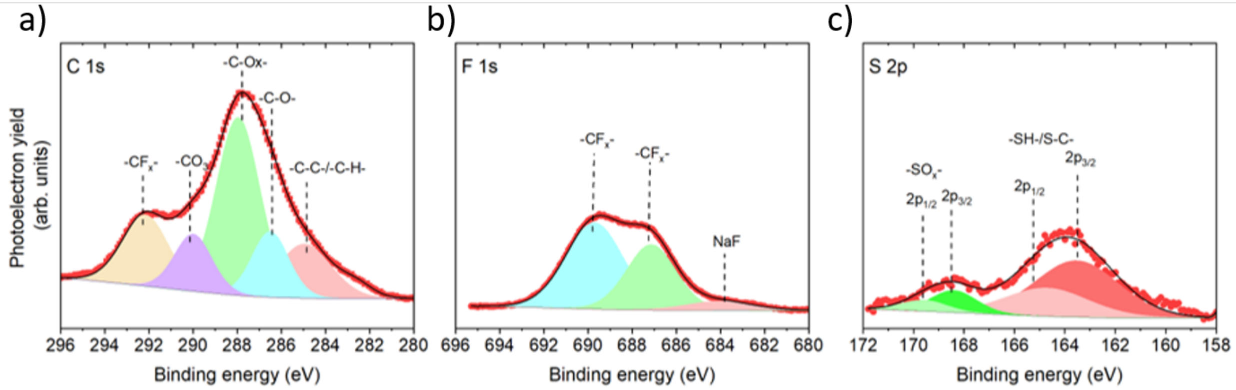

Figure 5.21: XPS analysis of NaSDCM-SIPE SEI. High-resolution a) C 1s, b) F 1s, and c) S 2p photoelectron regions.

5.3.5 Galvanostatic Cycling Performance

The NaSTFSI-based and NaSDCM-based SIPEs were used to realize proof-of-concept Na||SIPE|| PW cells, while the NaVBS-SIPE was excluded from subsequent experiments, considering it exhibits a low ionic conductivity and poor oxidation stability not being compatible with PW cathode material. The voltage profiles of Na||NaSTFSI-SIPE||PW (Figure 5.22a) cell show first cycle charge and discharge capacity of 144 and 141 mAh g^{-1} at 0.02C, respectively. Meanwhile, the Na||NaSDCM-SIPE||PW (Figure 5.22b) cell shows an initial charge and discharge capacity of 146 and 145 mAh g^{-1} at 0.02C, respectively. With both SIPEs, the cells exhibit two plateaus (more defined for the NaSDCM-SIPE-based cell) at 3.0 and 3.3 V vs. Na$^+$/Na. However, the cell containing NaSTFSI-SIPE shows higher polarization and lower specific capacity.

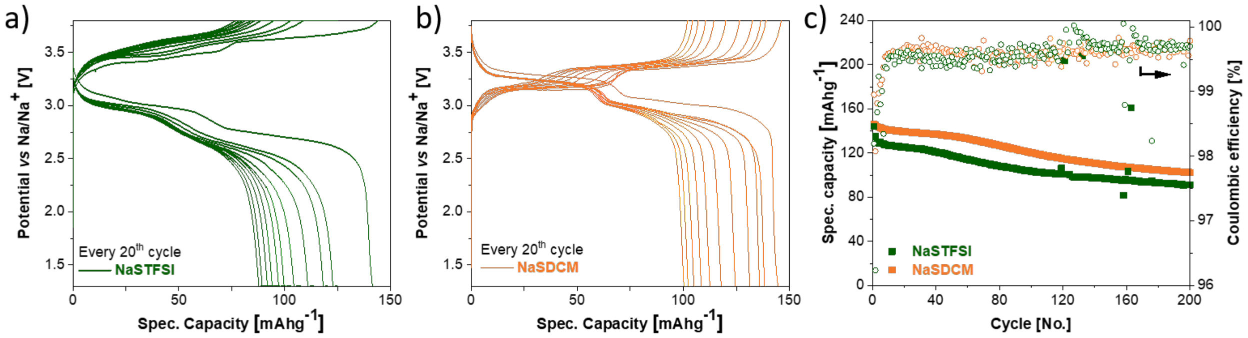

Figure 5.22: Voltage profiles of Na||SIPE||PW cells composed of a) NaSTFSI- and b) NaSDCM-SSMs and c) the corresponding specific capacity and Coulombic efficiency upon cycling. EC:DMC:FEC (49:49:2 vol.%) molecular transporter is incorporated into all SIPEs. The galvanostatic cycling test with a current density of C/50 the 1st cycle, followed by 5 cycles at C/20 and ongoing ones at C/10 between 3.8 V and 1.3 V. All measurements were performed at 40 °C.

The specific capacity of the cells decays when increasing the current from 0.02 C to 0.05 C and 0.1 C, independent of the used SIPE. The specific capacity of the cell with NaSTFSI-SIPE reaches 91 mAh g^{-1} after 200 cycles, while that employing NaSDCM-SIPE still delivers 102 mAh g^{-1} after 200 cycles (Figure 5.22c). Nonetheless, the average Coulombic efficiency is above 99% for both SIPEs, suggesting that both SIPEs can be considered good candidates to be implemented in the quasi-solid-state Na cells. The NaSTFSI-SIPE-containing cell shows a slightly higher initial capacity drop, as well as capacity jumps upon cycling, due to dendrite formations. However, a more stable initial capacity for the cells with NaSDCM-SIPE might be related to the formation of a more stable and/or thinner SEI compared to the NaSTFSI analog, which may be due to the absence of fluorine in the SSM that reduces the formation of NaF by reacting with sodium-metal.[153]

5.3.6 Conclusion on the Influence of the Anionic Center

Different anionic centers for SIPEs were investigated using either NaVBS, NaSTFSI or NaSDCM as SSM. The study revealed a strong correlation of lower dissociation energy (NaVBS>NaSTFSI >NaSDCM) with higher ionic conductivity (NaVBS<NaSTFSI<NASDCM). Additionally to the highest ionic conductivity, the NaSDCM-SIPE showed lower polarization and a slightly more stable cycling performance compared to the other two investigated SSMs. However, the NaSDCM-SIPE showed a lower thermal stability (250 °C instead of 300 °C), which was associated with the instability of the C-C=N bonds of the SSM. The comparison to the previously designed NaSTFSI-M4-SIPE showed that the ionic conductivity could be improved by ∼50% to $4.2{\cdot}10^{-5}\,\mathrm{S\,cm^{-1}}$ at RT and $2.9{\cdot}10^{-4}\mathrm{S\,cm^{-1}}$ at 90 °C. The cycling performance showed a capacity retention of 70% after 200 cycles, which is comparable (2% higher) to the previous NaSTFSI-M4-SIPE. The stronger anionic center might not be as beneficial for Na-based SIPEs as predicted for Li-based SIPEs.[95] Following, the ionic conductivity and the cycle performance might depend more on the polymer chain movement and the charge delocalization of the chain (directly connected to the anionic center) than the anionic center itself.

Chapter 5.4
Spacer Arm Variation in TFSI-based SIPEs

The spacer arm, which connects the anionic center to the polymer backbone, is crucial for the ionic conductivity of Na-based SIPEs. The ionic conductivity is expected to highly depend on the polymer chain movement, which can be modified by the flexibility of the spacer arm as well as the charge delocalization of the anionic center, which can be impacted by the chemical structure of the side chain. The anionic center of all SSMs in this chapter is TFSI-based, as this study was conducted in parallel with the previous chapter.

5.4.1 Chemical Structures of SSMs with Varying Spacer Arms

The influence of the spacer arm was investigated using the PET-4A/MP backbone with either NaSTFSI, NaMTFSI or NaFTFSI SSM.[164] The NaSTFSI SSM has a sterically demanding and rigid benzene ring as spacer arm, while the NaMTFSI SSM utilizes a flexible CH_2-based spacer arm. The NaFTFSI SSM also has a flexible spacer arm but the chain is CF_2-based to further delocalize the charge of the anionic center along the spacer arm (Figure 5.23). Noteworthy, the FTFSI SSM does not have a terminal double bond but a primary iodide instead. Iodides can be linked with the thiols of PETMP either by using a base as catalyst (nucleophilic substitution) or via a radical mechanism. The second uses the same conditions as the other SSMs, thus was used to connect the FTFSI SSM to the backbone with unchanged synthesize conditions.

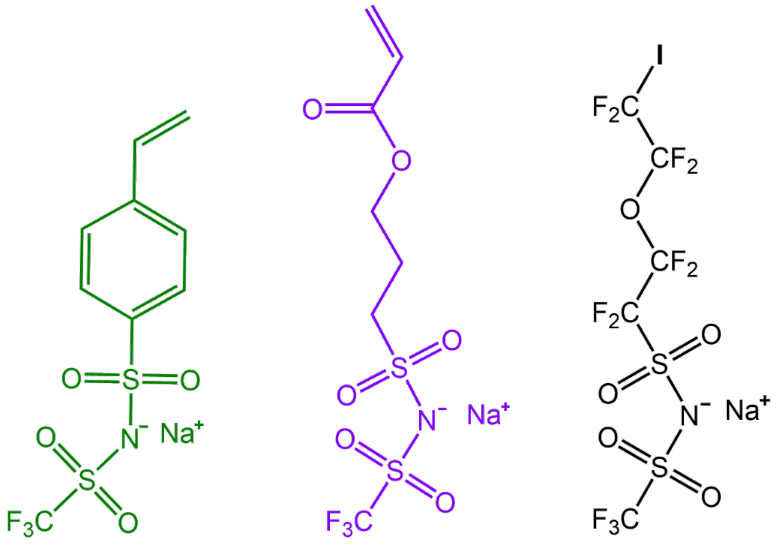

NaSTFSI **NaMTFSI** **NaFTFSI**

Figure 5.23: Chemical structure of the NaSTFSI, NaMTFSI and NaFTFSI SSMs.

5.4.2 Thermal and Electrochemical Properties

The thermal stability of all three dry SIPEs was assessed using TGA (Figure 5.25a) between 30 °C and 600 °C. The NaSTFSI- and NaFTFSI-based SIPE membranes show thermal stability up to 300 °C, while the NaMTFSI-based membrane shows thermal stability up to 270 °C. This poorer stability is due to the ester (R-(C=O)-O-R) group that exhibits easier bond breaking upon heating, compared to the benzene ring or the fluorinated alkyl chain ($-CF_2-CF_2-O-$).[153,165,166] The NaFTFSI-based SIPE shows an additional shoulder around 450 °C, showing that the NaFTFSI's decomposition takes in two different temperatures: at 300 °C corresponding to the backbone, and 450 °C due to the decomposition of the spacer arm, indicating that NaFTFSI's decomposition occurs at two distinct temperatures. The feature at 300 °C corresponds to the decomposition of the backbone, while that at 450 °C arises from the decomposition of the side chain. This indicates that the NaFTFSI SSM is even more thermally stable than the other two studied SSMs.

The phase transitions of the dried SIPEs were investigated using a DSC (Figure 5.25b) by scanning between -20 °C and 200 °C at a scan rate of 5 °C min^{-1}. All SIPEs show thermal stability up to 200 °C, confirming the results of the TGA scan. All SIPEs show a glass transition temperature (T_g) at 30 °C and an exothermic crystallization temperature (T_c) at 100 °C, matching the crystallization temperature of PVDF-HFP.[167]

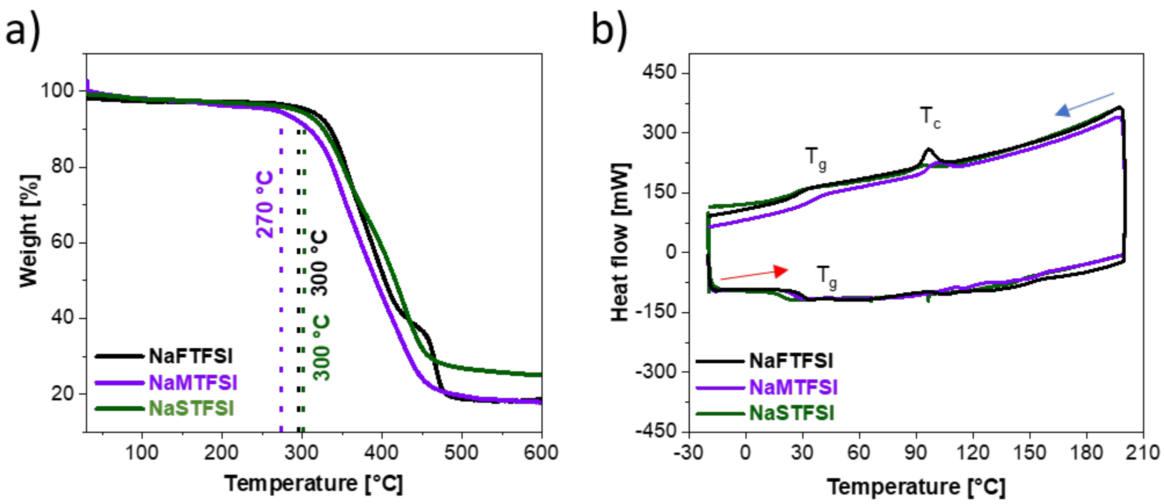

Figure 5.24: a) TGA and b) DSC (heating rate of 5 K min^{-1}, inert N_2 atmosphere for both experiments) of NaSTFSI- (black), NaMTFSI- (purple) and NaFTFSI (green)- dry SIPEs.

The SIPEs were soaked in EC:DMC:FEC (49:49:2 vol.%) solution, serving as a molecular transporter, at 60 °C for 48 hours prior to the ionic conductivity measurements. The uptake was determined to be 50 wt % of the final electrolyte membrane by differential weighing. The ionic conductivity measurements were performed between 10 °C and 90 °C (Figure 5.25a), starting from 20 °C and step-wise reaching 90 °C (increasing 10 °C per step) followed by a step-wise cooling to 10 °C. The results reveal that the ionic conductivity increases with increasing temperature, showing the Vogel-Tamman-Fulcher (VTF, see Fig. S8.4 for comparison with ln() vs. 1000/T plot) behavior typically observed for other Li- and Na-based SIPEs.[142,158] The NaSTFSI delivers the lowest ionic conductivity of $2.8{\cdot}10^{-5}$ S cm^{-1} at RT ($2.2{\cdot}10^{-4}$ S cm^{-1} at 90 °C), followed by NaMTFSI, which reaches $7.9{\cdot}10^{-5}$ S cm^{-1} at RT ($4.5{\cdot}10^{-4}$ S cm^{-1} at 90 °C) and NaFTFSI with ionic conductivity of $2.7{\cdot}10^{-4}$ S cm^{-1} at RT ($1.1{\cdot}10^{-3}$ S cm^{-1} at 90 °C). The lowest ionic conductivity of NaSTFSI-SIPE is related to the shorter and immobile benzene spacer arm, which hinders the movement of the anionic center. Meanwhile, NaMTFSI-SIPE has a similar chain length but a more flexible arm, facilitating the sodium ion carrier. The ionic conductivity improves even more for the fluorinated NaFTFSI-SIPE due to the slightly larger length and the presence of the fluor atoms, which draw and delocalize the negative charge across the whole SSM rather than just in the anionic center.

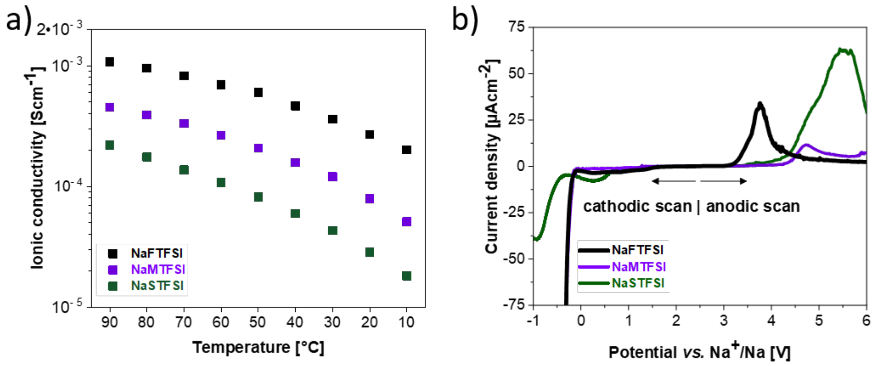

Figure 5.25: a) Temperature-dependent ionic conductivity and b) electrochemical stability window (Na||SIPE||Al, scan rate of 30 µV s^{-1} at 40 °C) of NaSTFSI-, NaMTFSI- and NaFTFSI-based SIPEs containing the EC:DMC:FEC molecular transporter.

The electrochemical stability window was investigated by LSV (Figure 5.25b). The NaMTFSI- and NaSTFSI-SIPE exhibited a good electrochemical stability between 0 (i.e., prior Na plating) and 4.2 V vs. Na$^+$/Na (threshold for the voltage onset was 25 µA cm^{-2}). In comparison, the NaFTFSI-SIPE exhibited a lower oxidation stability, as indicated by the peak around 3.5 V. The lower value of the oxidation threshold voltage may be related to the oxidation of the fluorine-rich spacer arm and side reactions, resulting in the formation a passivation layer.[104] However, such a low oxidation stability suggests NaFTFSI-SIPE not to be an appropriate SIPE for PW cathode-based cells, since the upper cut-off of PW is around 4.0 V vs. Na$^+$/Na. Regarding cathodic stability, NaMTFSI- and NaFTSI-SIPEs exhibited a more rapid current increase below 0 V compared to NaSTFSI-SIPE, indicating lower polarization and good compatibility with Na metal due to the rapid Na deposition. Summarizing the anodic and cathodic scan results, NaMTFSI-SIPE appears to be the most appropriate electrolyte for application in full-cells.

However, to further investigate the plating/stripping behavior of SIPEs, additional symmetric cells (Na||SIPE||Na) were tested with current densities between 10 and 50 µA cm^{-2} (Figure 5.26). The overpotential of all SIPEs increases with increasing current density, resulting in a final overpotential of 0.52 V for the NaSTFSI-SIPE (Figure 5.26a), 0.21 V for the NaMTFSI-SIPE (Figure 5.26c) and 0.18 V for the NaFTFSI-SIPE (Figure 5.26e). The interfacial resistance evolution upon cycling was studied using EIS. The interfacial resistance is slightly decreasing for the NaMTFSI-SIPE with increasing current density, suggesting the homogenization of the SEI. The interfacial resistance of the NaFTFSI-SIPE is rather stable at first but increases during long-term cycling, suggesting that the NaFTFSI-SIPE is not suitable for long-term cycling. The interfacial resistance of the NaSTFSI-SIPE shows an increase upon cycling at first, suggesting ongoing SEI formation in the first cycles, which stabilizes upon long-term cycling. This slow formation of a stable SEI suggests that the NaSTFSI-SIPE has slower kinetics compared to the other two SIPEs in alignment with the ionic conductivity trend. The interfacial resistance after long-term cycling stabilizes around 15 kΩ for the NaSTFSI-SIPE (Figure 5.26b)and 3.5 kΩ for the NaMTFSI-SIPE (Figure 5.26d), while the interfacial resistance of 2.5 kΩ for the NaFTFSI-SIPE (Figure 5.26f) starts to increase upon prolonged cycling. The small increase might be related to the fact that the –CF_2 groups may undergo dehydrofluorination, yielding the formation of a NaF-rich SEI, as observed with NaSTFSI-SIPE, but resulting into a loss of the initial properties, such as ionic conductivity, thereby increasing the interfacial resistance. The low interfacial resistance of the NaMTFSI-SIPE suggests the formation of a good ionic conducting SEI and promising long-term cycling stability.

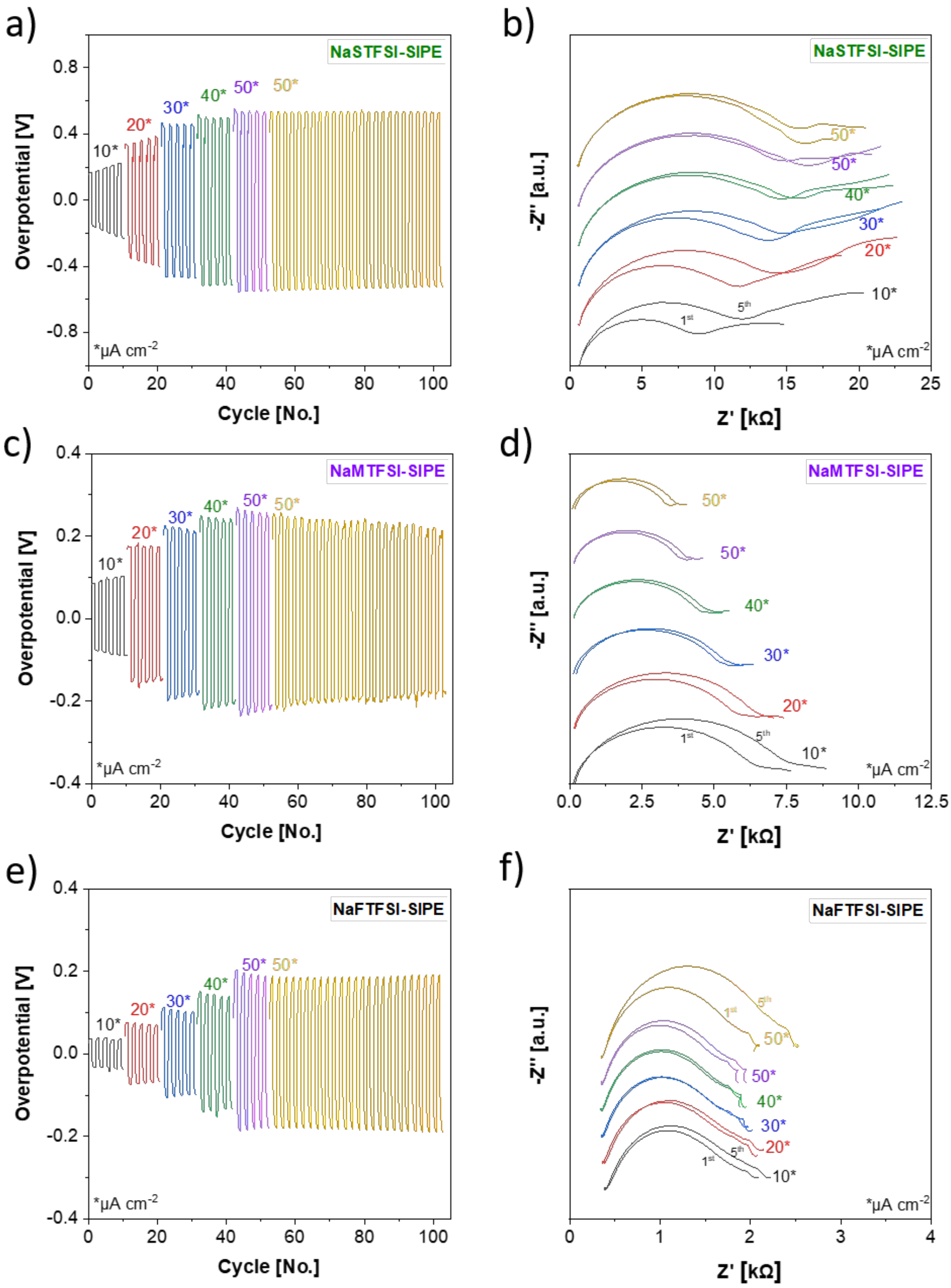

Figure 5.26: Na stripping/plating tests at different current densities at 40 °C using a) NaSTFSI-, c) NaMTFSI-, and e) NaFTFSI-SIPEs together with the corresponding Nyquist plot of b) NaSTFSI-, d) NaMTFSI- and f) NaFTFSI-SIPE after the 1st and 5th cycle at each current density: 10 µA cm^2 – black, 20 µA cm^2 – red, 30 µA cm^2 – blue, 40 µA cm^2 – green and 50 µA cm^2 – purple, as well as after 1st and 5th in the long-term cycling at 50 µA cm^2 – yellow. Additionally, 50 wt.% of EC:DMC:FEC (49:49:2 vol.%) molecular transporter were incorporated into all SIPEs.

5.4.3 Spacer Arm Dependent Cycling Performance

The electrochemical performance in quasi-solid-state Na||SIPE||PW cells was also investigated. The cells employing NaSTFSI- (Figure 5.27a) and NaFTFSI-SIPEs (Figure 5.27b) exhibited high polarization. Meanwhile, the NaMTFSI-SIPE based-cell (Figure 5.27c) showed lower polarization, clearly displaying the two characteristics plateaus of PW at 3.0 and 3.3 V vs. Na^+/Na, in line with the lower polarization visible during stripping/plating.[153] The Na||PW cell tested with NaSTFSI-SIPE delivers an initial charge and discharge capacity of 144 and 141 mAh g^{-1}, the NaFTFSI-SIPE-based cell 172 and 148 mAh g^{-1} and the NaMTFSI-SIPE-based cell 155 and 142 mAh g^{-1}, respectively. The high irreversibility of PW in NaFTFSI-SIPE is certainly related to SIPE oxidation, as indicated by LSV and confirmed by the charge capacity being greater than the theoretical one.

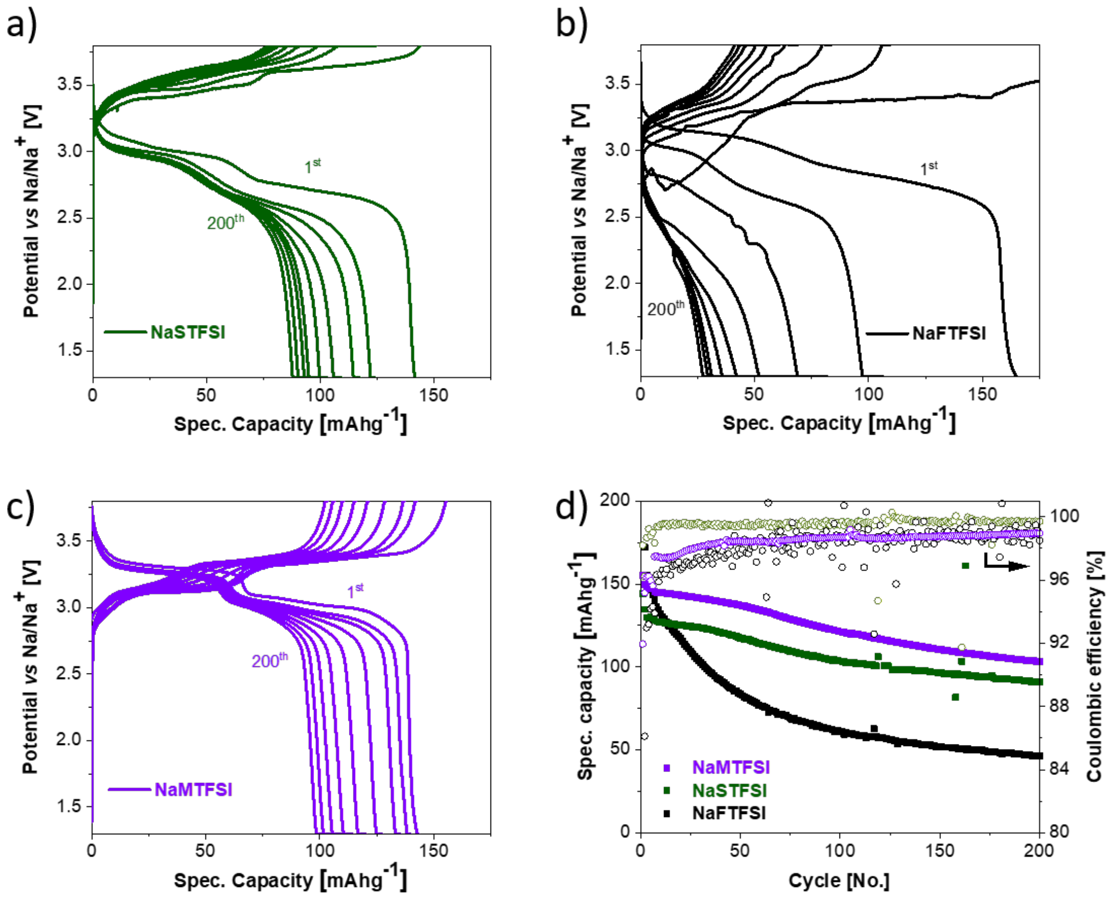

Figure 5.27: Voltage profile of Na||PW cells using a) NaSTFSI-, b) NaFTFSI- or c) NaMTFSI-SIPEs, and the corresponding d) specific capacity and Coulombic efficiency. In all SIPEs EC:DMC:FEC (49:49:2 vol.%) molecular transporter is incorporated. The galvanostatic cycling tests are carried out at a current density of C/50 the 1st cycle, followed by 5 cycles at C/20 and ongoing ones at C/10 between 3.8 V and 1.3 V. All measurements are performed at 40 °C.

The long-term stability of the cells was also investigated (Figure 5.27d). The Na||NaMTFSI-SIPE||PW cell delivered the highest capacity and exhibited the best cycling stability, in agreement with the higher stability against sodium-metal observed in the stripping/plating test and the excellent oxidation stability observed *via* LSV. Indeed, the Na||NaMTFSI-SIPE||PW cell showed a capacity retention of 72%, followed by Na||NaSTFSI-SIPE||PW (70%) and Na||NaFTFSI-SIPE||PW (31%) cells after 200 cycles. With regard to Coulombic efficiency, the NaFTFSI-SIPE-based PW cell delivered low and fluctuating values, due to the SIPE decomposition reactions described above. However, the Coulombic efficiency of the cell based on NaSTFSI-SIPE went above 99% after a few cycles (ICE = 98%). On the other hand, the NaMTFSI-SIPE-based cells delivered initially low Coulombic efficiency (<97%), suggesting the occurrence of decomposition reaction(s). This may be attributed to the ester splitting reaction of the methacrylate side chain spacer, induced by the high proton content, together with a high fluorine content near the Na metal anode.

5.4.4 Conclusion on the Spacer Arm Investigation

The influence of the spacer arm on NaSTFSI, NaMTFSI or NaFTFSI SSM has been investigated. Results showed that the flexible and fluorinated NaFTFSI SSM, although it exhibited the highest ionic conductivity, largely suffered from decomposition reactions with sodium-metal, leading to poor cycling stability. On the contrary, the NaMTFSI-SIPE showed an improved ionic conductivity of $7.9 \cdot 10^{-5}$ S cm^{-1} at RT (+88% compared to the NaSDCM-SIPE) and $4.5 \cdot 10^{-4}$ S cm^{-1} at 90 °C (+55% compared to the NaSDCM-SIPE) and a comparable (2% higher) capacity retention of 72% (103 mAhg^{-1}) in Na||PW cells after 200 cycles at 0.1C. The strong improvement of the ionic conductivity confirmed that the polymer chain movement and the charge delocalization are essential for Na ion conduction and might be even more important for Na-based SIPEs than for Li-based SIPEs. However, the ionic conductivity and the cycling performance might still be limited by the mismatch between the size of the Na ions compared to the size of the polymer matrix.

Chapter 5.5
Investigation of Different Backbones with NaMTFSI as SSM

The backbone structure and chemistry of the polymer membrane are expected to influence the thermal, mechanical and electrochemical properties of the SIPEs. Thus, the influence of the backbone was investigated using the most promising NaMTFSI SSM studied in chapter 5.4, with four different polymer backbones to determine the influence of the polymer matrix on the properties of the SIPEs, especially the influence on the Na ion conductivity.

5.5.1 Chemical Structures of Different Polymer Backbone Monomers

The different polymer backbones investigated in this chapter are all PETMP-based with either diene, trione, PET4A, or PET6A as copolymerizing backbone component (Figure 5.28). The obtained backbone structures are blended with PVDF-HFP and incorporated with 50 wt.% of molecular transporter (EC:DMC:FEC) and are labeled by the varied backbone components as diene-, trione-, PET4A- and PET6A-SIPE, respectively. The main difference among the various backbone monomers is the amount of functional vinyl groups that they provide per molecule. Diene, trione, PET4A, and PET6A have, respectively, 2, 3, 4, and 6 functional groups. A higher amount of vinyl groups is expected to create more cross-linking bridges in the resulting SIPE that means the diene-SIPE is expected to have the lowest degree of cross-linking and the PET6A-SIPE the highest. This would enable us to fabricate SIPEs with various networks, offering different mechanical and electrochemical properties. For example, it is expected that the PET6A will provide higher mechanical properties due to its high cross-link degree. However, the formated cavities might be small enough to hinder Na^+ transport. Therefore, a deep characterization is conducted and shown below to understand the influence of the backbone components on the SIPE properties.

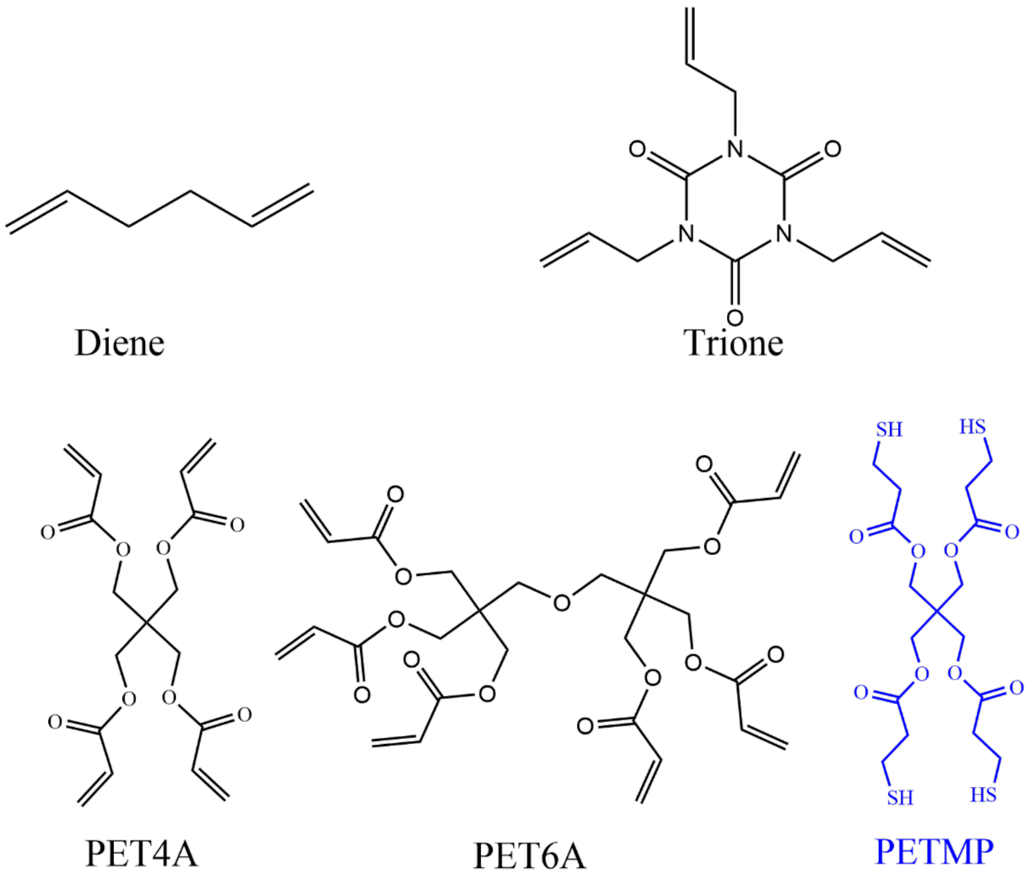

Figure 5.28: Structure of the monomers that were used to synthesize the diene-, trione-, PET4A- and PET6A-based SIPEs that build up the polymer backbone together with PETMP (in blue).

5.5.2 Mechanical Properties of SIPEs with Different Backbone Monomers

The mechanical properties of the different cross-linked SIPEs were investigated using dry and PVDF-HFP-free SIPEs for a direct comparison. The SIPEs are exposed to strain, while measuring the stress until failure (Figure 5.29a). In addition, the maximum elongation that the SIPEs can hold before breaking is illustrated in Figure 5.29b. The diene- and trione-SIPE are rigid, not showing a linear elastic region that follows Hooke's law of elastic deformation in the stress-strain curves, indicating that an increased force does not proportionally extend the polymer. Instead, these two SIPEs directly enter the strain hardening region upon elongation, exhibiting the lowest elongation values of 15% and 30% for diene-SIPE and trione-SIPE, respectively. In the case of diene-SIPE, it contains only two functional groups, i.e., two cross-link sites, and thus, the binding strength inside the polymer backbone is not as strong as for the other SIPEs.

Additionally, the diene molecule is rather rigid and cannot adjust to an increasing amount of stress, resulting in a lower maximum strain value. Although the trione-SIPE has an additional functional group providing additional mechanical stability, the molecule itself is also rigid and not-flexible, thus also breaks rather easily when strain is applied.

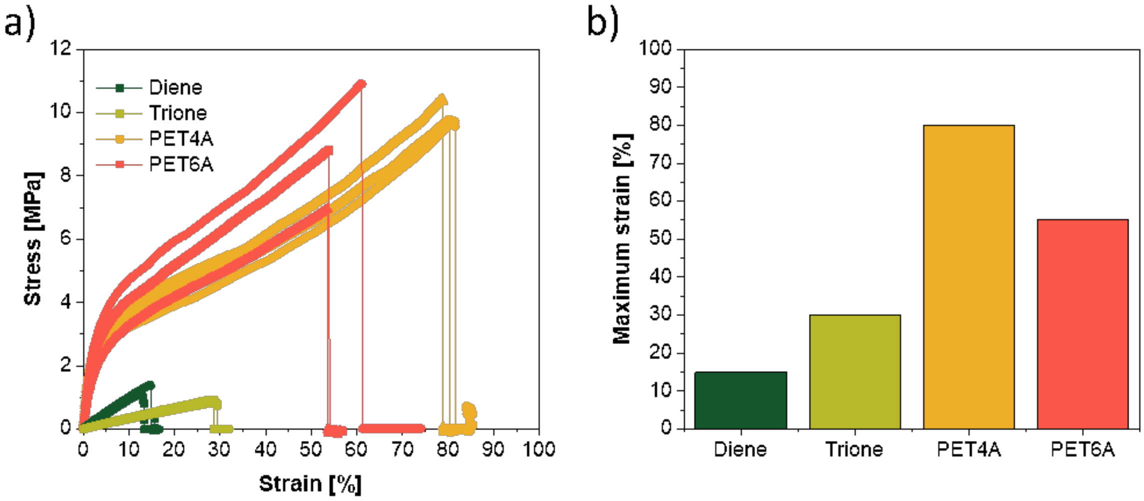

Figure 5.29: a) The measured stress-strain curve and b) the maximum strain before breaking of the diene-, trione-, PET4A- and PET6A-SIPEs. The tests were performed on neat SIPEs, i.e., without PVDF-HFP and molecular transporter, at RT.

On the other hand, both PET4A-SIPE and PET6A-SIPEs exhibited a linear elastic deformation at the beginning of the stress-strain curves and high strain resistance, exceeding 50%, as both molecules are more flexible and contain more functional groups, allowing for the production of a densely crosslinked SIPE structure. Noteworthy, the PET6A-SIPE exhibits 55% as maximum strain, while PET4A-SIPE reaches 80%. The better mechanical properties of PET4A-SIPE can be explained through the chemical structure. The PET6A molecule features an ether bond in the middle of its structure, connecting both sides of the molecules (see Figure 5.28). This ether bond breaks, generating an oxygen radical and a tertiary carbon radial, which are both stable intermediate states.[168–170] Thus, the PET6A molecule could break more easily compared to the "core" of PET4A, which is based on four carbon-carbon bonds. In summary, the PET4A-SIPE exhibits the highest strain resistance, as PET4A provides the most flexible backbone monomer among the tested SIPEs and has a stable "core" in the middle of its structure.

5.5.3 Thermal Stability of SIPEs with Different Backbones

The thermal stability of the dry diene-, trione-, PET4A-, and PET6A-based SIPEs blended with PVDF-HFP was investigated by TGA up to 600 °C (Figure 5.30a). All SIPEs show thermal stability up to 270 °C, *i.e.*, less than 5% weight loss, indicating that the backbone component had no significant influence on the thermal properties. The diene-SIPE showed a slightly sharper mass loss right after passing the decomposition temperature, i.e., a higher decomposition rate, due to the lowest amount of cross-linking bonds in the backbone structure.

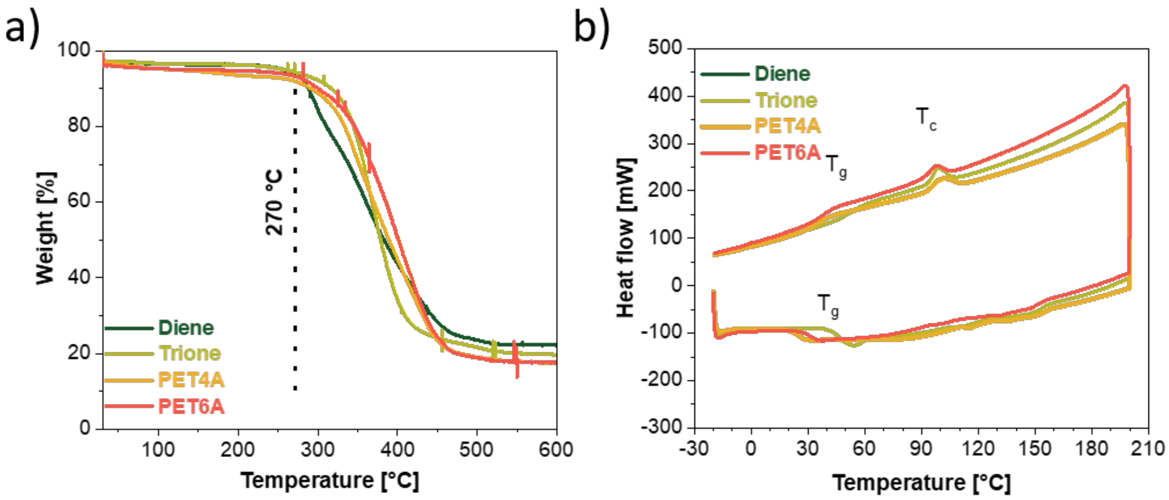

Figure 5.30: a) TGA and b) DSC of dry diene-, trione-, PET4A- and PET6A-based SIPEs (heating rate of 5 K min^{-1}, inert N_2 atmosphere, the DSC was performed by two cooling and heating cycles between -20 and 200 °C).

In addition, DSC measurements were performed from -20 °C up to 200 °C and back to -20 °C. The DSC scans (Figure 5.30b) showed a glass transition peak (T_g) between 30 and 50 °C and a crystallization peak (T_c) around 100 °C for all SIPEs, without significant differences among them.

5.5.4 Small and Wide Angle X-ray Scattering

The small and wide angle X-ray scattering (SWAXS) patterns of PVDF-HFP free and PVDF-HFP blended SIPE composed of either diene-, trione-, PET4A- or PET6A-based backbones were recorded. Additionally, the SWAXS pattern of a neat PVDF-HFP membrane and commercially available PVDF has been measured as a reference (Figure 5.31). The WAXS pattern of PVDF powder displays the typical Bragg peaks of crystalline PVDF at q-values 1.15 Å^{-1}, 1.28 Å^{-1}, 1.81 Å^{-1} and 2.66 Å^{-1},[171,172] indicating a semi-crystalline structure. Meanwhile, the PVDF-HFP copolymerization led to a significant amorphization for both the powder and the membrane, as suggested by the peak intensity decrease and broadening, coupled with the appearance of a broad halo and a complete intensity loss at 1.81 Å^{-1}.[173]

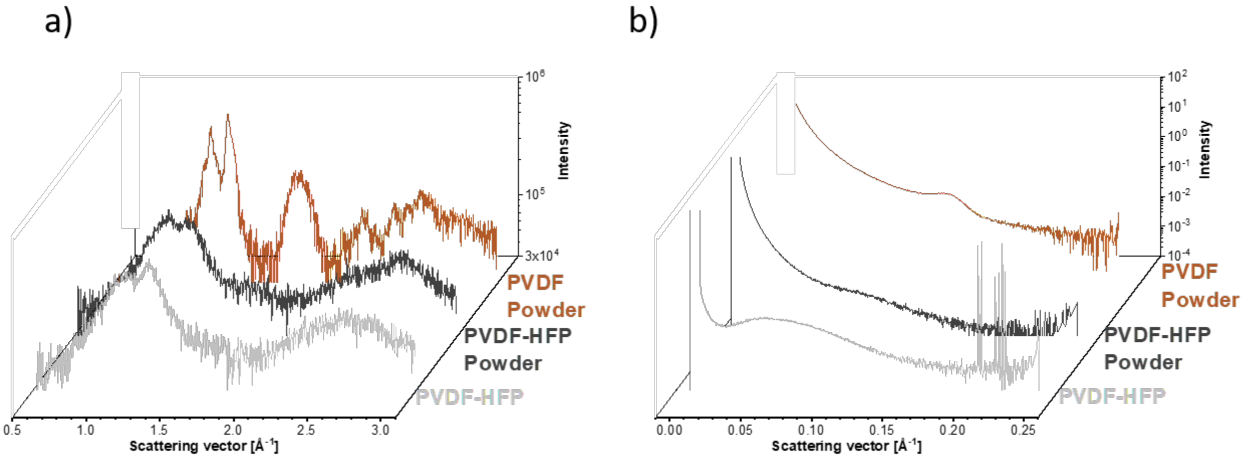

Figure 5.31: a) WAXS and b) SAXS pattern of commercial PVDF powder, PVDF-HFP powder and a pure PVDF-HFP membrane.

Further information about the structure was obtained by comparing the SAXS patterns. The PVDF powder showed a slightly visible peak at 0.135 Å^{-1}, while no clear peak was seen for the PVDF-HFP powder, which is in good agreement with the more amorphous structure of the latter, as observed *via* WAXS. The change in intensity and q values from PVDF to PVDF-HFP suggests that the copolymerization with HFP results in a decrease of the crystallinity and an increase of the average distance between the lamellar domains. However, once PVDF-HFP is cast as a membrane, a broad peak emerges at 0.07 Å^{-1}, indicating that the casting process facilitates a more pronounced orientation.

SIPEs composed of the four polymer backbones (*i.e.*, diene-, trione, PET4A or PET6A) were analyzed with and without PVDF-HFP (Figure 5.32) to identify the structural properties of the backbone alone and in the realistic setup with PVDF-HFP. All investigated PVDF-HFP-free membranes exhibited a broad peak between 0.5 and 1.5 Å^{-1} in the WAXS pattern (Figure 5.32a), a characteristic typically observed in amorphous polymers. In fact, the SAXS patterns (Figure 5.32b) are in agreement with the WAXS pattern, displaying no sharp peaks, which suggests a random orientation of the polymer over long distances and confirming the rather amorphous polymer structure.

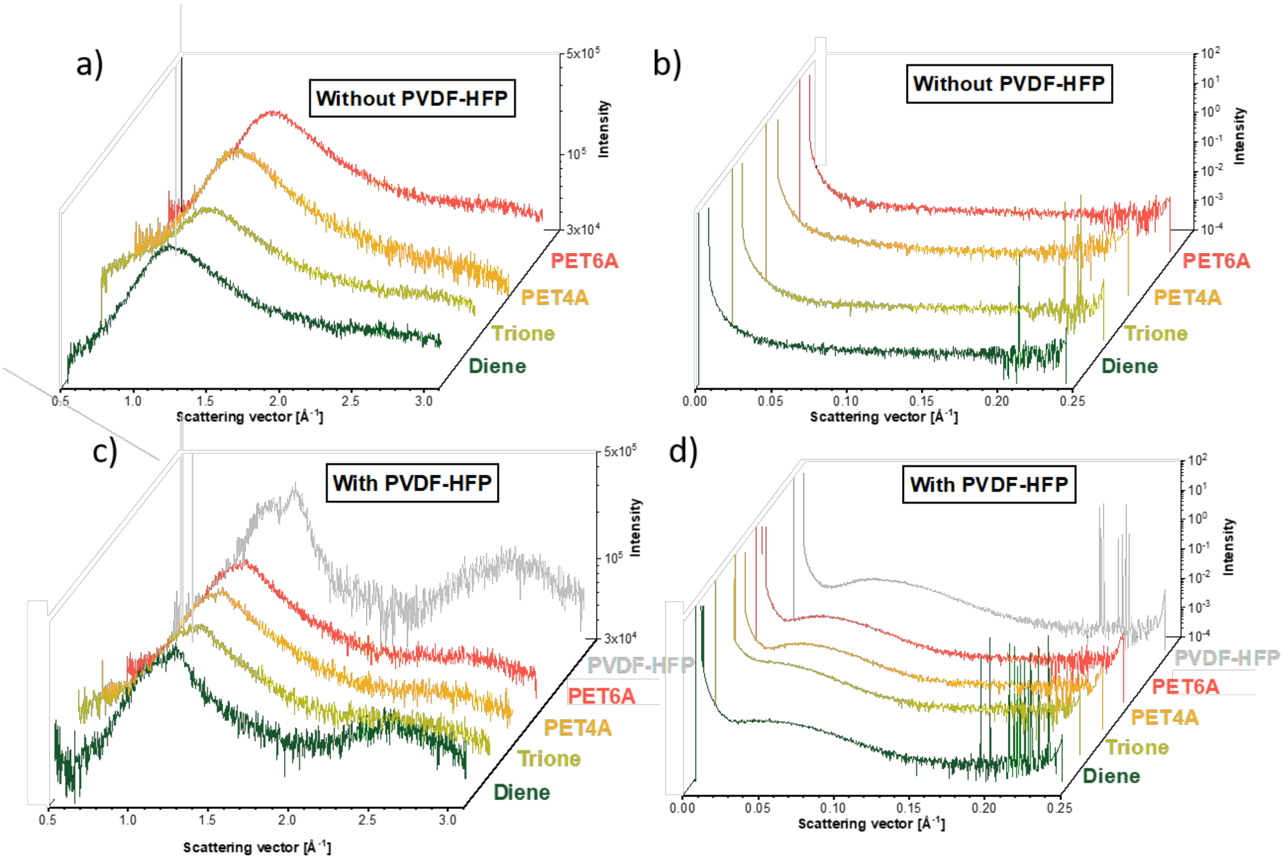

Figure 5.32: a) WAXS and b) SAXS patterns of the diene-, trione-, PET4A- and PET6A-based SIPEs without PVDF-HFP and with PVDF-HFP (c) and d), respectively).

The WAXS patterns of SIPEs blended with 20% PVDF-HFP (Figure 5.32c) exhibited similarities with those of PVDF-HFP-free, such as a broad peak between 0.5 and 1.5 Å^{-1}, which is characteristic for amorphous structures. In fact, the peak at 2.7 Å^{-1} displayed by PVDF-HFP was not observed for the SIPE membranes, except for the diene-SIPE, suggesting either larger pores or higher flexibility of the membranes.[171] Regarding the SAXS patterns (Figure 5.32d), all SIPEs and neat PVDF-HFP membranes showed a broad peak around 0.06-0.08 Å^{-1}, which is characteristic of the long-distance repeating unit of PVDF-HFP. However, the broad peak that pure PVDF-HFP shows at 0.08 Å^{-1} was shifted towards 0.06 Å^{-1} for SIPEs. The peak shift towards smaller q values suggests that the distance between the vinylidene fluoride units increased once included in the polymer network, not forming subclusters, but rather being homogeneously incorporated into the SIPE network.

Additional insights into the SIPE structure were obtained from density measurements (Figure 5.33a), which ranged from 0.7 g cm^{-3} to 1.2 g cm^{-3}. The density increased with the addition of functional groups, except for diene-SIPE, which exhibited a higher density than trione-SIPE despite having fewer crosslinks. This suggests for the least crosslinked structure formed a denser polymer backbone structure, presumably due to the reduced size of the flexible diene molecule.

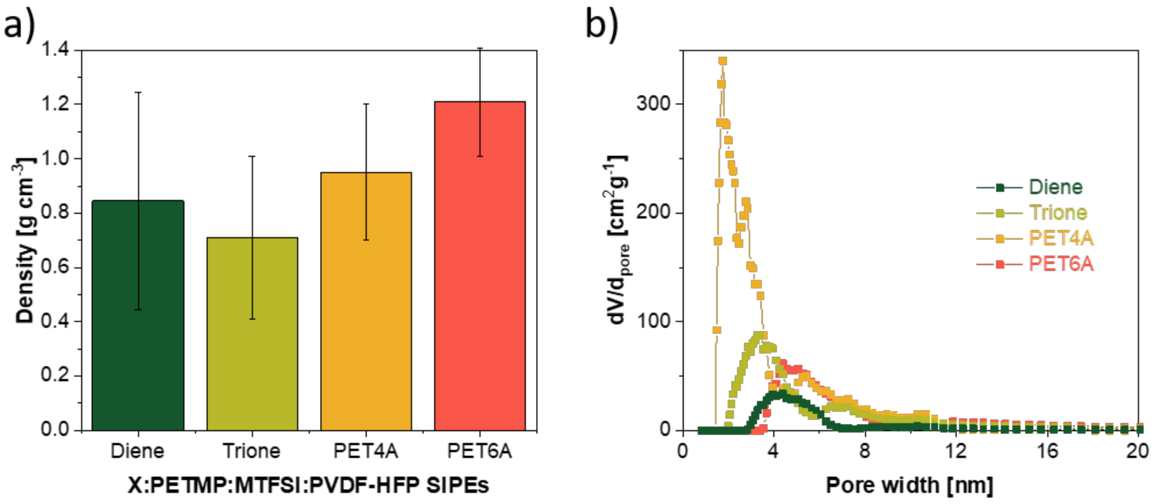

Figure 5.33: a) Density and b) calculated pore size of the diene-, trione-, PET4A- and PET6A-based SIPEs blended with PVDF-HFP. The dry membranes' patterns were collected at RT.

The intrinsic porosity and the pore size distribution was assessed by physical adsorption using the Brunauer-Emmet-Teller (BET) method. The Ar isotherms were measured for all SIPEs (Figure 8.5) and the pore size distribution was analyzed (Figure 5.33b), revealing pore sizes ranging from 2 and 8 nm. The diene-SIPE exhibited a pore distribution between 3 and 6 nm. The trione-SIPE, on the other hand, exhibited two distinct pore sizes: one ranging from 3 to 5 nm and another from 6 and 8. The PET4A-SIPE displayed the smallest pores sizes (between 1 and 4 nm) with a lower content of pore sizes of 5 – 8 nm. Lastly, the PET6A-SIPE exhibited a pore size ranging from 4 to 8 nm. In summary, the trione-SIPE with the lowest density exhibited the largest pores, confirming its high porosity, i.e., low density, which is likely due to the rigid structure. The PET4A- and trione-based SIPEs also featured pores with a size below 4 nm. This second type of pores could originate from interlocking chains between the same molecules, forming a closed ring rather than a network with multiple bonding partners and thus creating a second type of cavity with a different pore width. The absence of this second peak for the diene- and PET6A-based SIPEs can be explained as the diene molecule is hindered from forming closed rings due to the low number and wide spacing of its functional groups. The BET results align with the density and SWAXS measurements, confirming the differences in the porous structures of the various backbones.

5.5.5 Conductivity and Electrochemical Stability Window

The SIPEs were soaked with the EC:DMC:FEC (49:49:2 vol.%) molecular transporter, and their ionic conductivity was measured (Figure 5.34a). As expected, the SIPEs' conductivity increased with temperature and exhibited the VTF behavior, typical of polymeric ion conductors. Comparing the ionic conductivity among the four SIPEs, the diene- and trione-SIPEs displayed slightly higher values at all measured temperatures (ionic conductivity of $1.8\cdot10^{-4}$ S cm^{-1} at RT and $6.0\cdot10^{-4}$ S cm^{-1} at 90 °C) compared to PET4A- and PET6A-SIPEs (ionic conductivity of $7.9\cdot10^{-5}$ S cm^{-1} at RT and $4.5\cdot10^{-4}$ S cm^{-1} at 90 °C). The ionic conductivity results indicated that a lower amount of cross-linking and lower density promote faster ion transport throughout the membrane (PET6A/PET4A<Trione/Diene).

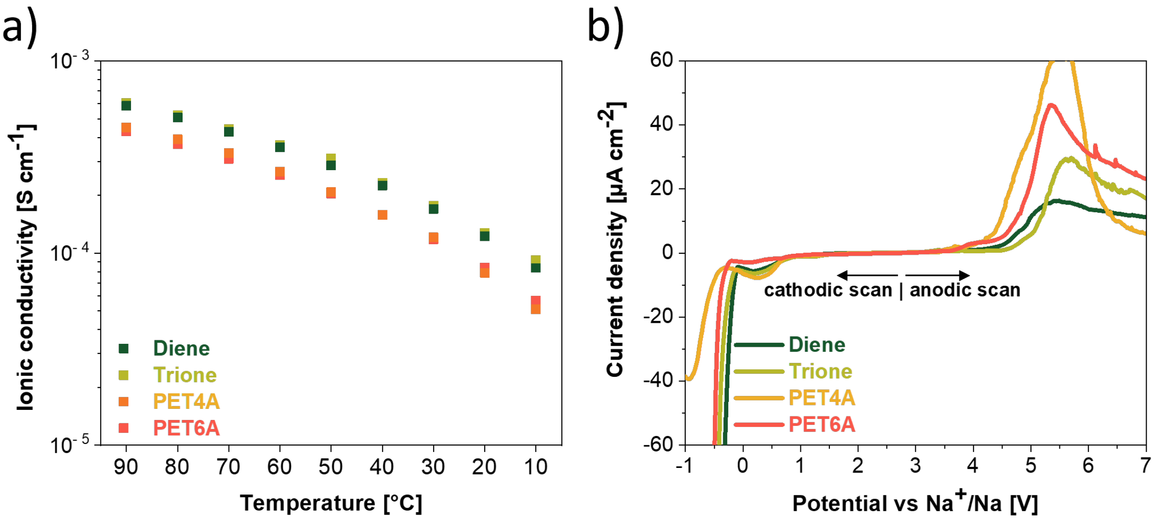

Figure 5.34: a) Temperature-dependent ionic conductivity, and b) electrochemical stability window (Al||SIPE||Na, scan rate of 30 µV s^{-1}, temperature 40 °C) of the diene-, trione-, PET4A- and PET6A-based SIPEs containing 50 wt.% of molecular transporter (EC:DMC:FEC).

The electrochemical stability window of the SIPEs was measured using Al||SIPE||Na cells (Figure 5.34b). The cathodic stability showed no electrochemical limitation prior to sodium-metal plating at 0 V vs. Na$^+$/Na, except for a very small reduction peak at 0.4 V, attributed to the decomposition of EC, DMC and/or FEC. Meanwhile, the anodic scan shows excellent stability (above 4 V vs. Na^+/Na, considering the threshold for the voltage onset >25 µA cm^{-2}) for all SIPEs.

5.5.6 Cycling Performance of the SIPEs with different Backbones

The SIPEs were then used as electrolytes in quasi-solid-state Na||SIPE||PW cells. The cell voltage profiles (Figure 5.35) exhibited the characteristic plateaus at approximately 3.0 and 3.3 V vs. Na^+/Na, regardless of the backbone structure. The initial charge and discharge capacities of the cells were 188 and 184 mAh g^{-1} (97%) for the diene-SIPE-based cells, 186 and 176 mAh g^{-1} (94%) for the trione-SIPE, 155 and 143 mAh g^{-1} (92%) for the PET4A-SIPE and 167 and 159 mAh g^{-1} (95%) for the PET6A-SIPE. The initial charge capacity of all cells was higher than the theoretical capacity of PW, suggesting that some side reactions affecting the electrolyte occur at the PW and/or sodium-metal electrodes. The diene- and trione-SIPE exhibited a higher initial specific capacity due to the higher ionic mobility, which reduced the cell polarization..[174] This resulted in a longer first plateau of 86 and 82 mAh g^{-1} for the diene- and trione-based SIPEs, respectively, while the PET4A- and PET6A-based SIPEs cells delivered 65 and 67 mAh g^{-1}, respectively. The initial Coulombic efficiency was comparable for all SIPEs, e.g., 97%, 94%, 92%, and 95% for diene-, trione-, PET4A, and PET6A, respectively, suggesting that the choice of backbone monomer slightly influenced SEI and CEI formation.

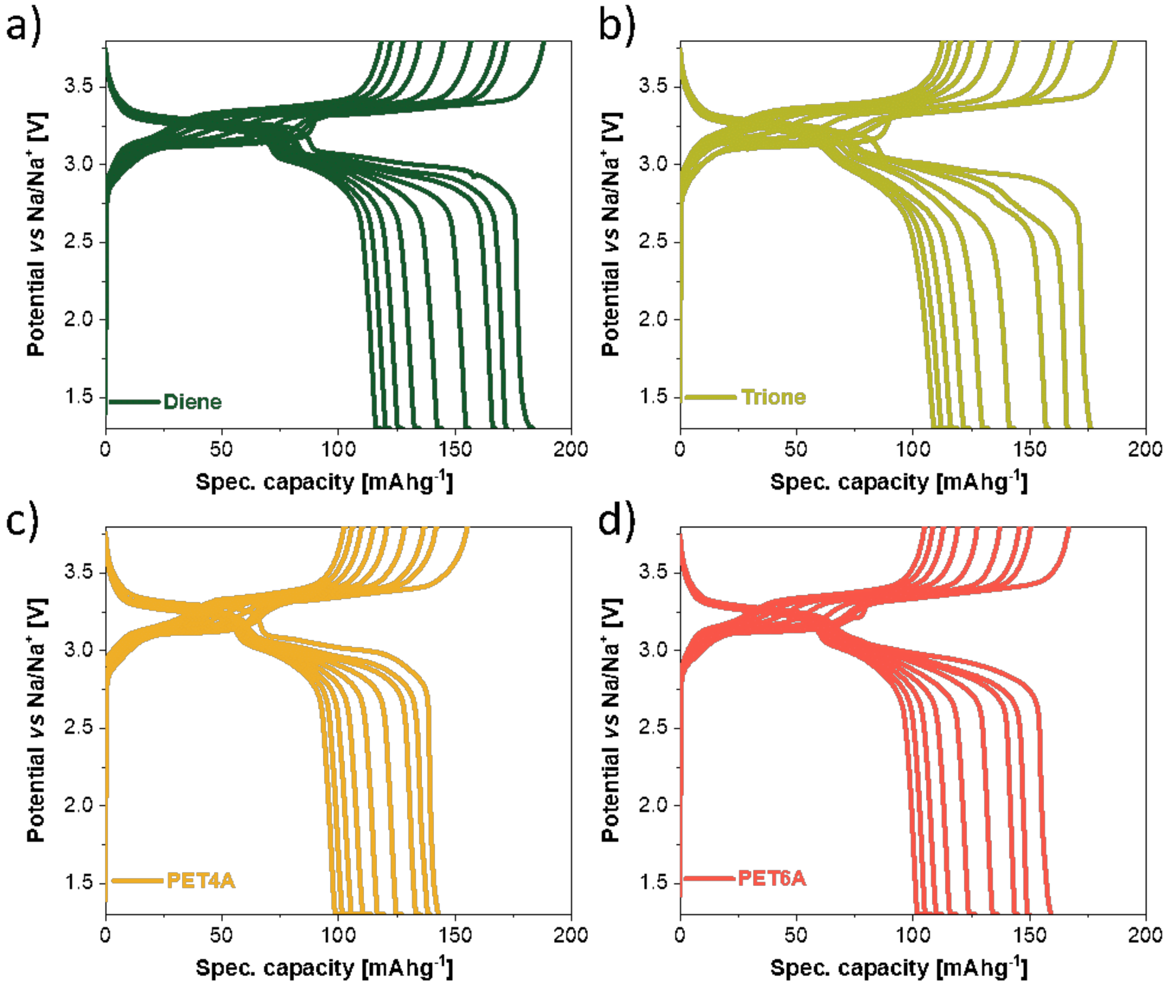

Figure 5.35: Voltage profile of the Na||SIPE||PW cells, containing a) diene-, b) trione-, c) PET4A- and d) PET6A-SIPE. The galvanostatic cycling tests are performed at C/50 (1st cycle), followed by at C/20 (5 cycles) and C/10 until failure between 3.8 V and 1.3 V. All measurements were performed at 40 °C. The SIPE contains 50 wt.% of EC:DMC:FEC.

Furthermore, the discharge capacity and Coulombic efficiency upon prolonged cycling are illustrated in figure 5.36. The capacity after 200 cycles was 119 mAh g^{-1} for the diene-SIPE, 113 mAh g^{-1} for the trione-SIPE, 103 mAh g^{-1} for the PET4A-SIPE and 105 mAh g^{-1} for the PET6A-SIPE based cells, with corresponding capacity retention rates of 68%, 66%, 73%, and 68%, respectively. The low Coulombic efficiency of the PET4A-SIPE upon cycling suggests that the close-knit network of the PET4A-SIPE results in a stiff membrane, thereby reducing contact with the electrodes compared to other SIPEs, which may lead to limited discharge and lower Coulombic efficiency. The diene-based SIPE offered slightly better ion transport compared to all other tested SIPEs. Still, it also exhibited the weakest mechanical stability, which may be related to its more pronounced capacity fading. Meanwhile, the PET4A- and PET6A-SIPE offer higher mechanical stability, but slightly lower ionic conductivity and cycling performance.

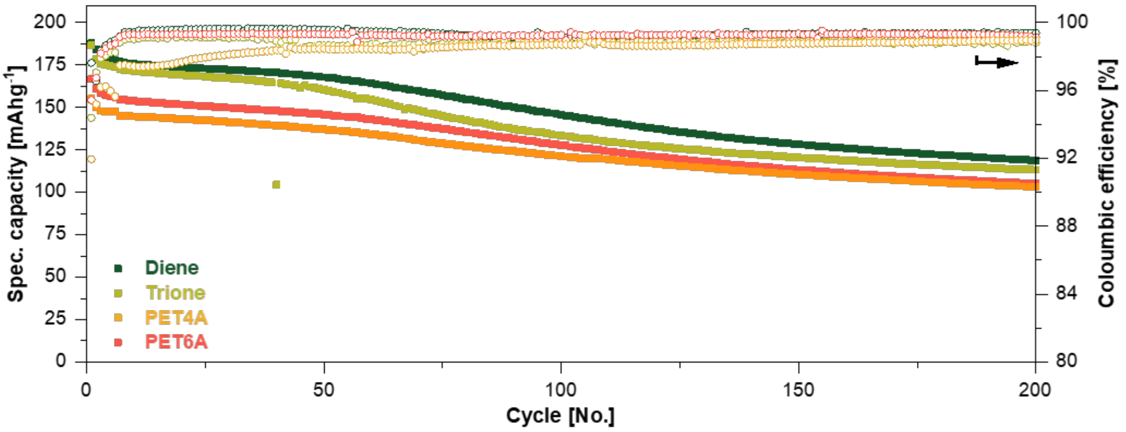

Figure 5.36: Cycling performance (capacity vs. cycle number and the corresponding Coulombic efficiency) of Na||PW cells using the diene-, trione-, PET4A- and PET6A-SIPEs (included 50 wt.% of molecular transporter). The galvanostatic cycling tests were carried out at 40 °C, applying C/50 in the first cycle, C/20 in the following 5 cycles and C/10 until achieving 200 cycles, between 3.8 V and 1.3 V.

5.5.7 Conclusion on the use of different Backbones

The influence of the backbone components on the electrochemical properties of NaMTFSI, PETMP and PVDF-HFP SIPE together with either diene, trione, PET4A or PET6A backbone monomer has been investigated. The number of cross-linking sites increased from diene (2) to PET6A (6), showing that a lower amount of cross-linking results in bigger pores and a higher ionic conductivity but a reduced mechanical stability. The diene-SIPE showed the highest ionic conductivity of $1.8 \cdot 10^{-4}$ S cm^{-1} at RT (+127% compared to the NaMTFSI-SIPE) and $6.0 \cdot 10^{-4}$ S cm^{-1} at 90 °C (+33% compared to the NaMTFSI-SIPE) and a specific capacity of 119 mAh g^{-1} after 200 cycles at 0.1C, which is 15% higher compared to the NaMTFSI-SIPE. These results reveal the need to investigate the chemistry of the SIPE components further to boost their physicochemical, mechanical and electrochemical properties with the final goal of manufacturing high-performing quasi-solid-state SMBs.

Chapter 5.6

Combing the Best Performing Anionic Center, Spacer Arm and Backbone Monomers

Various properties of the SIPE were investigated and different paths to optimize the electrochemical performance of the SIPE were revealed in the previous chapters. The ionic conductivity showed to be an effective tool to get an idea about the performance of the SIPE inside a SMB, thus the best performing SSM, anionic center, polymer backbone and their ratio were combined to further develop a new and optimized polymer SIPE membrane.

5.6.1 Overview of the Obtained Advantages

This thesis started with the design and analysis of the NaSTFSI-SIPE, following a literature known PET-4A/MP-SIPE for LMBs.[82] The thermal properties were similar, however, the electrochemical properties such as the ionic conductivity were significantly lower, which set the starting point for the follow-up investigations. After improving the components ratio and understanding their influence on the properties of the SIPE, the $TFSI^-$ anionic center was replaced with a $C(CN)_2^-$ anionic center, resulting in the NaSDCM-SIPE membrane with a slightly improved ionic conductivity. In parallel, the influence of a more flexible spacer arm was investigated and a non-fluorinated methacrylate spacer arm that tethers the anionic center to the polymer backbone (NaMTFSI-SIPE) showed to improve the conductivity more significantly. Next, the PET4A backbone was exchange with a more open-pore structure with fewer cross-links (diene-SIPE), allowing the Na ions to pass through the polymer matrix more easily and resulting in an even higher conductivity (Figure 5.37). The final chapter uses the cyano methanide group of chapter 5.3 with the methacrylate spacer arm (Chapter 5.4) and the open-pore PETMP/Diene backbone (Chapter 5.5) together as a NaMDCM-SIPE. The ionic conductivity of the optimized

NaMDCM-SIPE also shows the Vogel-Tamman-Vulcher behavior between 10 °C and 90 °C and exceeds all previously measured conductivities, reaching 1 mS cm^{-1} at 90 °C and $3.5 \cdot 10^{-4}$ S cm^{-1} at 20 °C.

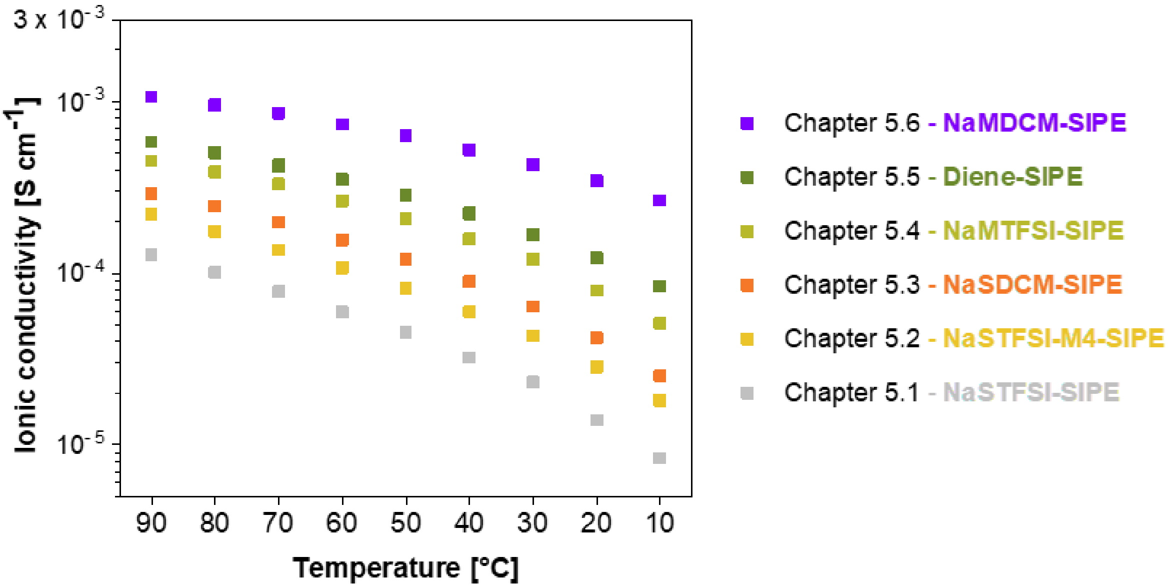

Figure 5.37: Temperature-depending ionic conductivity of the NaSTFSI-, optimized NaSTFSI-, NaSDCM-, NaMTFSI-, diene- and NaMDCM-SIPE between 10 and 90 °C.

5.6.2 Thermal and Electrochemical Characterization of the NaMDCM-SIPE

The optimized NaMDCM-SIPE was thermally and electrochemically characterized. First, the thermal stability was assessed by TGA (Figure 5.39a) and the thermal phase transition by DSC (Figure 5.39b). The TGA revealed that the SIPE is thermally stable up to 250 °C, which is identical to the thermal stability of the NaSDCM-PETMP/4A SIPE from Chapter 5.2, as the dicyano methanide group decomposes at higher temperatures. The DSC scan shows a glass transition temperature around 25 °C and two crystallization points at 100 °C and 140 °C, respectively. The first crystallization point (T_c^1) relates to the crystallization of PVDF-HFP chains, while the second crystallization temperature can be linked to the crystallization of the polymer backbone.

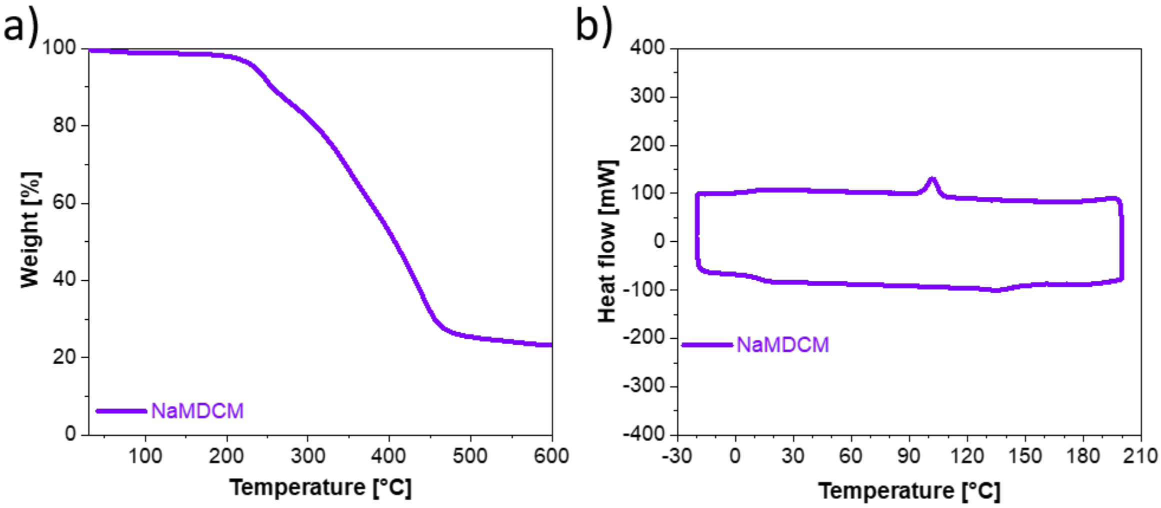

Figure 5.38: a) TGA and b) DSC of NaMDCM-SIPE (heating rate of 5 K min^{-1}, inert N_2 atmosphere). The DSC was performed by two cooling and heating cycles between -20 °C and 200 °C.

The electrochemical stability window was assessed by LSV (Figure 5.39a), revealing no electrochemical limitation in cathodic scan prior to sodium-metal plating at 0 V vs Na^+/Na and an anodic stability up to 4.5 V vs Na^+/Na, comparable to the previously studied SIPEs.[153] The stripping and plating behavior was studied at different current densities between 10 and 50 µA cm^{-2} (Figure 5.39b). The overpotential increases with increasing current density up to a stable overpotential of 950 mV at 50 µA cm^{-2}, while the interfacial resistance (Figure 5.39c) decreases slightly upon cycling and stabilizes around 1.7 kΩ upon prolonged cycling. The stable overpotential and interfacial resistance suggest that the NaMDCM-SIPE is well-suited for prolonged cycling in SMBs.

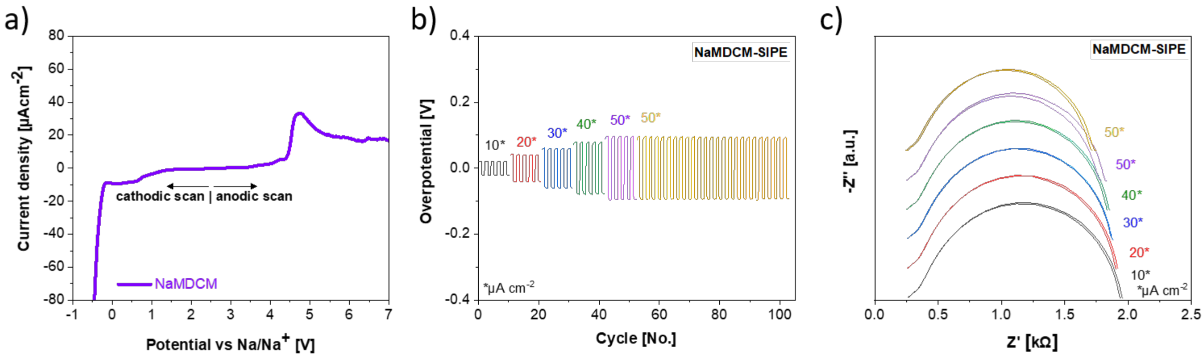

Figure 5.39: a) The electrochemical potential window of the NaMDCM-SIPE. b) The stripping and plating behavior of the of the NaMDCM-SIPE in Na||Na cells at 40 °C with an increasing current density between 10 and 50 µA cm^{-2} and c) the impedance plot after the 1st and 5th cycle of each current density and after long-term cycling at 50 µA cm^{-2}.

5.6.3 Cycling Performance of NaMDCM-Based SIPEs

The cycling performance of the NaMDCM-SIPE was studied in Na||SIPE||PW cells using a higher charge/discharge procedure starting with a formation cycle at C/50, followed by 5 cycles at 0.1 C and prolonged cycling at 1 C to test a more realistic charge/discharge profile. The voltage profile of the Na||NaMDCM-SIPE||PW cell (Figure 5.40a) shows the two plateaus of PW at 3.0 and 3.3 V vs Na^+/Na only in the formation cycle, due to the increased cell polarization with increasing charge-rate. The cycling test (Figure 5.40b and c) shows an initial charge/discharge capacity of 399 and 194 $mAhg^{-1}$, respectively, which suggests fast kinetics and a fast SEI formation through the decomposition of the plasticizers. After the initial SEI formation, the Coulombic efficiency increases to 98% in the following 5 cycles and up to 99.6% upon long-term cycling. The specific capacity decreases to 107 mAh g^{-1} after 200 cycles and delivered a specific capacity of 66 mAh g^{-1} after 1000 cycles at 1 C at 40 °C.

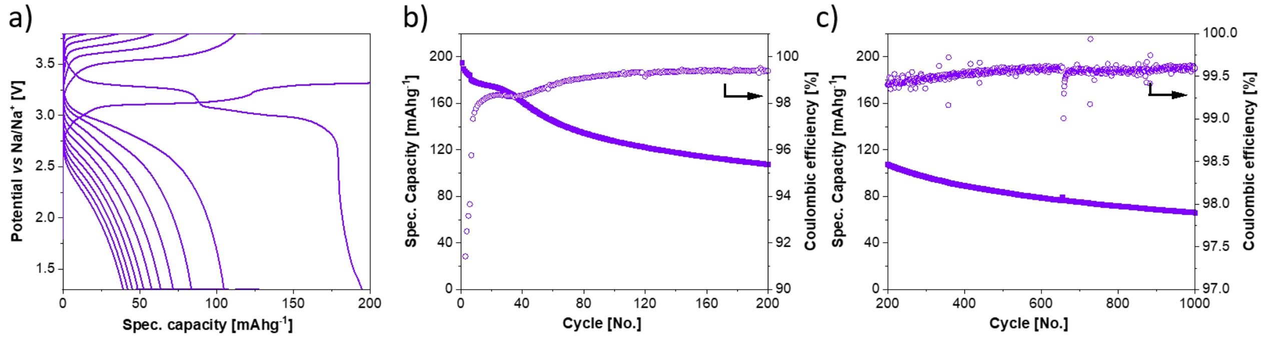

Figure 5.40: a) Voltage profile of the NaMDCM-SIPE and b) cycling performance up to 200 cycles and c) up to 100 cycles at 40 °C. The cell was run at 1 C after an initial formation cycle at C/50 and 5 cycles at 0.1 C.

5.6.4 Conclusion on the Optimized NaMDCM-SIPE

The investigation of the NaMDCM-SIPE showed that the combination of the above-mentioned optimizations resulted in a very high ion conductive Na-based SIPE that offers a wide stability window up to 4.5 V vs Na^+/Na, a moderate overpotential of 0.95 V at 50 µA cm^{-2} coupled with a low interfacial resistance of 1.7 k in Na||Na symmetric cells. The NaMDCM-SIPE reached $3.5 \cdot 10^{-4}$ mS cm^{-1} at RT (+94% compared to the NaMTFSI-diene-SIPE) and 1 mS cm^{-1} at 90 °C (+66% compared to the NaMTFSI-diene-SIPE), fulfilling the minimum ionic conductivity requirement reported for SIPEs.[85] The cycling performance of the NaMDCM-SIPE was investigated at 1 C, displaying the potential to cycle SMBs with QSS-SIPEs at high charge/discharge rates for over 1000 cycles.

Conclusion and Outlook

Chapter 6.1

Conclusion

Mass produced, cheap and green batteries are a necessity for a sustainable future. SIBs and SMBs appear to be promising candidates. However, SMBs offer far higher theoretical capacity than SIBs. SMBs can be realized by using SIPEs, which provide high safety and good cycle performance. SIPEs for SMBs have not been widely investigated, thus, this thesis work focused on various factors influencing the performance of SIPEs with the aim to develop a deeper understanding of SIPEs in general and develop a well performing Na||SIPE||PW cell.

The study was conducted on a self-standing, flexible, quasi-solid-state SIPE composed of a functionalized and cross-linked polymer network adapted from a highly-conducting Li-based SIPE. First, the three dimensional structure of the SIPE membrane was confirmed by various techniques and its thermal and electrochemical properties were assessed. These properties were used as reference for the follow-up investigation and optimization of the component's influences. However, the electrochemical properties, such as ionic conductivity, were not as good as for the Li-based SIPE. To improve the electrochemical performance, the ratio of the SIPEs components was varied to further deepen the understanding of each influencing factor towards the membranes thermal and electrochemical performance. Namely, different ratios of the two backbone components were studied, revealing the optimum amount of the SSM-binding backbone monomer (PETMP) to be slightly higher compared to the other two monomers (NaSTFSI and PET4A). Next, the ratio of supporting polymer PVDF-HFP inside the SIPE was assessed, revealing that it improves the molecular transporter uptake and conductivity with increasing amount of PVDF-HFP. However, high ratios of PVDF-HFP showed a decrease in the conductivity, due to the decreasing percentage of SSM in the SIPE, which are essential for the ion transport, thus an optimum ratio was found. Following, the amount of SSM was directly varied, showing that higher amounts of SSM were able to improve the conductivity and cell cycling performance up to a certain maximum. The limitation of the SSM ratio was the membranes homogeneity, which rapidly decreased at high ratios of SSMs due to the excess of vinyl groups that formed homo-polymers instead of forming the desired cross-linked structure with PETMP.

The charge delocalization plays an essential role in boosting the cations mobility and thus the SIPEs electrochemical performance. Following, different anionic centers were investigated by using either NaSTFSI, NaSDCM or NaVBS as sodium salt monomers. The NaSDCM SSM showed an improved conductivity compared to the previously TFSI-based anionic center, due to the lower binding energy towards the cation. Nevertheless, the ionic conductivity was not improving the level of the Li analogue, thus the mobility of the anionic center was investigated by using NaSTFSI, NaMTFSI and NaFTFSI as sodium salt monomers. These SSMs feature different spacer arms, which confirmed that a longer, more flexible spacer arm results in a higher mobility of the anionic center and thus a better conductivity.

Last, different polymer backbones were investigated using the NaMTFSI side chain with either PET4A, Diene, Trione or PET6A as polymer backbone monomer together with PETMP. The most porous backbone structure resulted in the diene-based SIPE with the overall best ionic conductivity and cycling performance, while the mechanical stability peaked for the PET4A-based SIPE with more cross connections inside the backbone. The obtained advantages of the anionic center, the side chain and the polymer backbone were combined in a new NaMDCM-SIPE that reached a high conductivity of 1 ms cm^{-1} at 90 °C, a high thermal stability, a wide potential window, a low overpotential and stable cycling in Na||SIPE||PW cells for over 1000 cycles at 1C.

Chapter 6.2
Outlook

In this thesis, various approaches to influence and improve the conductivity, thermal and mechanical stability, and the cycling performance were investigated. Comparing the same system with varying parameters revealed insight into the working mechanism of SIPEs and is expected to lay ground for an even deeper understanding and a following optimization of SIPEs in the future. Most noticeably, the combination of the cyano methanide anionic group and the methacrylate side chain showed promising potential as SSM in Na-based SIPE. Additionally, a first insight of the influence of the porosity of the three-dimensional backbone on the SIPEs performance was gained. Despite the broadness of the study, not all influence factors on SIPEs could be assessed and some influences remain unknown. Additional studies are needed to fully understand how SIPEs can be modified to further improve their electrochemical performance.

This work studied the impact of various SIPE components, including the impact of the amount of the PVDF-HFP. However, the supporting polymer itself was not varied. Future studies could potentially look into the influence of PVDF-HFP itself by replacing PVDF-HFP for example with PAN or PEO to produce a fluorine free SIPE, resulting in a new NaF-free SEI that is potentially even more stable upon cycling. Next, the backbone in this thesis was fully organic-based, due to its easy modularity, however, the use of an inorganic components in the backbone such as SiO_2 chains could further improve the conductivity and potentially the mechanical integrity of the SIPE. The amount of cross-linker was indirectly changed by varying the amount of molecular bonds between the backbone components, however, the use of a linear SiO_2 chain with one or two functional vinyl groups per repeating unit would allow to set the ratio between cross-linking and ionic conducting groups even more precisely, while also allowing an easier processability. Initial studies on this fascinating field were already conducted, showing a promising ionic conductivity above 1 ms cm^{-1} at RT. Another exciting research field would be the design of anode free cells where sodium is directly plated on a carbon-coated aluminum current collector instead of sodium-metal. This would allow to further reduce the thickness of the cell overall, while improving the contact area between the electrolyte and the SIPE. This contact area is especially important when avoiding the incorporated plasticizers in all-solid-state sodium-metal cells. All-solid-state SIPE cells utilize pressure to realize a good interface thus come with additional challenges and requirements for the SIPEs, which will need to be studied. Last, the synthesize procedure of the SIPEs in this thesis depends on a parallel polymerization of the backbone and the SSM with the backbone, which might be troublesome for an up-scaling. Instead, the membrane components as well as the plasticizers could be included into a precast PVDF-HFP porous membrane and light could be utilized to cross-link the components together for an easier processability, allowing an easier, faster, and cheaper production, thus representing an interesting field for further studies.

SIPEs are part of the green battery development that aims towards a future, where society mainly collects energy out of renewable sources and does not require coal, gas or nuclear energy. Realizing a carbon neutral future comes with various challenges but large-scale stationary storage via batteries to enable wind and solar energy is a big step to make this possible. Stationary energy storage for towns and cities will require massive storage systems, thus the batteries will have safety as their highest priority to avoid any possible dangers, followed by their price per GWh, while their weight and volume will be negligible. These priorities align with the desired properties for SIPEs, however, SIPE-based batteries still need to be improved regarding their safety, cycle rate, capacity retention and their potential for an upscaled production. Producing, understanding and optimizing SIPEs in the lab-scale is essential for this path, but lab-scaled research deals with different issues compared to production lines, thus the study on SIPEs could be made more efficient by designing clear benchmarks regarding expected costs, performance and synthesize procedure that align with industry standards. A cooperation between research and the industry could help to investigate and optimize SIPEs towards their commercial application in the future.

References

[1] R. Welch, P. A. Lamphier, *Technical innovation in american history: An encyclopedia of science and technology [3 volumes]*, Bloomsbury Publishing USA, **2019**.

[2] L. Day, I. McNeil, *Biographical dictionary of the history of technology*, Routledge, **2002**.

[3] C. W. Hall, *A Biographical Dictionary of People in Engineering: From the Earliest Records Until 2000*, Purdue University Press, **2008**.

[4] W. Bach, *International Journal of Hydrogen Energy* **1981**, *6*, 185–201.

[5] F. Martins, C. Felgueiras, M. Smitkova, N. Caetano, *Energies* **2019**, *12*, 964.

[6] A. Williams, *IEE Proceedings A (Science Measurement and Technology)* **1993**, *140*, 8–12.

[7] Y. Sun, Z. Zhao, M. Yang, D. Jia, W. Pei, B. Xu, *CSEE Journal of Power and Energy Systems* **2019**, *6*, 160–173.

[8] W. Wang, B. Yuan, Q. Sun, R. Wennersten, *Journal of Energy Storage* **2022**, *52*, 104812.

[9] C. Brunner, G. Deac, S. Braun, C. Zöphel, *Renewable Energy* **2020**, *149*, 1314–1324.

[10] L. Ma, J. Cui, S. Yao, X. Liu, Y. Luo, X. Shen, J.-K. Kim, *Energy Storage Materials* **2020**, *27*, 522–554.

[11] T. R. Crompton, *Battery reference book*, Newnes, **2000**.

[12] A. Volta, *Trans* **1800**, *2*, 430.

[13] B. Scrosati, *Journal of solid state electrochemistry* **2011**, *15*, 1623–1630.

[14] A. Jossen, W. Weydanz, et al., *Göttingen: MatrixMedia* **2006**.

[15] H. Zhang, M. Armand, *Israel Journal of Chemistry* **2021**, *61*, 94–100.

[16] J. Garche, C. K. Dyer, P. T. Moseley, Z. Ogumi, D. A. Rand, B. Scrosati, *Encyclopedia of electrochemical power sources*, Newnes, **2013**.

[17] G. Armstrong, *Nature chemistry* **2019**, *11*, 1076–1076.

[18] Z. Ogumi, R. Kostecki, D. Guyomard, M. Inaba, *The Electrochemical Society Interface* **2016**, *25*, 65.

[19] Y. Mekonnen, A. Sundararajan, A. I. Sarwat, *SoutheastCon 2016* **2016**, 1–6.

[20] C. Deng, X. Li, R. Chen, K. Ye, J. Lipton, S. A. Maclean, H. Wang, A. D. Taylor, G. Weng, *Energy Storage Materials* **2023**, *60*, 102820.

[21] Z. Chang, H. Yang, A. Pan, P. He, H. Zhou, *Nature Communications* **2022**, *13*, 6788.

[22] F. Wu, S. Fang, M. Kuenzel, A. Mullaliu, J.-K. Kim, X. Gao, T. Diemant, G.-T. Kim, S. Passerini, *Joule* **2021**, *5*, 2177–2194.

[23] I. energy agency, International energy agency, `https://www.iea.org`, Accessed: 2025-03-20.

[24] H. S. Hirsh, Y. Li, D. H. Tan, M. Zhang, E. Zhao, Y. S. Meng, *Advanced Energy Materials* **2020**, *10*, 2001274.

[25] P. K. Nayak, L. Yang, W. Brehm, P. Adelhelm, *Angewandte Chemie International Edition* **2018**, *57*, 102–120.

[26] L. Qiao, X. Judez, T. Rojo, M. Armand, H. Zhang, *Journal of The Electrochemical Society* **2020**, *167*, 070534.

[27] J. F. Peters, A. Peña Cruz, M. Weil, *Batteries* **2019**, *5*, 10.

[28] R. Usiskin, Y. Lu, J. Popovic, M. Law, P. Balaya, Y.-S. Hu, J. Maier, *Nature Reviews Materials* **2021**, *6*, 1020–1035.

[29] C. Vaalma, D. Buchholz, M. Weil, S. Passerini, *Nature Reviews Materials* **2018**, *3*.

[30] P. K. Nayak, L. Yang, W. Brehm, P. Adelhelm, *Angewandte Chemie* **2017**, *57*, 102–120.

[31] N. Yabuuchi, K. Kubota, M. Dahbi, S. Komaba, *Chemical reviews* **2014**, *114*, 11636–11682.

[32] Y. Wang, S. Song, C. Xu, N. Hu, J. Molenda, L. Lu, *Nano Materials Science* **2019**, *1*, 91–100.

[33] W. Lu, Z. Wang, S. Zhong in Journal of Physics: Conference Series, *Vol. 2109*, IOP Publishing, **2021**, p. 012004.

[34] C. Ruiz, Sodium-ion batteries ready for commercialisation: for grids, homes, even compact EVs. Accessed: 2023-09-30, **2023**, `https://energypost.eu/sodium-ion-batteries-ready-for-commercialisation-for-grids-homes-even-compact-evs/`.

[35] V. Media, Powering the future: what's the outlook for energy storage systems, `https://www.energymonitor.ai/sponsored/powering-the-future-whats-the-outlook-for-energy-storage-systems/`, Accessed: 2024-11-13.

[36] L. Xiao, Y. Cao, J. Xiao, W. Wang, L. Kovarik, Z. Nie, J. Liu, *Chemical communications* **2012**, *48*, 3321–3323.

[37] H. Zhang, I. Hasa, S. Passerini, *Advanced Energy Materials* **2018**, *8*, 1702582.

[38] Y. Wen, K. He, Y. Zhu, F. Han, Y. Xu, I. Matsuda, Y. Ishii, J. Cumings, C. Wang, *Nature communications* **2014**, *5*, 4033.

[39] Q. Liu, R. Xu, D. Mu, G. Tan, H. Gao, N. Li, R. Chen, F. Wu, *Carbon Energy* **2022**, *4*, 458–479.

[40] D. Cheng, X. Zhou, H. Hu, Z. Li, J. Chen, L. Miao, X. Ye, H. Zhang, *Carbon* **2021**, *182*, 758–769.

[41] L. Fan, Q. Liu, S. Chen, Z. Xu, B. Lu, *Advanced Energy Materials* **2017**, *7*, 1602778.

[42] X. Dou, I. Hasa, D. Saurel, C. Vaalma, L. Wu, D. Buchholz, D. Bresser, S. Komaba, S. Passerini, *Materials Today* **2019**, *23*, 87–104.

[43] H. Moon, M. Zarrabeitia, E. Frank, O. Böse, M. Enterría, D. Saurel, I. Hasa, S. Passerini, *Batteries & Supercaps* **2021**, *4*, 960–977.

[44] L. Fu, K. Tang, K. Song, P. A. van Aken, Y. Yu, J. Maier, *Nanoscale* **2014**, *6*, 1384–1389.

[45] D. M. Zhang, J. H. Jia, C. C. Yang, Q. Jiang, *Energy Storage Materials* **2020**, *24*, 439–449.

[46] H. Moon, A. Innocenti, H. Liu, H. Zhang, M. Weil, M. Zarrabeitia, S. Passerini, *ChemSusChem* **2023**, *16*, e202201713.

[47] Z. A. Ghazi, Z. Sun, C. Sun, F. Qi, B. An, F. Li, H.-M. Cheng, *Small* **2019**, *15*, 1900687.

[48] Y. Cai, X. Cao, Z. Luo, G. Fang, F. Liu, J. Zhou, A. Pan, S. Liang, *Advanced Science* **2018**, *5*, 1800680.

[49] C. Zhu, C. Wu, C.-C. Chen, P. Kopold, P. A. van Aken, J. Maier, Y. Yu, *Chemistry of Materials* **2017**, *29*, 5207–5215.

[50] L. Wang, J. Song, R. Qiao, L. A. Wray, M. A. Hossain, Y.-D. Chuang, W. Yang, Y. Lu, D. Evans, J.-J. Lee, et al., *Journal of the American Chemical Society* **2015**, *137*, 2548–2554.

[51] S. Baumgart, M. Sotoudeh, A. Groß, *Batteries & Supercaps* **2023**, *6*, e202300294.

[52] M. Reid, Sodium-ion batteries: disrupt and conquer?, `https://www.woodmac.com/news/opinion/sodium-ion-batteries-disrupt/`, Accessed: 2024-11-15.

[53] C. Bao, B. Wang, P. Liu, H. Wu, Y. Zhou, D. Wang, H. Liu, S. Dou, *Advanced Functional Materials* **2020**, *30*, 2004891.

[54] J. Liu, S. Ihuaenyi, R. Kuphal, J. Salinas, L. Xie, L. Yang, U. Janakiraman, M. E. Fortier, C. Fang, *Journal of The Electrochemical Society* **2023**, *170*, 010535.

[55] J. Yang, H. Zhang, Q. Zhou, H. Qu, T. Dong, M. Zhang, B. Tang, J. Zhang, G. Cui, *ACS applied materials & interfaces* **2019**, *11*, 17109–17127.

[56] X. Fan, L. Chen, O. Borodin, X. Ji, J. Chen, S. Hou, T. Deng, J. Zheng, C. Yang, S.-C. Liou, et al., *Nature nanotechnology* **2018**, *13*, 715–722.

[57] C. Monroe, J. Newman, *Journal of The Electrochemical Society* **2005**, *152*, A396.

[58] C. Monroe, J. Newman, *Journal of The Electrochemical Society* **2003**, *150*, A1377.

[59] C. Brissot, M. Rosso, J.-N. Chazalviel, S. Lascaud, *Journal of power sources* **1999**, *81*, 925–929.

[60] C. Brissot, M. Rosso, J.-N. Chazalviel, P. Baudry, S. Lascaud, *Electrochimica acta* **1998**, *43*, 1569–1574.

[61] M. Rosso, C. Brissot, A. Teyssot, M. Dollé, L. Sannier, J.-M. Tarascon, R. Bouchet, S. Lascaud, *Electrochimica Acta* **2006**, *51*, 5334–5340.

[62] J. Jia, B. Guo, H. Gao, Y. Zhao, G. Li, A. Wang, C. Liu, *Materials Today Energy* **2024**, 101664.

[63] B. Lee, E. Paek, D. Mitlin, S. W. Lee, *Chemical reviews* **2019**, *119*, 5416–5460.

[64] F. Zheng, M. Kotobuki, S. Song, M. O. Lai, L. Lu, *Journal of Power Sources* **2018**, *389*, 198–213.

[65] S. Passerini, D. Bresser, A. Moretti, A. Varzi, *Batteries: present and future energy storage challenges*, John Wiley & Sons, **2020**.

[66] G. G. Eshetu, G. A. Elia, M. Armand, M. Forsyth, S. Komaba, T. Rojo, S. Passerini, *Advanced Energy Materials* **2020**, *10*, 2000093.

[67] J. Han, R. H. Gee, R. H. Boyd, *Macromolecules* **1994**, *27*, 7781–7784.

[68] I. M. Kalogeras, W. Brostow, *Journal of Polymer Science Part B: Polymer Physics* **2009**, *47*, 80–95.

[69] C. Berthier, W. Gorecki, M. Minier, M. Armand, J. Chabagno, P. Riguad, *Solid State Ionics* **1983**, *11*, 91–95.

[70] Z. Osman, K. B. Md Isa, A. Ahmad, L. Othman, *Ionics* **2010**, *16*, 431–435.

[71] P. B. Bhargav, V. M. Mohan, A. Sharma, V. N. Rao, *Current Applied Physics* **2009**, *9*, 165–171.

[72] C. V. S. Reddy, X. Han, Q.-Y. Zhu, L.-Q. Mai, W. Chen, *European polymer journal* **2006**, *42*, 3114–3120.

[73] K. N. Kumar, T. Sreekanth, M. J. Reddy, U. S. Rao, *Journal of power sources* **2001**, *101*, 130–133.

[74] J. Mindemark, R. Mogensen, M. J. Smith, M. M. Silva, D. Brandell, *Electrochemistry Communications* **2017**, *77*, 58–61.

[75] R. Chandrasekaran, S. Selladurai, *Journal of Solid State Electrochemistry* **2001**, *5*, 355–361.

[76] X. Qi, Q. Ma, L. Liu, Y.-S. Hu, H. Li, Z. Zhou, X. Huang, L. Chen, *ChemElectroChem* **2016**, *3*, 1741–1745.

[77] A. Boschin, P. Johansson, *Electrochimica Acta* **2015**, *175*, 124–133.

[78] W. Gorecki, M. Jeannin, E. Belorizky, C. Roux, M. Armand, *Journal of Physics: Condensed Matter* **1995**, *7*, 6823.

[79] J.-H. Shin, W. A. Henderson, C. Tizzani, S. Passerini, S.-S. Jeong, K.-W. Kim, *Journal of The Electrochemical Society* **2006**, *153*, A1649.

[80] J. Zheng, W. Li, X. Liu, J. Zhang, X. Feng, W. Chen, *Energy & Environmental Materials* **2023**, *6*, e12422.

[81] X. Cheng, J. Pan, Y. Zhao, M. Liao, H. Peng, *Advanced Energy Materials* **2018**, *8*, 1702184.

[82] Y. Zhong, L. Zhong, S. Wang, J. Qin, D. Han, S. Ren, M. Xiao, L. Sun, Y. Meng, *Journal of Materials Chemistry A* **2019**, *7*, 24251–24261.

[83] G. Feuillade, P. Perche, *Journal of Applied Electrochemistry* **1975**, *5*, 63–69.

[84] J.-M. Tarascon, A. Gozdz, C. Schmutz, F. Shokoohi, P. Warren, *Solid State Ionics* **1996**, *86*, 49–54.

[85] H.-K. Kim, V. Srinivasan, *Journal of The Electrochemical Society* **2020**, *167*, 130520.

[86] A. Mayer, H.-D. Nguyen, A. Mariani, T. Diemant, S. Lyonnard, C. Iojoiu, S. Passerini, D. Bresser, *ACS Macro Letters* **2022**, *11*, 982–990.

[87] A.-C. Genix, V. Bocharova, A. Kisliuk, B. Carroll, S. Zhao, J. Oberdisse, A. P. Sokolov, *ACS applied materials & interfaces* **2018**, *10*, 33601–33610.

[88] C. R. South, C. Burd, M. Weck, *Accounts of chemical research* **2007**, *40*, 63–74.

[89] L. Deng, G. Chen, *Nano Energy* **2021**, *80*, 105448.

[90] R. J. Wojtecki, A. Nelson, *Journal of Polymer Science Part A: Polymer Chemistry* **2016**, *54*, 457–472.

[91] H. Papananou, E. Perivolari, K. Chrissopoulou, S. H. Anastasiadis, *Polymer* **2018**, *157*, 111–121.

[92] L. Chen, S. Xu, D. McBranch, D. Whitten, *Journal of the American Chemical Society* **2000**, *122*, 9302–9303.

[93] O. Bubnova, M. Berggren, X. Crispin, *Journal of the American Chemical Society* **2012**, *134*, 16456–16459.

[94] H. Zhang, C. Li, M. Piszcz, E. Coya, T. Rojo, L. M. Rodriguez-Martinez, M. Armand, Z. Zhou, *Chemical Society Reviews* **2017**, *46*, 797–815.

[95] M. Martinez-Ibañez, E. Sanchez-Diez, L. Qiao, L. Meabe, A. Santiago, H. Zhu, L. A. O'Dell, J. Carrasco, M. Forsyth, M. Armand, et al., *Batteries & Supercaps* **2020**, *3*, 738–746.

[96] D. Bannister, G. Davies, I. Ward, J. McIntyre, *Polymer* **1984**, *25*, 1291–1296.

[97] D. Benrabah, S. Sylla, J.-Y. Sanchez, M. Armand, *Journal of power sources* **1995**, *54*, 456–460.

[98] C. Cao, Y. Li, Y. Feng, P. Long, H. An, C. Qin, J. Han, S. Li, W. Feng, *Journal of Materials Chemistry A* **2017**, *5*, 22519–22526.

[99] C. Cao, Y. Li, Y. Feng, C. Peng, Z. Li, W. Feng, *Energy Storage Materials* **2019**, *19*, 401–407.

[100] K. Deng, Q. Zeng, D. Wang, Z. Liu, Z. Qiu, Y. Zhang, M. Xiao, Y. Meng, *Journal of Materials Chemistry A* **2020**, *8*, 1557–1577.

[101] R. Rohan, K. Pareek, Z. Chen, W. Cai, Y. Zhang, G. Xu, Z. Gao, H. Cheng, *Journal of Materials Chemistry A* **2015**, *3*, 20267–20276.

[102] X. Liu, W. Mao, J. Gong, H. Liu, Y. Shao, L. Sun, H. Wang, C. Wang, *Polymers* **2023**, *15*, 394.

[103] A. Mayer, T. Ates, A. Varzi, S. Passerini, D. Bresser, *Frontiers in Chemistry* **2022**, *10*, 974202.

[104] X. Dong, X. Liu, H. Li, S. Passerini, D. Bresser, *Angewandte Chemie* **2023**, *135*, e202308699.

[105] J. Zhang, S. Wang, D. Han, M. Xiao, L. Sun, Y. Meng, *Energy Storage Materials* **2020**, *24*, 579–587.

[106] J. L. Olmedo-Martínez, A. Fdz De Anastro, M. Martínez-Ibañez, A. J. Müller, D. Mecerreyes, *Energy & Fuels* **2023**, *37*, 5519–5529.

[107] S. Das, S. Jana, M. Orságh, K. Byś, J. Mishra, M. Uchman, V. Adyam, *ACS Applied Energy Materials* **2023**, *6*, 5113–5121.

[108] K. Liu, Y. Xie, Z. Yang, H.-K. Kim, T. L. Dzwiniel, J. Yang, H. Xiong, C. Liao, *Journal of the Electrochemical Society* **2021**, *168*, 120543.

[109] L. Yang, Y. Jiang, X. Liang, Y. Lei, T. Yuan, H. Lu, Z. Liu, Y. Cao, J. Feng, *ACS Applied Energy Materials* **2020**, *3*, 10053–10060.

[110] J. Li, H. Zhu, X. Wang, M. Armand, D. R. MacFarlane, M. Forsyth, *Electrochimica Acta* **2015**, *175*, 232–239.

[111] I. Scholz, P. Hodgkinson, B. H. Meier, M. Ernst, *The Journal of chemical physics* **2009**, *130*.

[112] C. Hucher, F. Beaume, R.-P. Eustache, P. Tekely, *Macromolecules* **2005**, *38*, 1789–1796.

[113] K. Schmidt-Rohr, H. W. Spiess, *Multidimensional solid-state NMR and polymers*, Elsevier, **2012**.

[114] H. Friebolin, *Ein-und zweidimensionale NMR-Spektroskopie: eine Einführung*, John Wiley & Sons, **2013**.

[115] W. Reusch, Nuclear Magnetic Resonance Spectroscopy, `https://www2.chemistry.msu.edu/faculty/reusch/virttxtjml/spectrpy/nmr/nmr1.htm`, Accessed: 2025-03-12.

[116] G. Metz, M. Ziliox, S. O. Smith, *Solid State Nuclear Magnetic Resonance* **1996**, *7*, 155–160.

[117] C. S. Yannoni, *Accounts of Chemical Research* **1982**, *15*, 201–208.

[118] W. Herres, J. Gronholz, *Part* **1984**, *1*, 5.

[119] S. Gómez-Graña, M. Perez-Ameneiro, X. Vecino, I. Pastoriza-Santos, J. Perez-Juste, J. M. Cruz, A. B. Moldes, *Nanomaterials* **2017**, *7*, 139.

[120] R. B. Prime, J. D. Menczel, *Thermal analysis of polymers: fundamentals and applications*, John Wiley & Sons, **2009**.

[121] J. D. Menczel, R. B. Prime, *Thermal analysis of polymers*, Wiley Online Library, **2009**.

[122] G. Delaizir, L. Calvez, *Sintering of Ceramics—New Emerging Techniques* **2012**, 281–306.

[123] P. J. Lingane, D. G. Peters, *CRC Critical Reviews in Analytical Chemistry* **1971**, *1*, 587–634.

[124] D. D. Macdonald, D. D. Macdonald, *Transient Techniques in Electrochemistry* **1977**, 119–184.

[125] D. Garreau, J. Savéant, *Journal of Electroanalytical Chemistry and Interfacial Electrochemistry* **1972**, *35*, 309–331.

[126] V. D. Parker in *Comprehensive Chemical Kinetics*, *Vol. 26*, Elsevier, **1986**, pp. 145–202.

[127] A. Haghipour, M. Tahertalari, M. M. Kalantarian, *Sustainable Energy & Fuels* **2022**, *6*, 879–893.

[128] S. Tu, X. Ren, J. He, Z. Zhang, *Fatigue & Fracture of Engineering Materials & Structures* **2020**, *43*, 3–19.

[129] S. Wang, J. Zhang, O. Gharbi, V. Vivier, M. Gao, M. E. Orazem, *Nature Reviews Methods Primers* **2021**, *1*, 41.

[130] P. Van der Heide, *X-ray photoelectron spectroscopy: an introduction to principles and practices*, John Wiley & Sons, **2011**.

[131] B. Chu, B. S. Hsiao, *Chemical reviews* **2001**, *101*, 1727–1762.

[132] M. C. Biesinger, *Applied Surface Science* **2022**, *597*, 153681.

[133] G. Socrates, *Infrared and Raman characteristic group frequencies: tables and charts*, John Wiley & Sons, **2004**.

[134] M. T. Gokmen, J. Brassinne, R. A. Prasath, F. E. Du Prez, *Chemical Communications* **2011**, *47*, 4652–4654.

[135] S. Kuypers, S. K. Pramanik, L. D'Olieslaeger, G. Reekmans, M. Peters, J. D'Haen, D. Vanderzande, T. Junkers, P. Adriaensens, A. Ethirajan, *Chemical Communications* **2015**, *51*, 15858–15861.

[136] K. Schmidt-Rohr, H. W. Spiess, *Multidimensional solid-state NMR and polymers*, Elsevier, **2012**.

[137] C. Hucher, F. Beaume, R.-P. Eustache, P. Tekely, *Macromolecules* **2005**, *38*, 1789–1796.

[138] S. Ferrari, E. Quartarone, P. Mustarelli, A. Magistris, M. Fagnoni, S. Protti, C. Gerbaldi, A. Spinella, *journal of Power Sources* **2010**, *195*, 559–566.

[139] R. Meziane, J.-P. Bonnet, M. Courty, K. Djellab, M. Armand, *Electrochimica Acta* **2011**, *57*, 14–19.

[140] D. Blundell, *Polymer* **1987**, *28*, 2248–2251.

[141] K. Ishino, H. Shingai, Y. Hikita, I. Yoshikawa, H. Houjou, K. Iwase, *ACS omega* **2021**, *6*, 32869–32878.

[142] H.-Y. Guan, Z.-B. Guo, J.-J. Ding, F. Lian, *Journal of Applied Polymer Science* **2016**, *133*.

[143] J. Baek, B. Yoon, H. Jeong, J. Jeong, S. Mamidi, H.-K. Seo, C.-R. Lee, I. Seo, *Journal of Electroanalytical Chemistry* **2022**, *920*, 116631.

[144] A. Gulino, F. Lupo, G. G. Condorelli, M. E. Fragalà, M. E. Amato, G. Scarlata, *Journal of Materials Chemistry* **2008**, *18*, 5011–5018.

[145] G. Beamson, *ICIplc* **1992**.

[146] V. Simone, L. Lecarme, L. Simonin, S. Martinet, *Journal of The Electrochemical Society* **2016**, *164*, A145.

[147] F. Buchner, M. Bozorgchenani, B. Uhl, H. Farkhondeh, J. Bansmann, R. J. Behm, *The Journal of Physical Chemistry C* **2015**, *119*, 16649–16659.

[148] Y. Peng, R. Badam, T. P. Jayakumar, W. Wannapakdee, C. Changtong, N. Matsumi, *Journal of the Electrochemical Society* **2022**, *169*, 050515.

[149] A. J. Dias, T. J. McCarthy, *Journal of Polymer Science: Polymer Chemistry Edition* **1985**, *23*, 1057–1061.

[150] M. A. Muñoz-Márquez, M. Zarrabeitia, E. Castillo-Martínez, A. Eguía-Barrio, T. Rojo, M. Casas-Cabanas, *ACS applied materials & interfaces* **2015**, *7*, 7801–7808.

[151] H. Kumar, E. Detsi, D. P. Abraham, V. B. Shenoy, *Chemistry of Materials* **2016**, *28*, 8930–8941.

[152] C. Sångeland, R. Mogensen, D. Brandell, J. Mindemark, *ACS Applied Polymer Materials* **2019**, *1*, 825–832.

[153] C. Wunder, T.-L. Lai, E. Šić, T. Gutmann, E. De Vito, G. Buntkowsky, M. Zarrabeitia, S. Passerini, *Journal of Materials Chemistry A* **2024**, *12*, 20935–20946.

[154] M. Krajewski, A. M. Witowski, S.-C. Liou, M. Maj, M. Tokarczyk, D. Wasik, *Macromolecular Rapid Communications* **2023**, *44*, 2300038.

[155] V. Raju, E. Menezes, G. Marin, W. Graessley, L. Fetters, *Macromolecules* **1981**, *14*, 1668–1676.

[156] P. De Gennes, *Macromolecules* **1976**, *9*, 594–598.

[157] M. Rubinstein, E. Helfand, *The Journal of chemical physics* **1985**, *82*, 2477–2483.

[158] S. Das, A. Ghosh, *Electrochimica Acta* **2015**, *171*, 59–65.

[159] Z. Chen, G.-T. Kim, J.-K. Kim, M. Zarrabeitia, M. Kuenzel, H.-P. Liang, D. Geiger, U. Kaiser, S. Passerini, *Advanced Energy Materials* **2021**, *11*, 2101339.

[160] L. A. Ma, A. J. Naylor, L. Nyholm, R. Younesi, *Angewandte Chemie International Edition* **2021**, *60*, 4855–4863.

[161] A. K. Nigam, M. Suryanarayana, P. Gutch, S. P. Sharma, L. Tomar, R. Vijayaraghavan, *Journal of Hazardous Materials* **2010**, *184*, 506–514.

[162] N. Boaretto, L. Meabe, M. Martinez-Ibañez, M. Armand, H. Zhang, *Journal of The Electrochemical Society* **2020**, *167*, 070524.

[163] F. Gebert, J. Knott, R. Gorkin, S.-L. Chou, S.-X. Dou, *Energy Storage Materials* **2021**, *36*, 10–30.

[164] C. Wunder, L. Hildebrand, L. Gräber, A. Varzi, D. Bresser, M. Zarrabeitia, S. Passerini, *EES Batteries* **2026**.

[165] A. Mayer, A. Mariani, X. Dong, G. Vansse, P. Theato, C. Iojoiu, S. Passerini, D. Bresser, *Macromolecules* **2023**, *56*, 2505–2514.

[166] M. Worzakowska, K. Sztanke, M. Sztanke, *International Journal of Molecular Sciences* **2024**, *25*, 4768.

[167] R. Xie, A. R. Weisen, Y. Lee, M. A. Aplan, A. M. Fenton, A. E. Masucci, F. Kempe, M. Sommer, C. W. Pester, R. H. Colby, et al., *Nature communications* **2020**, *11*, 893.

[168] H. Zipse, *Radicals in Synthesis I* **2006**, 163–189.

[169] R. A. Jackson, *Tetrahedron* **1991**, *47*, 6777–6786.

[170] J. M. Gutteridge, *Chemico-biological interactions* **1994**, *91*, 133–140.

[171] T. A. Ezquerra, A. Nogales, M. C. García-Gutiérrez, E. Rebollar, O. Gálvez, I. Šics, M. Malfois, *Polymer* **2022**, *249*, 124827.

[172] M. Li, H. J. Wondergem, M.-J. Spijkman, K. Asadi, I. Katsouras, P. W. Blom, D. M. De Leeuw, *Nature materials* **2013**, *12*, 433–438.

[173] A. K. Maurya, E. Mias, J. Schoeller, I. E. Collings, R. M. Rossi, A. Dommann, A. Neels, *Nanoscale advances* **2022**, *4*, 491–501.

[174] Z. Song, F. Chen, M. Martinez-Ibañez, W. Feng, M. Forsyth, Z. Zhou, M. Armand, H. Zhang, *Nature communications* **2023**, *14*, 4884.

[175] C. Wunder, L. Graeber, D. Bresser, M. Zarrabeitia, S. Passerini, *ACS Applied Polymer Materials* **2025**, *7*, 4895–4907.

Appendix

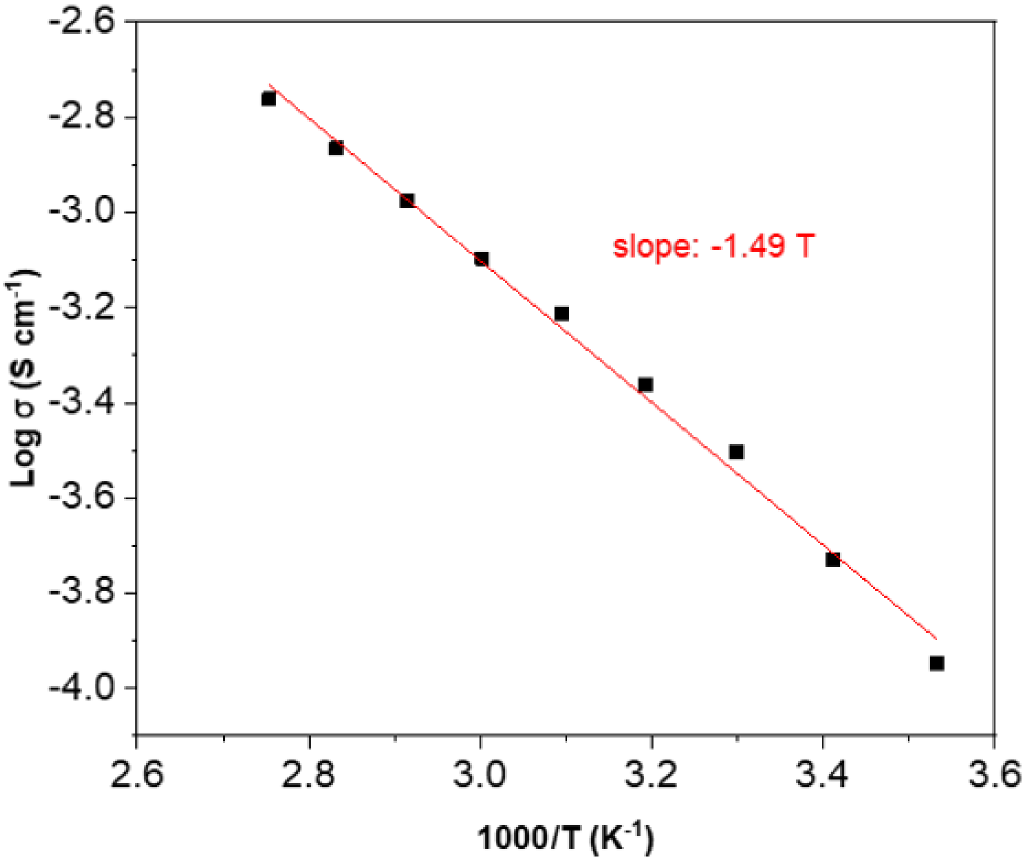

Figure 8.1: The logarithmic plot of the conductivity vs. 1000/T. The obtained slope of -1.49 T was multiplied with $-8.6 \cdot 10^{-5}$ eV T^{-1} to determine the activation energy of 0.13 eV.

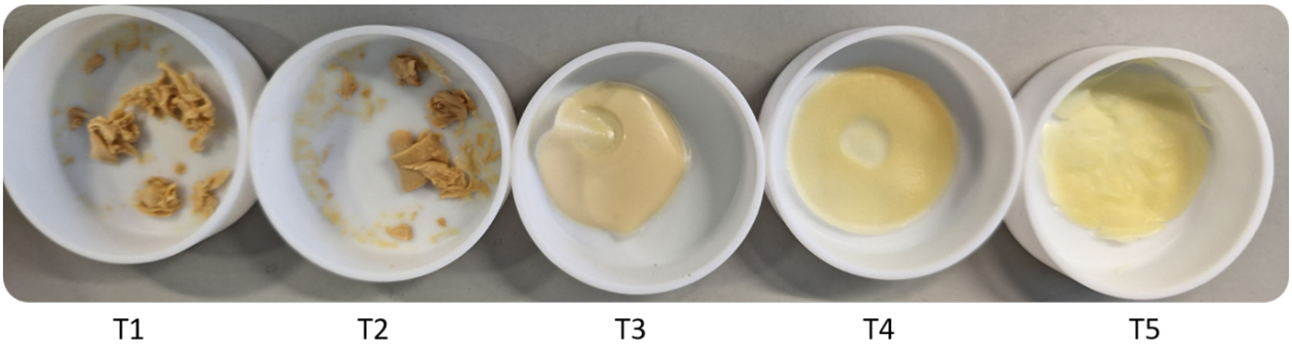

Figure 8.2: Photographs of NaSTFSI-SIPE membranes synthesized for the optimization of the PET4A/PETMP molar ratio. The PET4A/PETMP molar ratio has been varied in 15% steps, while the molar ratio of NaSTFSI and PVDF-HFP vs PETMP was kept constant at 20% and 44%, respectively. Table 5.1 shows the chemical molar ratio of NaSTFSI-SIPE membranes.

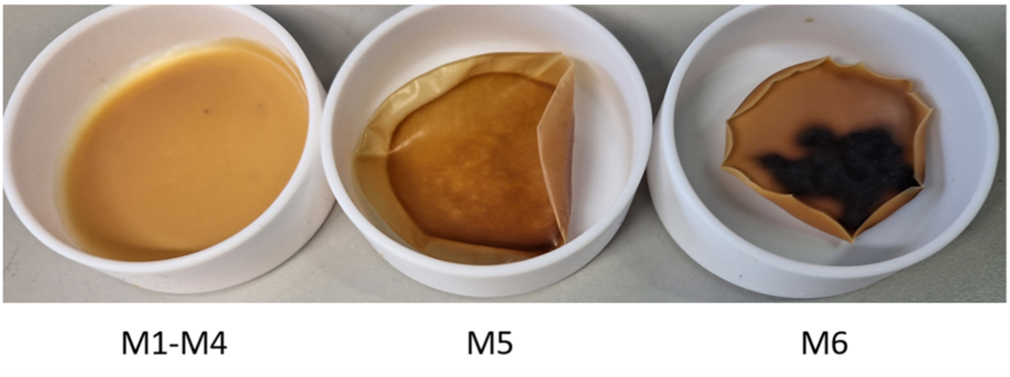

Figure 8.3: Photographs of NaSTFSI-SIPE membranes synthesized for the optimization of the NaSTFSI SSM content. Table 3 shows the chemical molar ratio of NaSTFSI-SIPE membranes.

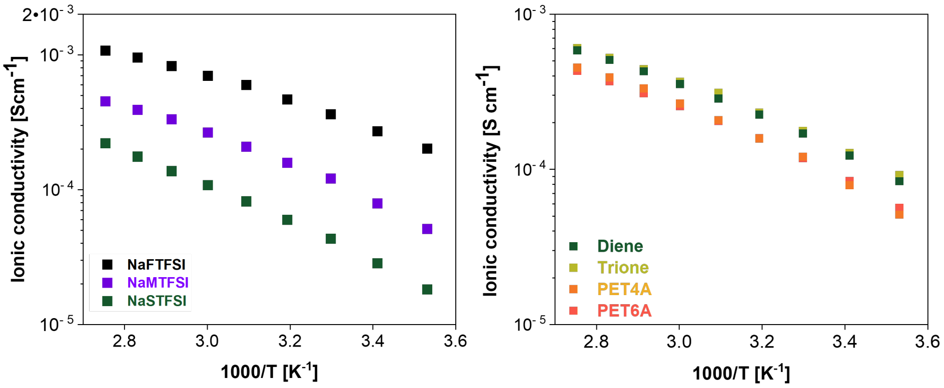

Figure 8.4: Arrhenius plot ln $(\sigma)vs1000/T)ofNaSTFSI-,NaMTFSI-andNaFTFSI-basedSIPEscontaining50wt.\%ofEC:DMC:FEC.$

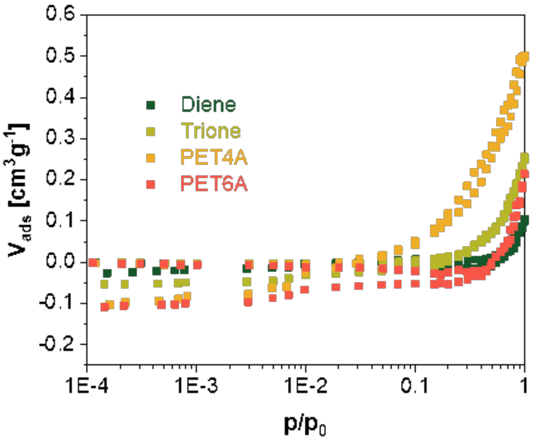

Figure 8.5: The isotherm of the BET measurements of the dry diene-, trione-, PET4A- and PET6A-based SIPEs with PVDF-HFP.

List of Figures

2.1 Scheme of a rechargeable battery. During discharge, the electrons travel from the negative electrode (anode, green) to the positive electrode (cathode, red), where the cations travel through the single ion-conducting electrolyte (blue), reducing the positive electrode and oxidizing the negative one. 4

2.2 Volumetric vs gravimetric energy density plot, where different battery chemistries are compared. Reprinted from ref.[19] ©2016 IEEE 6

2.3 Scheme of LIBs, a) upon charge and b) discharge, Li ions intercalate into the anode (during charge) and the cathode (during discharge) structure. Reprinted from Energy Storage Materials, Vol. 60, Deng et al.[20], Recent advances in rocking chair batteries and beyond, 102820, 2023, with permission from Elsevier. 7

2.4 The chemical structures of common carbonate solvents (upper row) and conducting salts (lower row). 8

2.5 Predicted growth of LIBs in EVs. The demand is expected to steadily increase and reach up to 5000 GWh in the next 10 years. Reprinted with permission from Rho Motion, 2024 9

2.6 Li and Na reserve distribution on the world. 11

2.7 Market share of different battery chemistries in 2023. Lithium-ion battery refer to cells employing Co, Mn and Ni based cathodes.[35] 12

2.8 Cost analysis of LIBs and SIBs using different cathode materials, such as layered oxides, phosphates and PW. Reprinted from ref.[52] 14

2.9 Common side reaction in SMBs. 15

2.10 Schematic presentation of SIPEs. The anionic center (blue) is tethered to the polymer backbone (black) via a spacer arm (green), while the cation (red) is mobile. 21

2.11 Chemical structure and dissociation energies of lithium salt monomers with different ionic centers (blue). Reprinted from ref.[95] 22

2.12 Chemical structure of common spacer arms. 23

2.13 Cross-linked structure of the LiSFSI-PETMP/4A-SIPE. Reprinted with permission from ref.[82] 24

4.1 Synthesis procedure of the synthesized NaSTFSI. 30
4.2 ^{1}H, ^{13}C and ^{19}F-NMR of the NaSTFSI monomer. 31
4.3 Synthesis procedure of NaSDCM. 32
4.4 ^{1}H and ^{13}C of the synthesized NaSDCM monomer. 33
4.5 Synthesis procedure of NaFTFSI. 34
4.6 ^{19}F-NMR of the synthesized NaFTFSI monomer. 34
4.7 Synthesis procedure of NaMDCM. 35
4.8 ^{1}H and ^{13}C of the synthesized NaMDCM monomer. 36
4.9 Direction depending separation of the magnetic moment μ into two different energy levels. 42
4.10 Example NMR graph of 1,3-dichloropropane. Reprinted from ref.[115] 43
4.11 a) Sketch of an interferometer used for FT-IR spectroscopy. b) Example spectrum of a lipopeptide with marked absorbant' bands.[119] 44
4.12 A schematic TGA curve. No mass loss is detected in the stable region, while decomposition is visible as a mass loss with increasing temperature. 45
4.13 A typical DSC curve. Reprinted from ref.[122] 46
4.14 Schematic illustration of a) the applied current and b) the resulting potential response upon cycling. 47
4.15 Schematic illustration of an anodic and cathodic LSV scan to determine the ESW. 48
4.16 a) Schematic voltage profile and b) cycling performance. 49
4.17 Schematic stress-strain curve via uniaxial tensile test. Reprinted from ref.[128] . . 50
4.18 Nyquist plot of a typical EIS scan. Reprinted from ref.[129] 51
4.19 Sample XPS spectrum of surface species with binding energy peaks corresponding to specific elemental composition and chemical state. 52
4.20 a) Schematic diagram of a SWAXS setup. b) Small- and c) wide-angle X-ray scattering of the diene-SIPE. 53

5.1 a) Cross-linked structure (NaSTFSI in green, PETMP in blue, and PET4A in red) and b) image of the self-standing NaSTFSI-SIPE. 61
5.2 a) FT-IR spectra of NaSTFSI, PET4A, PETMP, and NaSTFSI-SIPE. ^{1}H$\rightarrow$^{13}C CPMAS NMR spectrum of b) NaSTFSI and NaSTFSI-SIPE, recorded at 10 kHz. Note: Signals marked with asterisks (*) are spinning side-bands. 62
5.3 a) TGA/MS and b) DSC of the NaSTFSI-SIPE. 63

5.4 Electrochemical characterization of the NaSTFSI-SIPE: a) ionic conductivity in the temperature range of 10-90 °C, b) anodic and cathodic scan in Na||Al cells, c) Na stripping/plating test over 2000 h at different current densities in Na||Na symmetric cells, and d) the corresponding Nyquist plot after cycling for 10 cycles at each current density. Additionally, the EIS was measured after 100 cycles at 50 µA/cm^2 (red line). All tests were performed at 40 °C. 65

5.5 Ex-situ C 1s, S 2p, and F 1s XPS spectra of the surface of the NaSTFSI-SIPE (dried), incorporating EC:DMC:FEC molecular transporters (soaked) and after cycling for 5 cycles in a Na||Na symmetric cell under 10 µA cm^{-2} (cycled). 67

5.6 Ex-situ XPS spectra of O 1s and Na 1s of NaSTFSI-SIPE surface after cycling for 5 cycles in a Na||Na symmetric cell under 10 µA cm^{-2}. 68

5.7 ToF-SIMS combined mappings of S- (red) and F- (green) ionic fragments on the surface of the NaSTFSI-SIPE (dried), incorporating EC:DMC:FEC molecular transporters (soaked) and two zones after cycling for 5 cycles in a Na||Na symmetric cell under 10 µA cm^{-2} (cycled). 69

5.8 a) Voltage profile and b) cycling performance of hydrated (green) and dehydrated (black) PW cathode using NaSTFSI-SIPE at 40 °C. 70

5.9 Voltage profile and cycling performance of PW cathode using a,b) 1M NaPF$_6$ in EC:DEC (3:7 vol%) liquid electrolyte and c,d) NaSTFSI-SIPE at 40 °C. 71

5.10 Photographs of NaSTFSI-SIPE membranes synthesized for the optimization of the PVDF-HFP content. The molar ratio of PET4A, PETMP, and NaSTFSI (2:10:7) was kept constant. Table 5.2 shows the chemical molar ratio of NaSTFSI-SIPE membranes. 76

5.11 a) TGA (heating rate of 5 K min^{-1}, inert He atmosphere), and b) DSC (two cooling and heating cycles between -20 and 200 °C with a 5 K min^{-1} rate) of the dried NaSTFSI-SIPEs with different PVDF-HFP ratios from 2:10:7:0 (0% PVDF-HFP) to 2:10:7:11 (36 mol% PVDF-HFP). 77

5.12 DSC of pure PVDF-HFP with a cooling and heating cycle between -20 and 200 °C at a rate of 5 K min^{-1}. 78

5.13 a) Molecular transporter (EC: DMC: FEC in 49: 49: 2 vol. ratio) uptake in wt.% and b) temperature-dependent ionic conductivity at 20, 40 and 60 °C of swelled NaSTFSI-SIPEs with different PVDF-HFP ratios from 0% PVDF-HFP to 36 mol% PVDF-HFP. 79

5.14 a) TGA (heating rate of 5 K min^{-1}, inert He atmosphere), and b) DSC (two cooling and heating cycles between -20 and 200 °C with a 5 K min^{-1} rate) of the dry NaSTFSI-SIPE with various SSM concentrations. 81

5.15 a) Temperature-dependent ionic conductivity, and b) activation energy of the NaSTFSI-SIPEs with different NaSTFSI contents (from 1:10:7:4.4 to 4:10:7:4.4) and EC:DMC:FEC molecular transporter incorporation. 82

5.16 a) Na plating/stripping tests of Na||M2||Na and Na||M4||Na cells at different current densities at 40 °C. Nyquist plots after the initial and last cycles at different current densities in b) the Na||M2||Na and c) the Na||M4||Na cell. Voltage profiles of Na||NaSTFSI-SIPE||PW cells composed d) 2:10:7:4.4 (9 mol% NaSTFSI – light green) and e) 4:10:7:4.4 (17 mol% NaSTFSI – dark green), and f) the corresponding specific capacity and Coulombic efficiency upon cycling. EC:DMC:FEC (49:49:2 vol.%) molecular transporter is incorporated into all SIPEs. The galvanostatic cycling test with a current density of C/50 the 1st cycle, followed by 5 cycles at C/20 and ongoing ones at C/10 between 3.8 V and 1.3 V. All measurements were performed at 40 °C. 84

5.17 Chemical structure of the three investigated SSMs: NaSTFSI (green), NaSDCM (orange), and NaVBS (blue). 88

5.18 a) TGA (heating rate of 5 K min^{-1}, inert He atmosphere), and b) DSC (cooling and heating cycles between -20 and 200 °C with a 5 K min^{-1} rate) of the dried NaSTFSI-, NaSDCM-and NaVBS-SIPEs with the 4:10:7:4.4 molar composition. 88

5.19 a) Temperature-dependent ionic conductivity and b) anodic and cathodic stability LSV curves (Na||SIPE||Al, scan rate of 30 µV s^{-1}, temperature 40 °C) of the NaSTFSI-, NaSDCM-, or NaVBs-SIPE with 50 wt.% of carbonate-based molecular transporters. 90

5.20 Stripping and plating tests of a) NaSTFSI-, b) NaSDCM- and c) NaVBS-SIPE at different current density at 40 °C. 91

5.21 XPS analysis of NaSDCM-SIPE SEI. High-resolution a) C 1s, b) F 1s, and c) S 2p photoelectron regions. 92

5.22 Voltage profiles of Na||SIPE||PW cells composed of a) NaSTFSI- and b) NaSDCM-SSMs and c) the corresponding specific capacity and Coulombic efficiency upon cycling. EC:DMC:FEC (49:49:2 vol.%) molecular transporter is incorporated into all SIPEs. The galvanostatic cycling test with a current density of C/50 the 1st cycle, followed by 5 cycles at C/20 and ongoing ones at C/10 between 3.8 V and 1.3 V. All measurements were performed at 40 °C. 93

5.23 Chemical structure of the NaSTFSI, NaMTFSI and NaFTFSI SSMs. 96

5.24 a) TGA and b) DSC (heating rate of 5 K min^{-1}, inert N_2 atmosphere for both experiments) of NaSTFSI- (black), NaMTFSI- (purple) and NaFTFSI (green)-dry SIPEs. 97

5.25 a) Temperature-dependent ionic conductivity and b) electrochemical stability window (Na||SIPE||Al, scan rate of 30 µV s^{-1} at 40 °C) of NaSTFSI-, NaMTFSI- and NaFTFSI-based SIPEs containing the EC:DMC:FEC molecular transporter. 98

5.26 Na stripping/plating tests at different current densities at 40 °C using a) NaSTFSI-, c) NaMTFSI-, and e) NaFTFSI-SIPEs together with the corresponding Nyquist plot of b) NaSTFSI-, d) NaMTFSI- and f) NaFTFSI-SIPE after the 1st and 5th cycle at each current density: 10 µA cm^2 – black, 20 µA cm^2 – red, 30 µA cm^2 – blue, 40 µA cm^2 – green and 50 µA cm^2 – purple, as well as after 1st and 5th in the long-term cycling at 50 µA cm^2 – yellow. Additionally, 50 wt.% of EC:DMC:FEC (49:49:2 vol.%) molecular transporter were incorporated into all SIPEs. 100

5.27 Voltage profile of Na||PW cells using a) NaSTFSI-, b) NaFTFSI- or c) NaMTFSI-SIPEs, and the corresponding d) specific capacity and Coulombic efficiency. In all SIPEs EC:DMC:FEC (49:49:2 vol.%) molecular transporter is incorporated. The galvanostatic cycling tests are carried out at a current density of C/50 the 1st cycle, followed by 5 cycles at C/20 and ongoing ones at C/10 between 3.8 V and 1.3 V. All measurements are performed at 40 °C. 102

5.28 Structure of the monomers that were used to synthesize the diene-, trione-, PET4A- and PET6A-based SIPEs that build up the polymer backbone together with PETMP (in blue). 105

5.29 a) The measured stress-strain curve and b) the maximum strain before breaking of the diene-, trione-, PET4A- and PET6A-SIPEs. The tests were performed on neat SIPEs, i.e., without PVDF-HFP and molecular transporter, at RT. 106

5.30 a) TGA and b) DSC of dry diene-, trione-, PET4A- and PET6A-based SIPEs (heating rate of 5 K min^{-1}, inert N_2 atmosphere, the DSC was performed by two cooling and heating cycles between -20 and 200 °C). 107

5.31 a) WAXS and b) SAXS pattern of commercial PVDF powder, PVDF-HFP powder and a pure PVDF-HFP membrane. 108

5.32 a) WAXS and b) SAXS patterns of the diene-, trione-, PET4A- and PET6A-based SIPEs without PVDF-HFP and with PVDF-HFP (c) and d), respectively). . . . 109

5.33 a) Density and b) calculated pore size of the diene-, trione-, PET4A- and PET6A-based SIPEs blended with PVDF-HFP. The dry membranes' patterns were collected at RT. 110

5.34 a) Temperature-dependent ionic conductivity, and b) electrochemical stability window (Al||SIPE||Na, scan rate of 30 µV s^{-1}, temperature 40 °C) of the diene-, trione-, PET4A- and PET6A-based SIPEs containing 50 wt.% of molecular transporter (EC:DMC:FEC). 111

5.35 Voltage profile of the Na||SIPE||PW cells, containing a) diene-, b) trione-, c) PET4A- and d) PET6A-SIPE. The galvanostatic cycling tests are performed at C/50 (1st cycle), followed by at C/20 (5 cycles) and C/10 until failure between 3.8 V and 1.3 V. All measurements were performed at 40 °C. The SIPE contains 50 wt.% of EC:DMC:FEC. 113

5.36 Cycling performance (capacity vs. cycle number and the corresponding Coulombic efficiency) of Na||PW cells using the diene-, trione-, PET4A- and PET6A-SIPEs (included 50 wt.% of molecular transporter). The galvanostatic cycling tests were carried out at 40 °C, applying C/50 in the first cycle, C/20 in the following 5 cycles and C/10 until achieving 200 cycles, between 3.8 V and 1.3 V. 114

5.37 Temperature-depending ionic conductivity of the NaSTFSI-, optimized NaSTFSI-, NaSDCM-, NaMTFSI-, diene- and NaMDCM-SIPE between 10 and 90 °C. . . . 116

5.38 a) TGA and b) DSC of NaMDCM-SIPE (heating rate of 5 K min^{-1}, inert N_2 atmosphere). The DSC was performed by two cooling and heating cycles between -20 °C and 200 °C. 117

5.39 a) The electrochemical potential window of the NaMDCM-SIPE. b) The stripping and plating behavior of the of the NaMDCM-SIPE in Na||Na cells at 40 °C with an increasing current density between 10 and 50 µA cm^{-2} and c) the impedance plot after the 1st and 5th cycle of each current density and after long-term cycling at 50 µA cm^{-2}. 117

5.40 a) Voltage profile of the NaMDCM-SIPE and b) cycling performance up to 200 cycles and c) up to 100 cycles at 40 °C. The cell was run at 1 C after an initial formation cycle at C/50 and 5 cycles at 0.1 C. 118

8.1 The logarithmic plot of the conductivity vs. 1000/T. The obtained slope of -1.49 T was multiplied with -8.6·10^{-5} eV T^{-1} to determine the activation energy of 0.13 eV. 134

8.2 Photographs of NaSTFSI-SIPE membranes synthesized for the optimization of the PET4A/PETMP molar ratio. The PET4A/PETMP molar ratio has been varied in 15% steps, while the molar ratio of NaSTFSI and PVDF-HFP vs PETMP was kept constant at 20% and 44%, respectively. Table 5.1 shows the chemical molar ratio of NaSTFSI-SIPE membranes. 134

8.3 Photographs of NaSTFSI-SIPE membranes synthesized for the optimization of the NaSTFSI SSM content. Table 3 shows the chemical molar ratio of NaSTFSI-SIPE membranes. 135

8.4 Arrhenius plot ln $(\sigma) vs 1000/T) of NaSTFSI-, NaMTFSI - and NaFTFSI - based SIPEs containing 50 wt.\% of EC : DMC : FEC$. 135

8.5 The isotherm of the BET measurements of the dry diene-, trione-, PET4A- and PET6A-based SIPEs with PVDF-HFP. 135

List of Tables

2.1 Table of Na-based SIPEs in the literature 25

4.1 Membrane list of chapter 5.1 and 5.2 39
4.2 Membrane list of chapter 5.3 and 5.4 40
4.3 Membrane list of chapter 5.5 and 5.6 40

5.1 Composition of the dry NaSTFSI-SIPE membranes used for the evaluation of the influence of the PET4A content on the SIPE membranes. 75
5.2 Molar ratios of dry NaSTFSI-SIPE membranes used for the assessment of the influence of PVDF-HFP on the SIPE. 76
5.3 Investigated SSM ratios in the dry NaSTFSI-SIPE membranes. 80

Acknowledgements

Family

First of all, I have to thank my beautiful, charming, and lovely wife Lisa for her unending love and support not only during my PhD time but in every second of my life. I especially want to thank you for all the support you gave me during all the challenging times and for the effort, time, and motivation you put into raising Raphael with me. I love you so much and look forward to the wonderful future that we will have together. Next, I want to thank my family, namely my mother and my little brother Vincent, for supporting my career from the very beginning and for giving me an awesome childhood to look back on. Your unwavering support has been a cornerstone of my success, and I'm truly grateful for everything you've done for me.

Supervision

I want to thank Prof. Dr. Stefano Passerini for accepting me as his PhD Student and for his supervision and corrections. The SIMBA project was a perfect fit for my interests, combining my interests in organic and physical chemistry. I want to thank you for this opportunity that allowed me to spend so much time with functional polymers that can potentially be utilized for the next generation of save batteries.

Next, I want to express my highest gratitude to Dr. Maider Zarrabeitia for her support and supervision as well as for her open ear for all my problems and concerns over the last years. I know that the organic synthesis and the characterization of completely new SIPE were a challenging topic but I want to thank you for giving me the freedom to research in the direction I thought of as most promising without any restrictions. This thesis would not have been possible without you, I am thankful for having you as my supervisor as I always felt well supported throughout my studies in every regard. Your insights and guidance not only strengthened this work but also significantly shaped the way I will approach scientific challenges in the future.

Funding

I want to thank the HORIZON 2020 program (Project "SIMBA" 963542) as well as the Helmholtz Association for the financial support that made this project possible and I am truly grateful for this opportunity.

Best Friends

I have to thank my best friends Jameela and Leon, who are always there for me and also helped me a lot during my PhD time in so many ways, including discussing science, checking my work, taking care of Raphy, keeping me engaged in the topic etc.. Thank you for everything. Leon, I want to thank you for traveling with me to Sweden so I could meet Lisa there and now have the live I always wanted. Jameela I want to thank you for the consistent support with Raphael. You were the family in Ulm that we could rely on so often. I want to thank you both as I know that I can always count on.

Close Friends

I want to thank many people that I met during my PhD time but I can not name all of them, thus I will only shortly mention the ones that helped me the most during my journey and kept me motivated and inspirited throughout the years. Namely I want to thank Leo (Organic lab buddy for daily discussions), Anja, Julio, Timo (Norway), Ivan, Priya, Mariana, Laura, Elias, Kike, Dominik K1, Medina, Gregoire, Guillaume all the people of the organic sub group and all the people of EChem1.

Workspace

I want to thank all the people at HIU for the team events, the group meetings, the BBQs, the shared ice cream events etc. for creating such a nice working environment as well as the admin and safety team that keep everything running smoothly at HIU. Already mentioned as close friends, I want to thank Medina again for keeping the organic lab in order and organizing the organic sub group meeting previously mentioned.

External Contributions

I want to thank the Co-Authors of my published/submitted papers for the additional measurements they performed and/or analyzed. Additionally, I want to thank the von Delius group at Ulm University for the solution NMR measurements and Altris AB for providing the Prussian White cathode material.

Academic Contributions

Chapter 10.1
Scientific Meetings and Conferences

7th ICNaB, 2022

C. Wunder, M. Zarabaitia, S. Passerini. New single-ion solid-state sodium polymer electrolyte [Poster presentation]. International Conference on Sodium Batteries, Ulm, Germany (2022, December 6-8). https://chemistry-europe.onlinelibrary.wiley.com/doi/toc/10.1002/(ISSN)1864-564X.sodium-ion-batteries

13th ISP, 2023

C. Wunder, M. Zarabaitia, S. Passerini. 3D networking single-ion polymer electrolytes for sodium-based batteries [Oral presentation]. International Conference on Polyelectrolytes, Prague, Czechia (2023, August 28 - September 1). https://isp2023.com/

4th SBS, 2023

C. Wunder, M. Zarabaitia, S. Passerini. Single ion NaSTFSI-based solid polymer electrolyte for next generation solid state sodium batteries [Oral presentation]. International Sodium Battery Symposium, Dresden, Germany (2023, September 4-5). https://www.batterien.fraunhofer.de/de/Messen_Ve
sodium-battery-symposium-sbs4.html

18th ISPE, 2024

C. Wunder, M. Zarabaitia, S. Passerini. Sodium Salt Monomer Side Chain Influence on Single-Ion Polymer Electrolytes for Sodium-based batteries [Poster presentation]. International Symposium on Polymer Electrolytes, Langkawi, Malaysia (2024, June 23-28). https://www.ispe18.com/

Chapter 10.2
Publications

Clemens Wunder et al. *Sodium 4-styrenesulfonyl (trifluoromethanesulfonyl) imide-based Single-ion Conducting Polymer Electrolyte incorporating Molecular Transporters for Quasi-Solid-State Sodium Batteries.* Journal of Materials Chemistry A, 12 (32) , 2024, p. 20935-20946, DOI: 10.1039/D4TA02329C.[153]

Clemens Wunder et al. *Understanding the Component-Driven Influence on the Electrochemical Properties in Single-Ion Polymer Electrolytes for Sodium-Based Batteries* ACS Applied Polymer Materials, 7 (8) , 2025, p. 4895–4907, DOI: 10.1021/acsapm.4c04234.[175]

Clemens Wunder et al. *Influence of the backbone chemistry and side-chain spacer flexibility in sodium single-ion conducting polymer electrolyte for sodium-batteries* EES Batteries, 2025, DOI: 10.1039/D5EB00145E.[164]